

# Measurement of the Proton Form Factor Ratio at Low Momentum Transfer

Thesis for the degree of  
“Doctor of Philosophy”

By  
Moshe Friedman

Submitted to the Senate of the Hebrew University of Jerusalem  
August 2016

This work was carried out under the supervision of:

Prof. Guy Ron

# Abstract

Experiment E08-007-II measured the proton elastic form factor ratio  $\mu G_E/G_M$  in the momentum transfer range of  $Q^2 \approx 0.02 - 0.08 \text{ GeV}^2$ , the lowest ever measured by polarization transfer techniques. The experiment was performed at the Thomas Jefferson National Accelerator Facility in Newport News, Virginia, USA during 2012. A polarized electron beam with energies of 1.1, 1.7, and 2.2 GeV was elastically scattered off a polarized solid  $\text{NH}_3$  target. The asymmetries between the cross section of positive and negative helicity states of the beam were determined. These asymmetries can be used to determine the form factor ratio.

In this thesis, we present the asymmetry analysis of the experiment, discuss the main challenges and show preliminary results for part of the data. Preliminary asymmetries indicate an increase in the form factor ratio above unity. However, a complete analysis is required before any conclusion can be made. Further analysis is ongoing, and final asymmetry results and form factor extraction is expected during 2017.

We also present first results for  $^{14}\text{N}$  asymmetries for elastic and quasi-elastic scattering. The measured asymmetries are in agreement with the shell model approximation, within the low accuracy of the measurement. A change in the asymmetry sign between the elastic and the quasi-elastic processes is seen, and should motivate further theoretical studies. These experimental asymmetries will also be useful for systematic studies of other experiments using polarized  $\text{NH}_3$  targets.

# Acknowledgments

This work could not have been completed without the guidance, advice, and encouragement given by many whom I would like to personally thank for their contributions and ongoing support.

First, I would like to thank my advisor, Prof. Guy Ron, who supported my goals from beginning and gave me the opportunity to work with world class scientists from the Jefferson Lab. I would also want to thank Dr. Douglas Higinbotham for his guidance and support, and in particular, for being a role model in the field of experimental physics.

During this endeavour, I collaborated with many graduate students and postdocs. Their cooperation, patients, and help was much appreciated. Among them, I would like to specifically thank Jixie Zhang, Dustin Keller, Chao Gu, Min Huang, Jie liu, Toby Badman, Ryan Zielinski, Melissa Cummings, and Pengjia Zhu.

I would also like to extend my appreciation to my colleagues and peers in Israel who provided me with support and advice when needed. In particular, I would like to thank Moshe Tessler, Dan Cohen, Ben Ohayon, David Izraeli, Yonatan Mishnaiot, Gitai Feinberg and many others who assisted me in my efforts to complete this work.

Special appreciation is extended to my former advisor, Prof. Michael Paul, who supported my work and efforts for many years.

But most of all, I want to thank my wife for her patience, support, and her ongoing encouragements that saw us and our family through the hardships associated with these kinds of personal undertakings.

# A Letter of Contribution

The experiment described in this thesis, the preparations, and the analysis, were performed in a common effort of the E08-007 and E08-027 collaborations. This report is focused on my personal contribution to the experimental and analysis parts of the research. Nevertheless, the report also describes others contributions, as will follow. Since there are many people involved in various aspects of the research, they will not be referred by their names.

The preparations for the experiment were mainly done long before I joined the group. During the last stages of the preparations, as soon as I joined the group, I took the lead on the E08-007 experiment. During E08-007 data production, I was responsible for on-line and off-line data analysis and decisions that had to be taken accordingly.

After the experiment, I performed the physics data analysis for experiment E08-007. This does not include the optics analysis, except for the elastic peak angular correction described in Sec. 3.2.4 which I performed. The target analysis was also performed mainly by the target group.

The basic g2psim simulation package was written in common efforts, while I contributed the elastic cross section models. I developed and implemented the adaptation of g2psim to the data, the partial contributions determination procedure, and the asymmetry extraction for both  $^1\text{H}$  and  $^{14}\text{N}$ . I also performed the uncertainty analysis for the above.

# Contents

<b>1</b>	<b>Introduction</b>	<b>15</b>
1.1	Definitions and Formalism	16
1.1.1	Electron Scattering	16
1.1.2	Formalism	17
1.1.3	Elastic Form Factors	18
1.1.4	Hadronic Currents	19
1.2	Measurement Techniques	20
1.2.1	Rosenbluth Separation	20
1.2.2	Polarization transfer measurements	22
1.2.3	Double Spin Asymmetry	23
1.3	World Data	26
1.3.1	World Data	26
1.3.2	Models and Fits	30
1.3.3	Constituent Quarks Models (CQMs)	31
1.3.4	Lattice QCD	33
1.3.5	Fits	33
<b>2</b>	<b>Experimental Setup</b>	<b>36</b>
2.1	Setup	36
2.2	Kinematics	38
2.3	CEBAF	38
2.4	Experimental Hall A	40
2.4.1	General	40
2.4.2	Rasters	40
2.4.3	Møller Polarimeter	41
2.4.4	Chicane Magnets	42
2.4.5	High Resolution Spectrometers	44

2.5	Polarized Target . . . . .	48
2.5.1	Dynamic Nuclear Polarization . . . . .	49
2.5.2	Target Material . . . . .	51
2.5.3	Target Assembly . . . . .	51
2.6	Septum Magnets . . . . .	54
2.7	Data Acquisition . . . . .	55
<b>3</b>	<b>Data Analysis</b>	<b>58</b>
3.1	Target Polarization . . . . .	58
3.1.1	NMR Signal Fitting and Integration . . . . .	59
3.1.2	Thermal Equilibrium Polarization . . . . .	60
3.1.3	Polarization Data . . . . .	61
3.1.4	Uncertainties . . . . .	62
3.2	Optics . . . . .	64
3.2.1	Definition of Coordinate Systems . . . . .	64
3.2.2	Reaction Variables Reconstruction . . . . .	69
3.2.3	Tilt Angle . . . . .	70
3.2.4	Elastic peak correction . . . . .	70
3.2.5	The g2p Helicity Decoder . . . . .	72
3.3	Asymmetries . . . . .	75
3.3.1	Cuts . . . . .	75
3.3.2	Raw Asymmetries . . . . .	76
3.4	Dilution analysis . . . . .	81
3.4.1	General . . . . .	81
3.4.2	g2psim . . . . .	83
3.4.3	Physical Asymmetries Extraction . . . . .	85
3.4.4	Uncertainties . . . . .	89
<b>4</b>	<b>Results and Discussion</b>	<b>96</b>
4.1	Proton Asymmetries . . . . .	96
4.2	Nitrogen Asymmetries . . . . .	98
4.3	Summary of Uncertainties . . . . .	100
4.4	Discussion . . . . .	101
4.4.1	Proton Asymmetries . . . . .	101
4.4.2	Nitrogen Asymmetries . . . . .	102
4.5	Future Outlook . . . . .	102

A Elastic Scattering Kinematics	114
B The Breit Frame	116

# List of Figures

1.1	Leading order Feynman diagram for $ep$ elastic scattering. . . . .	16
1.2	Illustration of the Rosenbluth separation method. . . . .	21
1.3	Coordinate system for the recoil polarization measurement. . . . .	23
1.4	World data for proton $G_E$ from unpolarized measurements [17–29], using the Rosenbluth method, normalized to the dipole parameterization. Figure from [30]. . . . .	25
1.5	World data for proton $G_M$ from unpolarized measurements [17, 19, 21, 23, 25–29, 31, 32], using the Rosenbluth method, normalized to the dipole parameterization. Figure from [30]. . . . .	25
1.6	Ratio $\mu G_E/G_M$ extracted from polarization transfer (filled blue diamonds) and Rosenbluth method (open red circles). The top (bottom) figures show Rosenbluth method data without (with) TPE corrections applied to the cross sections. Figures from [33]. . . . .	27
1.7	Low $Q^2$ polarization measurements of $\mu G_E/G_M$ , models and fits [34, 35, 37–39, 42, 45–52]. Figure from [45] . . . . .	28
1.8	A summary of some recent proton charge radius determinations: Sick [53], CODATA 2006 [54], Pohl et al. [8], Bernauer et al. [55], CODATA 2010 [56], Zhan et al. [45], and Antognini et al. [9]. Figure from [57]. . . . .	28
1.9	The form factors $G_E$ and $G_M$ , normalized to the standard dipole, and $G_E/G_M$ as a function of $Q^2$ , as measured at MAMI . . . . .	29
1.10	Vector meson dominance picture for the coupling of the photon to a nucleon. . . . .	30
1.11	Several VMD fits compared to the JLab $\mu G_E/G_M$ data. . . . .	31
1.12	The JLab $\mu G_E/G_M$ data compared to the results of some constituent quark models. . . . .	32
1.13	Connected and disconnected lattice diagrams. . . . .	33

1.14	Fits to nucleon electromagnetic form factors. For $G_{E_n}$ , data using recoil or target polarization [72–78] are shown as filled circles while data obtained from the deuteron quadrupole form factor [79] are shown as open circles. Figure from [71]. . . . .	34
2.1	Schematic diagram of the GEp experimental setup. See text for description.	37
2.2	Schematic diagram of the Continuous Beam Accelerator Facility (CEBAF) at Jefferson Lab. The electron beam is produced by a Ti:Sap laser at the injector and further accelerated in each of two superconducting linacs. The beam can be extracted simultaneously to each of the three (today four) experimental halls. . . . .	39
2.3	Schematic cross section of Hall A with one of the HRS spectrometers in the (fictitious) $0^\circ$ position. Figure is taken from [84]. . . . .	40
2.4	Fast and slow raster patterns. . . . .	41
2.5	Layout of the Møller polarimeter, (a) presents a side view, while (b) presents a top view. The trajectories displayed belong to a simulated event of Møller scattering at $\theta_{CM} = 80^\circ$ and $\phi_{CM} = 0^\circ$ , at a beam energy of 4 GeV. Figure taken from [84]. . . . .	42
2.6	The two chicane magnets. Scattering chamber (“target”) is seen at the left of the image. . . . .	43
2.7	Layout of HRS magnets and detector package. . . . .	44
2.8	Layout of the detector package. The arrow illustrates particle trajectory. . .	46
2.9	Layout of a VDC pair for one HRS (not to scale). The active area of each wire plane is rectangular and has a size of 2118 mm $\times$ 288 mm. Each VDC consists of one U and one V wire plane. The sense wires in each of them are orthogonal to each other and lie in the laboratory horizontal plane. They are inclined at an angle of $45^\circ$ with respect to both the dispersive and the non-dispersive directions. The vertical distance between like wire planes is 335 mm. Figure from [84]. . . . .	47
2.10	Particle detection in VDC. The charged particle ionizes the gas within the drift chamber, and the drift electrons are detected by the wires. Drift time information is used to reconstruct the trajectory within the VDC. . . . .	48
2.11	Layout of scintillators plane. . . . .	49

2.12	Population densities of the electron levels $N_e$ at different temperatures of the spin-spin interaction reservoir $T_{SS}$ and electron Zeeman reservoir $T_{Ze}$ . (a) Spin-spin interaction reservoir and Zeeman reservoir in thermal equilibrium with the lattice: $T_{SS} = T_{Ze} = T_L$ , (b) $0 < T_{SS} < T_{Ze}$ . Figure from [95]	50
2.13	Target assembly.	52
2.14	The evaporation refrigerator.	53
2.15	The target cells. On the left the cells are shown empty in air. On the right, the cells are full and submerged in liquid nitrogen. The top two cells seen contained the $\text{NH}_3$ target material. The microwave horn can be seen at the top of the image. Figure from [97].	54
2.16	A schematic drawing of the septum magnet.	55
2.17	Hall A standard DAQ system.	56
2.18	Helicity signals.	56
2.19	Schematic diagram depicting the RF generator, the Q-meter, and the target cavity. Figure from [96].	57
3.1	An example of raw NMR signal for one of the TE measurements. The black curve is the polynomial fit for the baseline.	59
3.2	The TE (left) and the enhanced signal (right) after baseline and background subtraction.	60
3.3	Example of fits in area and pressure analysis for TE. The top left (right) shows the two parameter check on the slope of the line for area (pressure). The bottom left (right) shows the final one parameter fit to a one parameter line for area (pressure). The error bars represents the total uncertainties, which are dominated by systematics. Figure from [96].	61
3.4	The final charge-averaged polarization and uncertainty per run. As discussed in the text and summarized in Tab. 3.2, the uncertainties are mainly calibration uncertainties, and corresponds to a global scaling uncertainty for each data set.	63
3.5	Geometric configuration of the sieve slit. Dimensions are in mm. The two large holes are used to determine the orientation of the sieve slit. The diameter is 1.4 mm and 2.7 mm for the normal holes and the large holes respectively. Figure from [101].	65

3.6	Coordinate systems for the scattering of polarized electrons from polarized target. In this figure, the unit vectors $\vec{u}_S, \vec{u}_N, \vec{u}_L$ define the scattering coordinate system, while $\vec{u}_x, \vec{u}_y, \vec{u}_z$ define the starred coordinate system. Figure from [16]. . . . .	66
3.7	Target coordinate system (top and side views). $\theta_0$ is the spectrometer central angle in HCS, $L$ is the distance from the sieve slit to the TCS origin, $D_x$ and $D_y$ are the vertical and horizontal deviations of the spectrometer central ray to the HCS origin. Figure from [101]. . . . .	67
3.8	Focal plane coordinate system. The red trajectories represents trajectories with $\theta_{tg} = \phi_{tg} = 0$ . Figure from [101]. . . . .	67
3.9	Typical focal plane plot in TRCS (a), compared to the reconstructed variables of momentum and scattering angle (b). The separation between elastic scattering on hydrogen and the heavier elements $^{14}\text{N}$ and $^4\text{He}$ is evident already on the focal plane, and the red curves compare the reconstructed variables to the elastic stripe formula (Eq. 3.18). . . . .	73
3.10	Angular distribution of the angles calculated by Eq. 3.19, using the cut $ \theta - 0.1  < 5 \times 10^{-4}$ , and cutting on hydrogen elastic events. A deviation of the mean from 0.1 indicates an inaccuracy in the reconstruction of the scattering variables. . . . .	74
3.11	Scattering angle correction function for the left arm 2.2 GeV configuration. This function is calculated based on the mean detected momenta and the elastic scattering relation (Eq. 3.19). The function is used as a correction of the scattering angle on an event-by-event basis. . . . .	74
3.12	Invariant mass distributions for the left HRS at all experimental configurations. Except for the lowest $Q^2$ setting, the hydrogen elastic events can be identified as the peak at $\sim 938$ MeV. . . . .	77
3.13	$\phi_{HCS}$ distributions for the left HRS at all experimental configurations (blue), compared to g2psim (black, see Sec. 3.4.2). In red are the cuts that were used for the analysis. . . . .	78
3.14	Blue: raw asymmetries for all left HRS runs. Red: raw asymmetries corrected for half-wave plate, beam and target polarizations. The fits for a constant value are done for the corrected asymmetries, and the $\chi^2/\text{NDF}$ values show consistent statistical behavior after these corrections. The gap in the 2.2 GeV runs (a+b) is due to the change in the target material (see text). . . . .	79
3.15	Raw asymmetries for all right HRS runs. . . . .	80

3.16	$^{14}\text{N}$ polarization as function of proton polarization. The squares and the stars represents two methods of measurements, while the solid curve represents an EST-based calculation. Further details of the measurements and calculation can be found in [106]. . . . .	81
3.17	Comparison between experimental data at 2.2 GeV and g2psim output. For the heavy elements, elastic interactions (low W peaks) and quasi-elastic interactions (high W peaks) are calculated separately. The absolute yields are arbitrary for all interactions. . . . .	84
3.18	Simulation results for all experimental configurations. The black curves are the experimental data, the red curves are the total simulated yields, the blue, green and purple curves are the proton, helium and nitrogen partial contributions, respectively. . . . .	87
3.19	An example of invariant mass histogram divided into three regions, each dominated by different reaction: proton elastics (1), heavy-elements elastics (2) and quasi-elastics (3). The partial contribution of each reaction is determined based on simulation. . . . .	88
3.20	An example of simulated background (red) relative to the simulated proton elastic peak (blue). Invariant mass cuts of $\pm 1$ MeV (black) and $\pm 4$ MeV (purple) are drawn in dashed lines. The proton-to-background ratio changes significantly with cut width. . . . .	90
3.21	Polarization-corrected raw asymmetries, $A_{raw}/P_B P_T$ as function of invariant mass cut width. A decrease in raw asymmetry is evident as cut width increases due to the lower proton-to-background ratio. Error bars represents statistical uncertainties, which are highly correlated between different cuts. . . . .	93
3.22	Physical asymmetries as a function of invariant mass cut width. Physical asymmetries extracted according to the procedure described in the text. Except for the tightest cuts, consistent values obtained for the different cut widths. Error bars represents statistical uncertainties, which are highly correlated between different cuts. . . . .	94

3.23	Systematic study of simulation-related uncertainty. The uncertainty is estimated by changing the parameters of the smearing Gaussian, which represents energy calibration ( $\mu$ ) and resolution adjustment ( $\sigma$ ). The plots show two extreme parameterizations that still produce reasonable fits (top), and the parameterization that is used for the asymmetry extraction(bottom). The extracted asymmetries in this case varies between 2.72%-2.77% for protons, 0.078%-0.081% for the heavy-elastic peak, and 0.186%-0.233% for the quasi-elastic peak. Based on the entire data set, conservative systematic uncertainties of 2%, 10% and 25%, respectively, were estimated. . . . .	95
4.1	Physical asymmetries for electron-proton elastic scattering. The solid line is the calculated asymmetry using the dipole parametrization (Eq.1.53). See text for the meaning of the the horizontal error bars. . . . .	97
4.2	Physical asymmetries for electron- <sup>14</sup> N elastic (blue circles) and quasi-elastic (red squares) scattering. See text for the meaning of the the horizontal error bars. . . . .	99
A.1	Notations for elastics scattering. . . . .	114

# List of Tables

2.1	Central kinematics for the left arm. $\theta$ is the scattering angle, while starred angles are the angles of the proton polarization axis relative to the recoil direction (see Sec. 1.1.2). Note that average values are different due to cross section weighting. . . . .	38
2.2	Beam polarization as measured by Møller polarimetry. Quoted uncertainties are statistical. Systematic uncertainties are estimated to be 1.7% for all measurements. For details see [91]. . . . .	43
2.3	Main design characteristics of the Hall A high resolution spectrometers; the resolution values are for the FWHM. Table from [84]. . . . .	45
3.1	TE calibration constants and their relative uncertainties with the associated experimental production runs. . . . .	62
3.2	Summary of polarization uncertainties, not including uncertainties associated with TE quality check described in Sec. 3.1.2. Note that the major contributions for the polarization uncertainty comes from the TE measurements, hence are scaling uncertainties for the whole set of runs associated with the same calibration constant (Table 3.1). . . . .	64
3.3	Covariance matrices for 2.2 GeV (top) and 1.7 GeV (bottom) configurations. See text for the meaning of $A_1, A_2, A_3$ . The matrices are calculated with 5 MeV invariant mass cut at 2.2 GeV and 2.5 MeV invariant mass cut at 1.7 GeV. All values should be multiplied by $10^{-7}$ . . . . .	89
3.4	Systematic uncertainties due to invariant mass cut width. The uncertainties are given relative to the extracted asymmetries. . . . .	91
4.1	Proton asymmetries with their absolute statistical and systematic uncertainties.	96
4.2	$^{14}\text{N}$ elastic asymmetries with their absolute statistical and systematic uncertainties. . . . .	98

4.3	$^{14}\text{N}$ quasi-elastic asymmetries with their absolute statistical and systematic uncertainties. . . . .	98
4.4	A summary of asymmetry uncertainties for electron-proton elastic (a), electron- $^{14}\text{N}$ elastic (b) and electron- $^{14}\text{N}$ quasi-elastic scattering (c). The tables list ranges over the whole dataset, and specific total uncertainties are listed in Tables 4.1,4.2,4.3. . . . .	100

# Chapter 1

## Introduction

Early in the 20th century, an anomalous magnetic moment for the proton was measured by Estermann, Frisch, and Stern, to be

$$\mu_p = 2.79\mu_B, \tag{1.1}$$

where  $\mu_B$  is the Bohr magneton [1]. This discovery was the first evidence for the complex internal structure of the proton. In adjacent to this understanding, electron scattering experiments were used to probe the proton (and other nuclei) internal structure. Through the measurements of electromagnetic form factors and nucleon structure functions, using elastic and inelastic scattering experiments, the proton is understood as composed of three valence quarks interacting through the strong force. While perturbative quantum chromodynamics (pQCD) can make rigorous predictions for large momentum transfer squared,  $Q^2$ , where the quarks are effectively free [2], this cannot be done in the low  $Q^2$  regime, so phenomenological models are used in attempt to explain the data. Hence, precise measurements of proton elastic form factors and structure functions are essential to test and improve these models.

The proton elastic form factors were traditionally based on cross section measurements, and these efforts continue to this day. In the last three decades, advances in technologies of polarized beams and targets enabled new types of experiments which are based on spin degrees of freedom. In contrast to the cross section measurements, spin-dependent measurements provide the ratio between the form factors. This has several experimental advantages, mainly by eliminating some of the main cross section measurement systematics, and enabling the extraction of ratios at kinematic domains where the cross section is dominated by one of the individual form factors.

Differences between the results of the two methods at high momentum transfer prompted theoretical and experimental efforts to resolve this discrepancy [3–7]. At low momentum

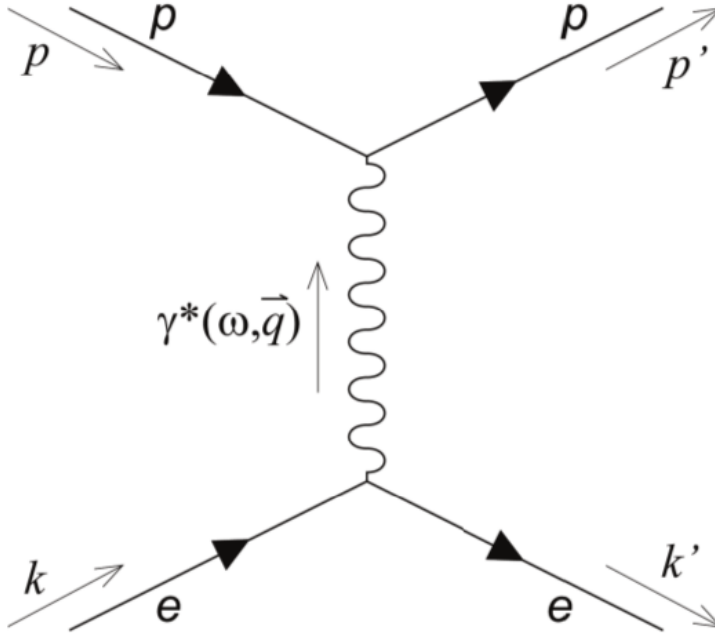


Figure 1.1: Leading order Feynman diagram for  $ep$  elastic scattering.

transfer, differences between high precision spin-dependent measurements of the ratios is observed. In addition, recent measurements of the proton charge radius based on the Lamb shift in muonic hydrogen resulted in significant deviation from the accepted results based on both scattering and atomic measurements using electrons [8, 9]. For these reasons, precise measurements of the proton form factors at low momentum transfer are required.

This report describes the second part of experiment E08-007 (GEp), which measured the proton form factor ratio at  $Q^2 = 0.02-0.08 \text{ GeV}^2$  using the double spin asymmetry technique. This  $Q^2$  region is the lowest ever measured using polarization techniques. The report will provide the relevant theoretical background and terminology, describe the experimental setup, and report the analysis approaches used to deal with the various challenges imposed by this complex experiment. Finally, preliminary results for the left arm asymmetries will be presented.

## 1.1 Definitions and Formalism

### 1.1.1 Electron Scattering

For the definition of the proton elastic form factors, we shall consider electron-proton ( $ep$ ) elastic scattering in the one-photon-exchange (OPE), or Born, approximation. In quantum

electrodynamics (QED), the leading order approximation for  $ep$  elastic scattering is described by the exchange of a single virtual photon, as shown in Fig. 1.1. The incoming and scattered electrons have four-momenta  $k^\mu = (E, \vec{k})$  and  $k'^\mu = (E', \vec{k}')$ , respectively, and the target and recoil protons have four-momenta  $p^\mu = (E_p, \vec{p})$  and  $p'^\mu = (E'_p, \vec{p}')$ . The four-momentum of the virtual photon is  $q^\mu = (\omega, \vec{q})$ . We define the four-momentum transfer squared,  $Q^2$  as (see Append. A)

$$Q^2 = -q_\mu q^\mu = -(\omega^2 - \vec{q}^2) = -k^\mu - k'^\mu = 4EE' \sin^2\left(\frac{\theta}{2}\right), \quad (1.2)$$

where the last expression is valid for ultra-relativistic electrons, and  $\theta$  is the scattering angle of the electron.

The OPE approximation is justified at low momentum transfer due to the small electromagnetic coupling constant  $\alpha \approx 1/137$ . As discussed in Sec. 1.3, discrepancies between cross section and polarization measurements suggests that the OPE approximation is not valid above  $Q^2 \sim 1 \text{ GeV}^2$ . For the scope of this experiment, however, this approximation is considered valid.

### 1.1.2 Formalism

The OPE amplitude for the  $ep$  elastic scattering is determined from the Feynman diagram in Fig. 1.1 to be

$$\begin{aligned} i\mathcal{M} &= [ie\bar{v}(p') \Gamma^\mu(p', p) v(p)] \frac{-ig^{\mu\nu}}{q^2} [ie\bar{u}(k') \gamma^\nu u(k)] \\ &= -\frac{i}{q^2} [ie\bar{v}(p') \Gamma^\mu(p', p) v(p)] [ie\bar{u}(k') \gamma_\mu u(k)], \end{aligned} \quad (1.3)$$

where  $\gamma^\mu$  are the Dirac matrices

$$\gamma^0 = \begin{pmatrix} 0 & 1 \\ 1 & 0 \end{pmatrix}; \gamma^i = \begin{pmatrix} 0 & \vec{\sigma} \\ -\vec{\sigma} & 0 \end{pmatrix} \quad (1.4)$$

$i = 1..3$ , and  $\vec{\sigma}$  are the Pauli matrices

$$\sigma_1 = \begin{pmatrix} 0 & 1 \\ 1 & 0 \end{pmatrix}; \sigma_2 = \begin{pmatrix} 0 & -i \\ i & 0 \end{pmatrix}; \sigma_3 = \begin{pmatrix} 1 & 0 \\ 0 & -1 \end{pmatrix} \quad (1.5)$$

$u(k)$  and  $u(k')$  are the Dirac spinors for the incoming and scattered electrons and  $v(p), \bar{v}(p')$  are the Dirac four-spinors for the target and the recoil protons. The proton spinors enter in the plane wave solution for a spin 1/2 particle:

$$\psi(x) = v(p)e^{-ip \cdot x}, \quad (1.6)$$

which satisfied the Dirac equation

$$(-i\gamma^\mu \partial_\mu - m) \psi(x) = 0, \quad (1.7)$$

and:

$$v(p) = \begin{pmatrix} \sqrt{p \cdot \bar{\sigma}} \chi \\ \sqrt{p \cdot \sigma} \chi \end{pmatrix} \quad (1.8)$$

with  $\sigma^\mu = (1, \vec{\sigma})$ ,  $\bar{\sigma} = (1, -\vec{\sigma})$  and  $\chi$  is a normalized two spinor such that

$$\chi^\dagger \chi = 1. \quad (1.9)$$

QED completely describes the leptonic current  $j_\mu = ie\bar{u}(k') \gamma_\mu u(k)$ . The hadronic current  $\mathcal{J}^\mu = ie\bar{v}(p') \Gamma^\mu(p', p) v(p)$ , however, which contains the information about the internal structure of the proton, is not known from QED. The symmetries of the electromagnetic interaction imply that the most general form of  $\Gamma^\mu$  is a linear combination of the vectors  $p$  and  $p'$ , and may contain constants such as the proton mass and charge. The Lorentz invariance implies that these are functions of a single scalar variable, conventionally chosen to be  $Q^2$ . An accepted form to write the hadronic current is [10]

$$\mathcal{J}^\mu = ie\bar{v}(p') \left[ \gamma^\mu F_1(Q^2) + \frac{i\sigma^{\mu\nu}}{2M_p} \kappa_p F_2(Q^2) \right] v(p), \quad (1.10)$$

where  $\sigma^{\mu\nu} = \frac{i}{2}[\gamma^\mu, \gamma^\nu]$ ,  $\kappa_p$  is the proton anomalous magnetic moment, and  $F_{1,2}(Q^2)$  are the proton elastic form factors. The elastic form factor contains the information about the electrodynamic structure of the proton.

### 1.1.3 Elastic Form Factors

The coupling of  $F_1$  to  $\gamma^\mu$  and  $F_2$  to  $\sigma^{\mu\nu}$  implies that  $F_1$  conserves helicity and  $F_2$  is responsible for the spin flip in the hadronic current. The form factors are normalized according to their static properties at  $Q^2 = 0$  to be:

$$F_{1p}(0) = 1 ; F_{2p}(0) = 1. \quad (1.11)$$

Similarly, the elastic form factor can be defined for the neutron with the normalization:

$$F_{1n}(0) = 0 ; F_{2n}(0) = 1. \quad (1.12)$$

Today, it is common to use an alternative definition of the form factor, suggested by Sachs [11] and by Hand, Miller and Wilson [12], and usually referred as the Sachs form factors:

$$\begin{aligned} G_E &= F_1 - \tau \kappa F_2, \\ G_M &= F_1 + \kappa F_2, \end{aligned} \quad (1.13)$$

where  $\tau = Q^2/4M_p^2$ . The Sachs form factors allow more simple interpretation of the form factors in a specific frame of reference, the Breit frame, as shown below. At  $Q^2 = 0$ , the Sachs form factors are normalized according to the static properties of the corresponding nucleon:

$$\begin{aligned} G_{E_p}(0) &= 1 ; G_{M_p}(0) = \mu_p \\ G_{E_n}(0) &= 0 ; G_{M_n}(0) = \mu_n \end{aligned} \quad (1.14)$$

### 1.1.4 Hadronic Currents

We can use the Gordon identity [10]

$$\bar{v}(p')\gamma^\mu v(p) = \bar{v}(p') \left[ \frac{p'^\mu + p^\mu}{2M_p} + \frac{i\sigma^{\mu\nu}q_\nu}{2M_p} \right] v(p) \quad (1.15)$$

to write

$$\bar{v}(p')\Gamma^\mu v(p) = \bar{v}(p') \left[ (F_1 + \kappa F_2)\gamma^\mu - \frac{(p + p')^\mu}{2M_p}\kappa F_2 \right] v(p) \quad (1.16)$$

The Breit frame is a frame of reference where the interaction only flips the sign of the nucleon three-momentum without changing its magnitude (see Appendix B). In the Breit frame, hadronic current is

$$\mathcal{J}^0 = ie\bar{v}(p') \left[ (F_1 + \kappa F_2)\gamma^0 - \frac{E_{pB}}{M_p}\kappa F_2 \right] v(p), \quad (1.17)$$

$$\vec{\mathcal{J}} = ie(F_1 + \kappa F_2)\bar{v}(p')\vec{\gamma}v(p), \quad (1.18)$$

where  $E_{pB}$  is the proton energy in the Breit frame. Since  $\bar{v}(p') = v^\dagger(p')\gamma^0$ , we get

$$\mathcal{J}^0 = ie \left[ (F_1 + \kappa F_2)v^\dagger(p')v(p) - \kappa F_2 \frac{E_{pB}}{M_p}v^\dagger(p')\gamma^0v(p) \right]. \quad (1.19)$$

We can now use the definitions of Eq. (1.4) and (1.8) to write

$$\begin{aligned} \mathcal{J}^0 &= ie(F_1 + \kappa F_2)\chi'^\dagger \left( \sqrt{p' \cdot \sigma} \cdot \sqrt{p' \cdot \bar{\sigma}} \right) \begin{pmatrix} \sqrt{p \cdot \sigma}\chi \\ \sqrt{p \cdot \bar{\sigma}}\chi \end{pmatrix} \\ &\quad - ie\kappa F_2 \frac{E_{pB}}{M_p}\chi' \left( \sqrt{p' \cdot \sigma} \cdot \sqrt{p' \cdot \bar{\sigma}} \right) \begin{pmatrix} 0 & 1 \\ 1 & 0 \end{pmatrix} \begin{pmatrix} \sqrt{p \cdot \sigma}\chi \\ \sqrt{p \cdot \bar{\sigma}}\chi \end{pmatrix}. \end{aligned} \quad (1.20)$$

Using the identities

$$M_p = \sqrt{p' \cdot \sigma} \cdot \sqrt{p \cdot \bar{\sigma}} = \sqrt{p' \cdot \bar{\sigma}} \cdot \sqrt{p \cdot \sigma}, \quad (1.21)$$

$$2E_{pB} = \sqrt{p' \cdot \sigma} \cdot \sqrt{p \cdot \bar{\sigma}} + \sqrt{p' \cdot \bar{\sigma}} \cdot \sqrt{p \cdot \sigma}, \quad (1.22)$$

$$\tau = \frac{Q^2}{4M_p^2} = \frac{q_B^2}{4M_p^2} = \frac{E_{pB}^2 - M_p^2}{M_p^2}, \quad (1.23)$$

where  $\vec{q}_B$  is the three-momentum of the virtual photon in the Breit frame, we find

$$\mathcal{J}^0 = 2ieM_p\chi'^\dagger\chi(F_1 - \tau\kappa F_2) = 2ieM_p\chi'^\dagger\chi G_E. \quad (1.24)$$

Similarly, we get

$$\vec{\mathcal{J}} = -e\chi'^\dagger(\vec{\sigma} \times \vec{q}_B)\chi(F_1 + \kappa F_2) = -e\chi'^\dagger(\vec{\sigma} \times \vec{q}_B)\chi G_M. \quad (1.25)$$

These results enables a simple interpretation of the Sachs form factors in the Breit frame. In this frame,  $G_E$  contains the information of the electric charge distribution, and  $G_M$  contains the information of the magnetic currents distribution. In this frame we can associate the form factors with the Fourier transforms of these distributions:

$$G_{E,M}(Q^2) = \int \rho(\vec{r})_{E,M} e^{i\vec{q}\vec{r}} d^3r = \int \rho(\vec{r})_{E,M} d^3r - \frac{\vec{q}^2}{6} \int \rho(\vec{r})_{E,M} r^2 d^3r + \dots \quad (1.26)$$

The first term in this expansion is the total charge (or magnetic moment), while the second term defines the charge and magnetic radii of the nucleon. However, this simplified interpretation loses its meaning when moving to other, more physical, frame of references.

## 1.2 Measurement Techniques

### 1.2.1 Rosenbluth Separation

The traditional form factor measurement technique is referred to as the Rosenbluth separation [13]. This method was the only method used until the 1990s and is still in use today. To understand the principle of the Rosenbluth separation technique, we shall start with the cross section for  $ep$  elastic scattering, as calculated by [10]

$$\frac{d\sigma}{d\Omega} = \frac{\langle |\mathcal{M}|^2 \rangle}{64\pi^2} \left( \frac{E'}{E} \right) \frac{1}{M_p}. \quad (1.27)$$

In the OPE approximation, the cross section can be written [13]

$$\frac{d\sigma}{d\Omega} = \left( \frac{d\sigma}{d\Omega} \right)_{Mott} \frac{E'}{E} \left[ F_1^2(Q^2) + 2(F_1(Q^2) + f_2(Q^2))^2 \tan^2 \frac{\theta}{2} \right], \quad (1.28)$$

where the Mott cross section,  $(d\sigma/d\Omega)_{Mott}$ , is the cross section for electron scattering off a spin 1/2 point-like target

$$\left( \frac{d\sigma}{d\Omega} \right)_{Mott} = \left( \frac{e^2}{2E} \right)^2 \left( \frac{\cos^2 \frac{\theta}{2}}{\sin^4 \frac{\theta}{2}} \right). \quad (1.29)$$

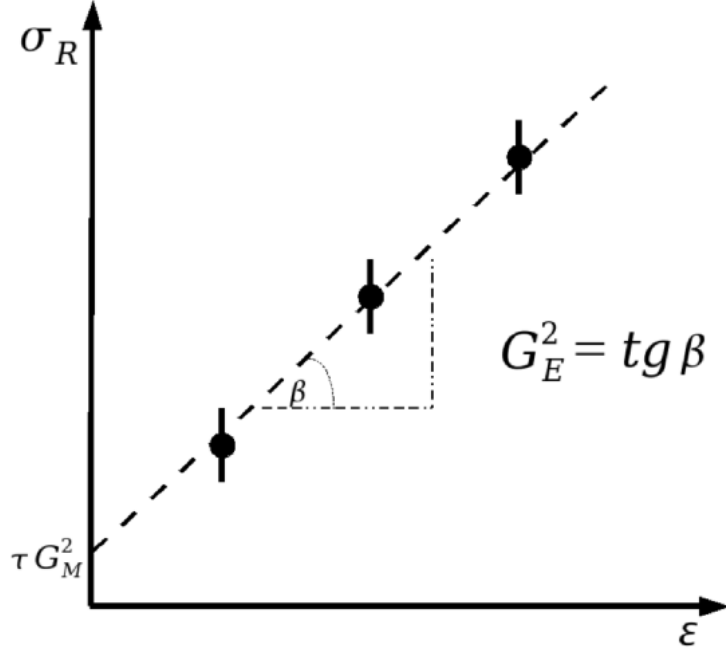


Figure 1.2: Illustration of the Rosenbluth separation method.

Using the definition of the Sachs form factors (Eq. 1.13), Eq. 1.28 becomes

$$\frac{d\sigma}{d\Omega} = \frac{\alpha^2}{Q^2} \left( \frac{E'}{E} \right)^2 \left[ 2\tau G_M^2 + \frac{\cot^2 \frac{\theta}{2}}{1 + \tau} (G_E^2 + \tau G_M^2) \right], \quad (1.30)$$

where  $\alpha = e^2/4\pi$  is the electromagnetic fine structure constant. The advantage of this representation is that there is no interference term, allowing a simple separation of the Sachs form factors.

We further define the "reduced cross section" as

$$\sigma_{red} = (1 + \tau) \frac{d\sigma/d\Omega}{(d\sigma/d\Omega)_{Mott}} = G_E^2 + \frac{\tau}{\epsilon} G_M^2, \quad (1.31)$$

where  $\epsilon \equiv [1 + 2(1 + \tau) \tan^2(\theta/2)]^{-1}$  is the virtual photon polarization. As mentioned above, the Mott cross section is the cross section for scattering off a point-like target. Hence, the reduced cross section isolates the contribution of the internal structure, represented by the Sachs form factors, to the cross section. Since  $\tau$  and  $Q^2$  are kinematic parameters controllable experimentally by changing beam energy and scattering angle, it is possible to produce a set of measurements with the same  $Q^2$  and a linear correlation between  $\sigma_R = \epsilon \sigma_{red}$  and  $\epsilon$ . From a linear fit to such set of measurements, the Sachs form factors can be extracted (See Fig. 1.2). This experimental technique is called "Rosenbluth separation".

Although the Rosenbluth separation technique was and still is a successful method for form factor measurements, it has several disadvantages. The main disadvantage is the need

for a cross section measurement, which is an absolute measurement. Absolute measurements suffer several systematic difficulties like absolute normalizations as well as acceptance and efficiency uncertainties. The need for several  $\epsilon$  data points with the same  $Q^2$  involves measurements at different angles and/or beam energies, and all these systematics must be well understood in order to use them for the same form factor extraction. An additional disadvantage is that the contribution of  $G_M$  is scaled by  $\tau/\epsilon$ , which implies low sensitivity for  $G_E$  at high  $Q^2$  and low sensitivity for  $G_M$  at low  $Q^2$ .

### 1.2.2 Polarization transfer measurements

Alternative methods for form factor measurements are based on spin degrees of freedom and are focused on the interference term of the form  $G_E G_M$ . Akheizer and Rekalov [14] suggested the use of a longitudinally polarized electron beam, and measuring the polarization components of the recoil proton from the reaction  $\vec{e} + p \rightarrow e' + \vec{p}$ . The polarization of the recoil proton can be expressed, in the coordinate system defined in Fig. 1.3, as [15]

$$\mathbf{P} \equiv \begin{pmatrix} C_x \\ P_y \\ C_z \end{pmatrix}, \quad (1.32)$$

where  $P_y = 0$  (in the OPE approximation), and

$$\sigma_{red} C_x = -2h \cot \frac{\theta}{2} \sqrt{\frac{\tau}{1+\tau}} G_E G_M \quad (1.33)$$

$$\sigma_{red} C_z = h \frac{E + E'}{M_p} \sqrt{\frac{\tau}{1+\tau}} G_M^2, \quad (1.34)$$

$\sigma_{red}$  is defined in 1.31, and  $h$  is the value of the beam polarization defined as

$$h = \frac{N_R - N_L}{N_R + N_L}, \quad (1.35)$$

where  $N_{R(L)}$  is the number of electrons with right (left) handed helicity. By simultaneously measuring both polarization components, and by taking the ratio between them, one can obtain the form factor ratio:

$$\mu_p \frac{G_E}{G_M} = -\mu_p \frac{E + E'}{2M_p} \frac{C_x}{C_z} \tan \frac{\theta}{2}. \quad (1.36)$$

The advantage of this method is that only a single measurement is required for each  $Q^2$  point, and it eliminates the systematics associated with absolute cross section measurements. Furthermore, the interference term is not suppressed at any  $Q^2$ . On the other hand, this method does not provide information on the individual form factors.

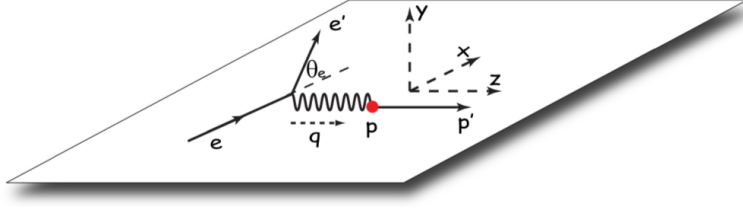


Figure 1.3: Coordinate system for the recoil polarization measurement.

### 1.2.3 Double Spin Asymmetry

Although the recoil polarization method can, in principle, extract the form factor ratio at any  $Q^2$ , this requires a measurement of the recoil proton polarization. This is a limitation at very low  $Q^2$ , where the energy transfer is low, and the proton does not acquire enough energy to exit the target material and reach the polarimeter. A different method, also based on spin degrees of freedom, is called the Double Spin Asymmetry (DSA). In a 1985 paper, Donnelly and Raskin [16] suggested using a longitudinally polarized electron beam with a polarized proton target, and measure the asymmetry in the cross section between the two helicity states.

The helicity of the electron is defined as the projection of the electron spin along its momentum direction, and can be either positive or negative for a longitudinally polarized electron beam,  $h = \pm 1$ . The differential cross section for elastic scattering can be written as:

$$\frac{d\sigma}{d\Omega} = \Sigma \pm h\Delta, \quad (1.37)$$

where  $\Sigma$  is the unpolarized cross section in Eq. 1.30, and the spin-dependent contribution  $\Delta$  is given by [16]:

$$\Delta = -\Sigma f_1 \frac{aF_T^2 + bF_L F_T}{F^2} \quad (1.38)$$

with the following definitions (in the ultra-relativistic approximation)<sup>1</sup>:

$$f_1 = \frac{1}{\sqrt{2}}, \quad (1.39)$$

$$v_L = \left(\frac{Q^2}{q^2}\right)^2, \quad (1.40)$$

$$v_T = -\frac{1}{2} \left(\frac{-Q^2}{q^2}\right) + \tan^2 \frac{\theta}{2}, \quad (1.41)$$

<sup>1</sup>When comparing with the original work by Donnelly and Raskin, note that the definition of  $Q^2$  uses opposite signs relative to the notations in this report.

$$v_{TL} = \frac{1}{\sqrt{2}} \left( \frac{-Q^2}{q^2} \right) \sqrt{\frac{Q^2}{q^2} + \tan^2 \frac{\theta}{2}}, \quad (1.42)$$

$$v_{T'} = \sqrt{\frac{Q^2}{q^2} + \tan^2 \frac{\theta}{2}} \tan \frac{\theta}{2}, \quad (1.43)$$

$$v_{TL'} = \frac{1}{\sqrt{2}} \left( \frac{-Q^2}{q^2} \right) \tan \frac{\theta}{2}, \quad (1.44)$$

$$F_L = \frac{1 + \tau}{\sqrt{4\pi}} G_E, \quad (1.45)$$

$$F_T = \frac{-\sqrt{2\tau(1 + \tau)}}{\sqrt{4\pi}} G_M, \quad (1.46)$$

$$F^2 = v_L F_L^2 + v_T F_T^2, \quad (1.47)$$

$$a = \sqrt{2} v_{T'} \cos \theta^*, \quad (1.48)$$

$$b = 2\sqrt{2} v_{TL'} \sin \theta^* \cos \phi^*. \quad (1.49)$$

In the above terms, we use both the scattering angle of the electron in the lab frame,  $\theta$ , and the spherical coordinates  $(\theta^*, \phi^*)$  of the polarization axis relative to the virtual photon direction, as illustrated in Fig. 3.6.

With the results above, one can use the asymmetry between the cross sections of the different helicities to write:

$$A = \frac{\sigma^+ - \sigma^-}{\sigma^+ + \sigma^-} = \frac{\Delta}{\Sigma}, \quad (1.50)$$

$$A = f_1 \frac{aF_T^2 + bF_L F_T}{F^2} = f_1 \frac{aF_T^2 + bF_L F_T}{v_L F_L^2 + v_T F_T^2}. \quad (1.51)$$

Dividing by  $F_T^2$  we get:

$$A = f_1 \frac{a + b \frac{F_L}{F_T}}{v_L \left( \frac{F_L}{F_T} \right)^2 + v_T}, \quad (1.52)$$

which is a function of the form factor ratio  $G_E/G_M$ . Using this relation, the DSA technique enables the extraction of the proton elastic form factor ratio using only a measurement of the scattered electron, without the need to detect the recoil proton, hence allowing the extraction of the ratio at even lower  $Q^2$  regions. The DSA technique is the one used for this experiment.

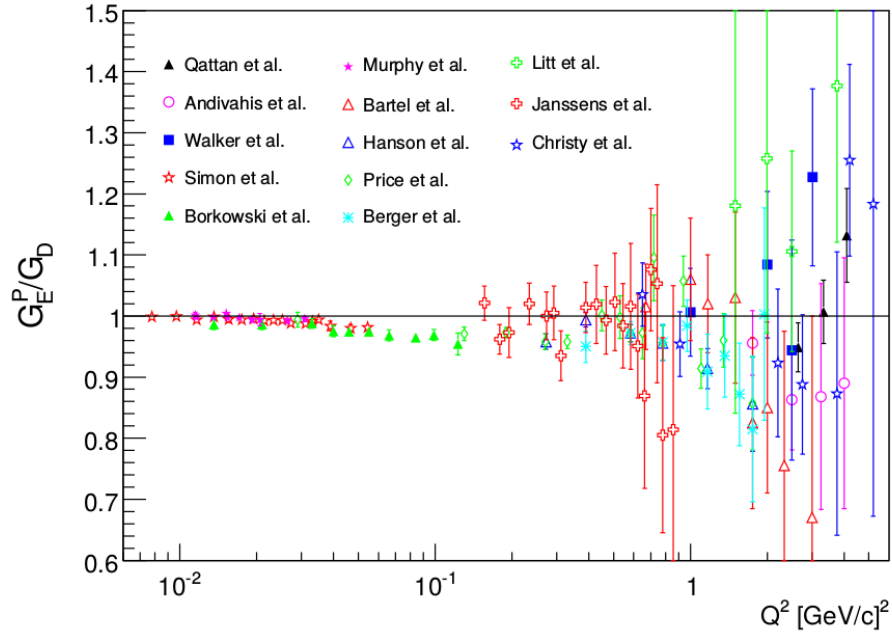


Figure 1.4: World data for proton  $G_E$  from unpolarized measurements [17–29], using the Rosenbluth method, normalized to the dipole parameterization. Figure from [30].

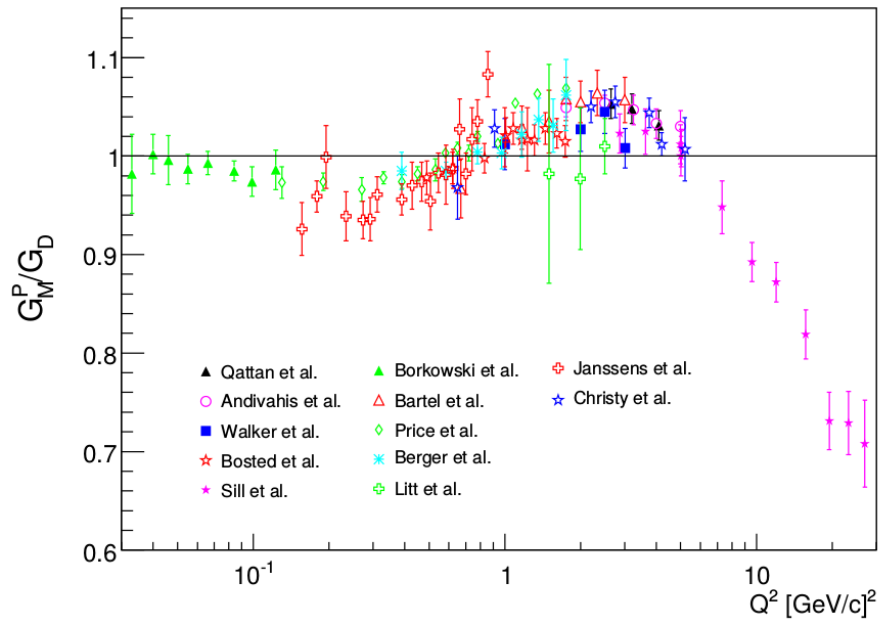


Figure 1.5: World data for proton  $G_M$  from unpolarized measurements [17, 19, 21, 23, 25–29, 31, 32], using the Rosenbluth method, normalized to the dipole parameterization. Figure from [30].

## 1.3 World Data

### 1.3.1 World Data

Experimental form factors based on Rosenbluth separation are shown in Figs. 1.4,1.5. The results are scaled to the dipole parametrization, which is considered a reasonable approximation for the form factors. The dipole parametrization describes an exponential distribution of the charge or magnetization densities, and has the form:

$$G_D = \left(1 + \frac{Q^2}{0.71\text{GeV}^2}\right)^{-2}. \quad (1.53)$$

The parameter 0.71 is an empirical parameter, fit to reproduce the experimental values obtained by cross section measurements within an accuracy of  $\sim 10\%$  up to about 10 GeV<sup>2</sup>.

The more recent polarization transfer measurements were done at the MIT-bates [34–36] facility, MAMI facility [37, 38] and at Jefferson Lab [39–46]. Fig. 1.6 shows the results obtained by these experiments, relative to the Rosenbluth separation results. Unlike the Rosenbluth results, a clear decline in the ratio as  $Q^2$  increases is evident for the polarization data. This discrepancy has been the focus of much theoretical and experimental work [3–7]. It is today considered most probable that the OPE approximation is not valid at this  $Q^2$  region, and Two-Photon-Exchange (TPE) corrections are required. A re-analysis of the Rosenbluth results with a TPE correction is shown in Fig. 1.6.

Fig. 1.7 shows the current data from polarization measurements, fits, and models for the form factor ratio at low  $Q^2$ . Differences between spin-dependent measurements of the ratios are evident. This region is a subject of increased interest in recent years, due to high precision measurements of the proton radius by muonic hydrogen Lamb shift measurements [8, 9]. These measurements show a  $7\sigma$  deviation of the proton charge radius relative to the values extracted by electron scattering and Lamb shift measurements (see Fig. 1.8). As mentioned above, the polarization measurements at low momentum transfer contribute mainly to the extraction of  $G_M$ , while the proton radius problem impacts the charge radius. However, there is a possibility that the origin of the discrepancy with the radii is the way that fits are done at the region of  $Q^2 \rightarrow 0$ . Since the proton RMS radius is defined by the slope of the form factor as  $Q^2 \rightarrow 0$  (Eq. 1.26), precise knowledge of the functional behavior at low  $Q^2$  is required for reliable comparison between the scattering data and the Lamb shift data. Constraining  $G_M$  at low  $Q^2$ , and constraining  $G_E/G_M$  in models and fits at low  $Q^2$ , will improve the reliability of the extraction of the slope in fits and models.

Additional recent work by Bernauer *et al.* at MAMI [55], performed a large survey consisting of  $\approx 1400$  data points at the low  $Q^2$  region, using unpolarized electron scattering

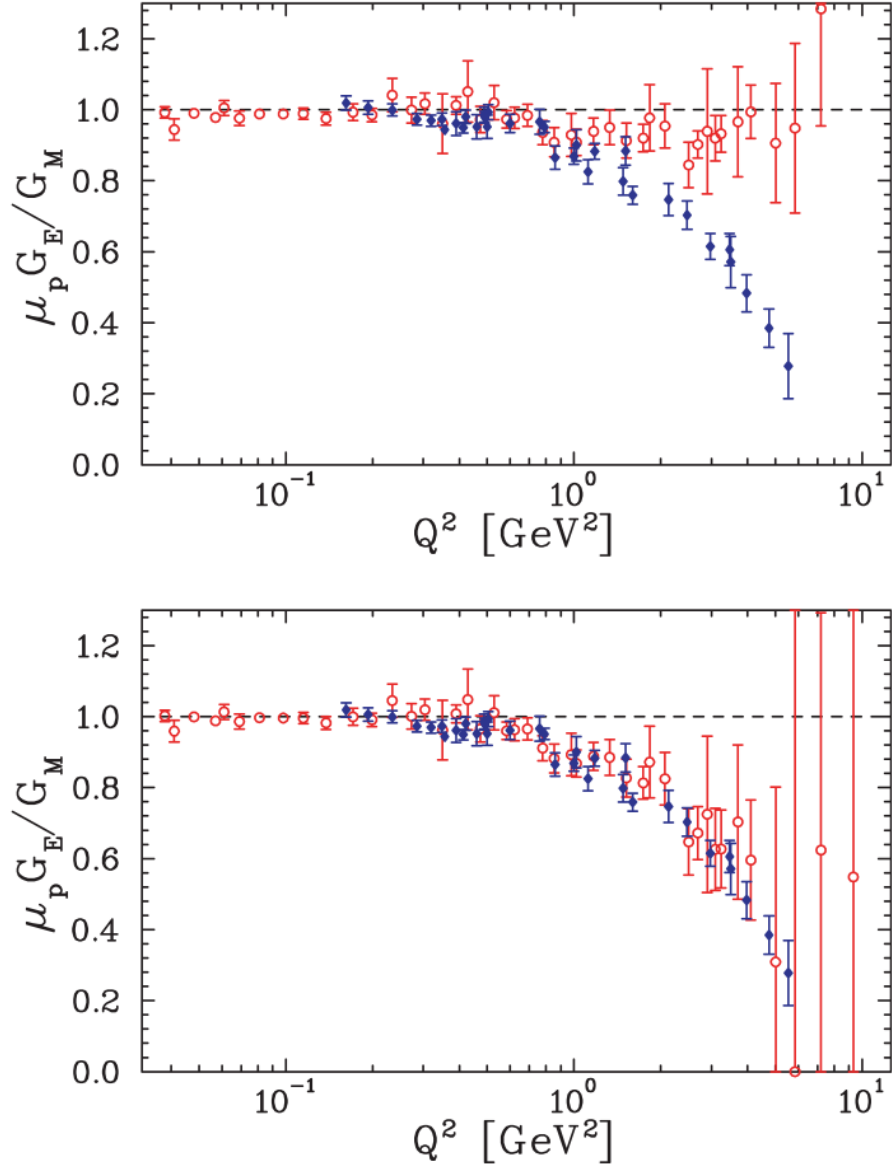


Figure 1.6: Ratio  $\mu G_E/G_M$  extracted from polarization transfer (filled blue diamonds) and Rosenbluth method (open red circles). The top (bottom) figures show Rosenbluth method data without (with) TPE corrections applied to the cross sections. Figures from [33].

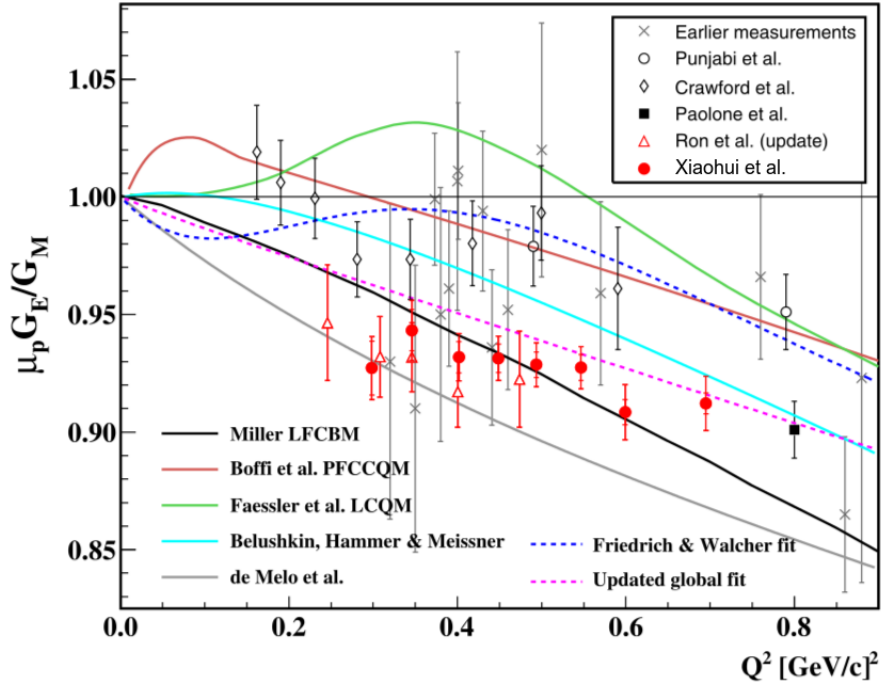


Figure 1.7: Low  $Q^2$  polarization measurements of  $\mu G_E/G_M$ , models and fits [34, 35, 37–39, 42, 45–52]. Figure from [45]

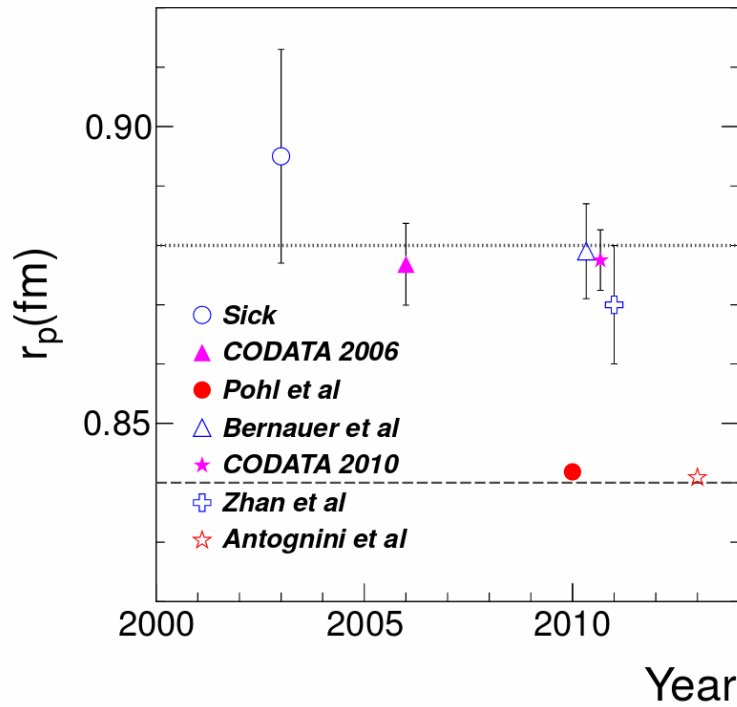


Figure 1.8: A summary of some recent proton charge radius determinations: Sick [53], CODATA 2006 [54], Pohl et al. [8], Bernauer et al. [55], CODATA 2010 [56], Zhan et al. [45], and Antognini et al. [9]. Figure from [57].

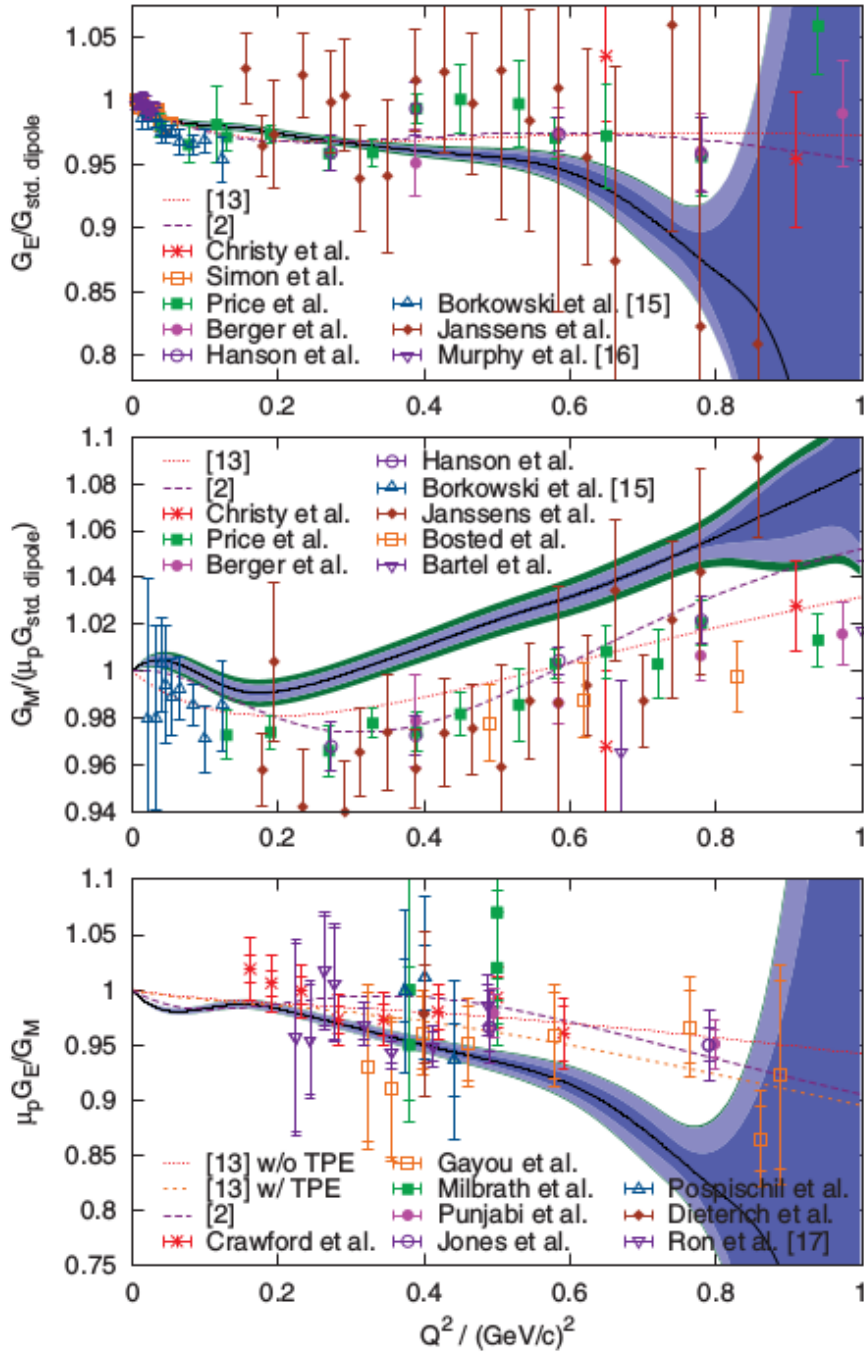


Figure 1.9: The form factors  $G_E$  and  $G_M$  normalized to the standard dipole and  $G_E/G_M$  as a function of  $Q^2$ , as measured by [55]. Black line: best fit to the data, blue area: statistical 68% pointwise confidence band, light blue area: experimental systematic error. The different data points depict previous measurements. Dashed lines are previous fits to the old data in. Figures and refs. from [55].

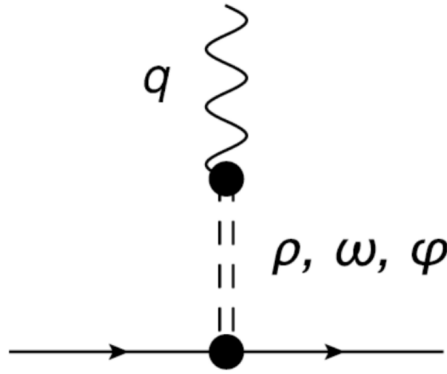


Figure 1.10: Vector meson dominance picture for the coupling of the photon to a nucleon. Figure from [58].

measurements. The extraction of the form factors was not done by the Rosenbluth separation technique, but by a simultaneous fit of a large variety of form factor models directly to the cross sections. Fig. 1.9 shows the results of this survey, which claims excellent precision for both  $G_E$  and  $G_M$  at low  $Q^2$ . However, these results are not in agreement with  $G_M$  values extracted by previous experiments, and the small error band might be a result of the limited number of parameters in the fit relative to the large number of data points, and the normalization constraint  $\mu G_M(0) = 1$ .

### 1.3.2 Models and Fits

While pQCD gives predictions for the nucleon form factors at high  $Q^2$ , and QCD effective theories can, in principle, give predictions in the very low  $Q^2$  region, in the intermediate  $Q^2$  region this task is much harder. Several QCD-inspired models, phenomenological models, and empirical fits suggested to provide prediction of the form factor behavior in this  $Q^2$  regime. References [3, 7, 58] summarize in details these efforts. Here we will give a brief overview of the main models and fit approaches in this field.

#### Vector Meson Dominance (VMD)

The VMD model is based on the understanding that the lowest lying vector mesons,  $\rho, \omega$ , and  $\phi$ , are prominent in the process  $e^+e^- \rightarrow$  hadrons at the relevant time-like values of the CM energy squared  $q^2 > 0$ . It is likely then that much of the behavior of the coupling at low space-like momentum transfer could be explained by the virtual photon converting to a strongly interacting meson which then interacts with the nucleon, as illustrated in Fig. 1.10. Early VMD models used single vector meson exchange with simple couplings giving

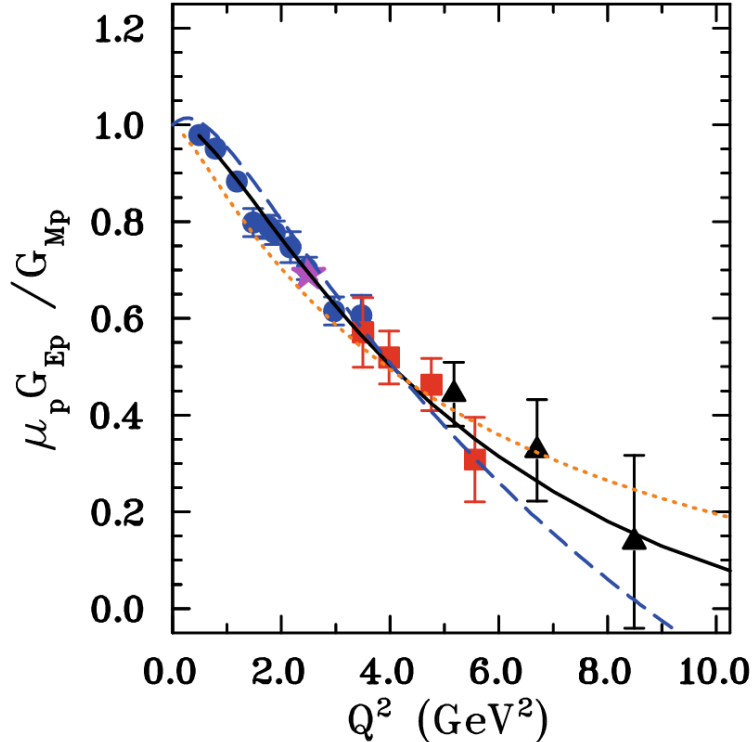


Figure 1.11: Several VMD fits compared to the JLab  $\mu G_E/G_M$  data. The solid curve (black) is the fit of Lomon [62], the dashed curve (blue) is that of Iachello, Jackson, and Lande [59], and the dotted curve (red) is that of Bijker and Iachello [63]. Figure from [58].

an  $m_V^2/(m_V^2 - q^2)$  factor from its propagator, for the falloff of the form factor, while more recent ones added more complexity to the propagator [59], and included excited states of the mesons [60]. These models show good agreement with data, and had some success in predicting the form factor behavior in the past, but are inconsistent with general constraints from unitarity [61]. Fig. 1.11 shows some recent results from VMD models.

### 1.3.3 Constituent Quarks Models (CQMs)

Constituent quark models refer to the nucleon as the ground state of a quantum mechanical three-quark system in a confining potential. The proton is described to be composed of three light quarks, which are described by an  $SU(6)$  flavor wave function and a completely anti-symmetric color wave function. Form factor calculations based on CQM require a realistic treatment of the proton, that takes into account the fact that the quarks are relativistic, due to their small mass scale as compared to the confinement mass scale. Relativistic transformation of the wave function in the rest frame to the moving frame is not trivial, and three main approaches are used to produce predictive models based on CQM:

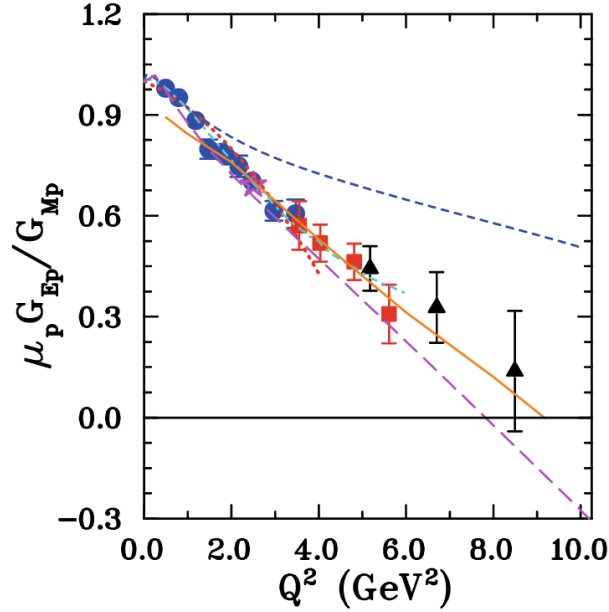


Figure 1.12: The JLab  $\mu G_E/G_M$  data compared to the results of some constituent quark models. The short dashed curve (blue) is from Boffi et al. [49], the solid (orange) from de Melo et al. [52], the long dash (magenta) from Gross et al. [64], the dotted (red) from Chung and Coester [65], and the dash-dot (cyan) from Cardarelli et al. [66]. Figure from [58].

- The point form: In this approach, all boosts and rotations are dynamical, meaning that as operators in a field theory they can be written without having to know their interactions. As a consequence, their angular momenta and Lorentz boosts are the same as in the free case. The cost is that all four components of the momentum operators are interaction dependent.
- The instant form: In this approach, the rotation operators and space components of the momenta are dynamical. As a consequence, dealing with angular momentum is easy, at the cost of including interaction effects for the boosts.
- The light-front form: In this approach, seven generators are dynamical, while the other three, which contain the interaction, one component of the four-momentum and 2 transverse rotations, are kinematical. The advantage of the light-front form is that states are simply transformed between frames of reference, but angular momenta are hard to construct.

The simplicity of state transformation makes the light-front form the most attractive for form factor calculations, and several calculations based on this approach were published [65, 67]. Improvement of these models is obtained by introducing form factors for the quarks

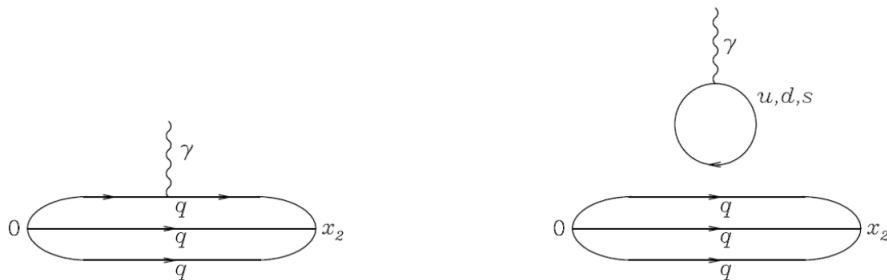


Figure 1.13: Connected (left) and disconnected (right) lattice diagrams.

[66, 68]. Other works added Goldstone bosons, which arise as effective degrees of freedom of low-energy QCD from spontaneous chiral symmetry breaking [69]. Some results from these methods are shown in Fig. 1.12.

### 1.3.4 Lattice QCD

The lattice QCD approach is to use computational resources to perform path integral calculation, on a discretized space-time lattice [70]. The calculation starts with (today artificial) quark masses and the coupling constants. The calculation is repeated with different lattice spacing,  $a$ , to allow extrapolation to  $a = 0$ .

The calculation of nucleon form factors requires evaluation of three-point functions, which have both connected and disconnected contributions (see Fig. 1.13). For connected diagrams, the photon couples to one of the valence quarks in the initial or final nucleon. For the disconnected diagrams, the photon couples to a sea quark  $q\bar{q}$  loop which then exchanges a gluon with the valence quark lines. The disconnected diagrams are incalculable today due to computational limitations. However, since these diagrams are the same for protons and neutrons, it is possible to take the differences between their form factors and cancel the effect of the disconnected diagrams. Thus, with today's computational capabilities, only isovector form factor can be calculated using lattice QCD.

### 1.3.5 Fits

There exist different fits for the form factors and their ratios, which are not necessarily based on models, but are useful for the sake of calculating cross sections and other form factor related quantities. There is discussion about what kind of functions can be used for this task, since these functions usually do not show the complete physical behavior expected by theory. We will try to list here the more common functional forms in use.

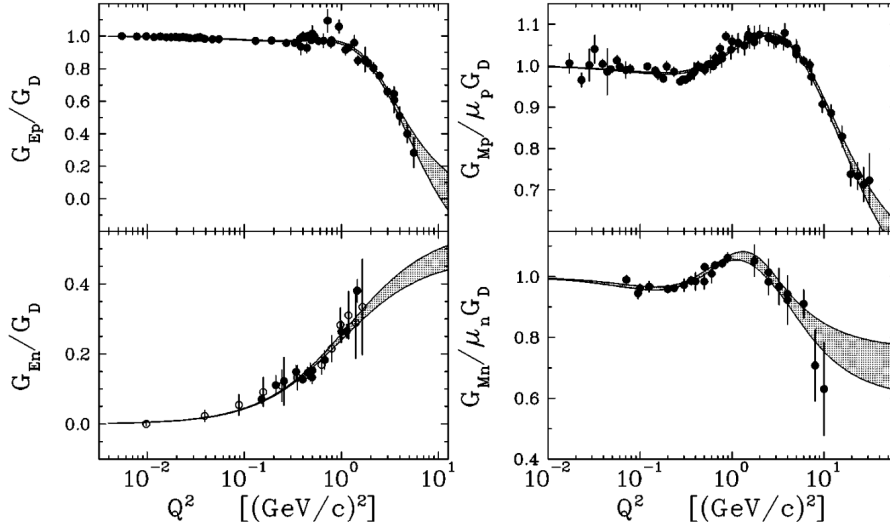


Figure 1.14: Fits to nucleon electromagnetic form factors. For  $G_{E_n}$ , data using recoil or target polarization [72–78] are shown as filled circles while data obtained from the deuteron quadrupole form factor [79] are shown as open circles. Figure from [71].

Kelly proposed the simple parametrization [71]:

$$G(Q^2) \propto \frac{\sum_{k=0}^n a_k \tau^k}{1 + \sum_{k=1}^{n+2} b_k \tau^k}. \quad (1.54)$$

In this parametrization, both numerator and denominator are polynomials in  $Q^2$  and the behavior at large  $Q^2$  is proportional to  $Q^{-4}$  as expected from theory [71]. Fig. 1.14 shows good agreement with data using only four parameters for  $G_{E_p}$ ,  $G_{M_p}$ , and  $G_{M_n}$ , and only two for  $G_{E_n}$ .

Arrington and Sick [80] performed a continued fraction fit:

$$G(Q) = \frac{1}{1 + \frac{b_1 Q^2}{1 + \frac{b_2 Q^2}{1 + \dots}}}. \quad (1.55)$$

This fit is good for the low momentum transfer region, and extends up to  $Q = \sqrt{Q^2} \approx 0.8$  GeV. They also include TPE correction for the Rosenbluth form factor.

There are also fits that take into account physical considerations of the expected analytical behavior of the form factors except for cuts at the time-like region, which begin where one can have a  $\pi \rightarrow 2\gamma$  transition at  $q^2 = 4m_\pi^2$ . Such effects leads to the use of the conformal variable  $z$ , defined as [81, 82]:

$$z(t, t_{cut}) = \frac{\sqrt{t_{cut} - t} - \sqrt{t_{cut} t}}{\sqrt{t_{cut} - t} + \sqrt{t_{cut} t}}, \quad (1.56)$$

where  $t_{cut} = 4m_\pi^2$ . Interestingly, the fit performed by Lorentz [82] yields a proton radius of  $0.840 \pm 0.015$  fm, in agreement with the muonic Lamb shift results, albeit with a  $\chi^2$  that indicates only moderate agreement with the data. However, this result was criticized by Bernauer and Distler [83] for being inconclusive.

# Chapter 2

## Experimental Setup

### 2.1 Setup

The goal of the GEp experiment was to measure the proton elastic form factor ratio at a  $Q^2$  range of 0.01-0.08 GeV<sup>2</sup>, using the Double Spin Asymmetry (DSA) technique (see Sec. 1.2.3). The experiment was performed in Hall A of the Continuous Electron Beam Accelerator Facility (CEBAF) at the Thomas Jefferson National Accelerator Facility, Newport News, VA (Sec. 2.3). A schematic view of the experimental setup is shown in Fig. 2.1. The CEBAF polarized beam at energies of 1.1, 1.7 and 2.2 GeV passed through fast and slow rasters (2,3, Sec. 2.4.2), reaching two chicane magnets (7, Sec. 2.4.4) compensating for the effect of the target magnetic field. The electrons, scattered off the polarized NH<sub>3</sub> target (9, Sec. 2.5), and bent by the septum magnet (10, Sec. 2.6) enters one of two High Resolution Spectrometers, HRSs (13, Sec. 2.4.5), and were detected by the detection package (14, Sec. 2.4.5). A detailed description of each component follows.

Between runs, Møller measurements were taken to determine beam polarization level (5). See Sec. 2.4.3 for details.

The GEp experiment ran at relatively low currents ( $\sim 10$  nA), hence no reliable beam position information could be extracted (6,8). Also, asymmetry measurements do not require absolute current normalization, so current information was not used for the analysis of this experiment (1,4). Another scintillator was positioned in the backward direction for the g2p experiment (12). All the components will not be detailed here, and the reader is referred to Hall A [84] and g2p [85, 86] documentation for a discussion of these components.

The GEp experiment ran alongside the g2p experiment [85, 86], and several aspects of the analysis were performed jointly with this experiment.

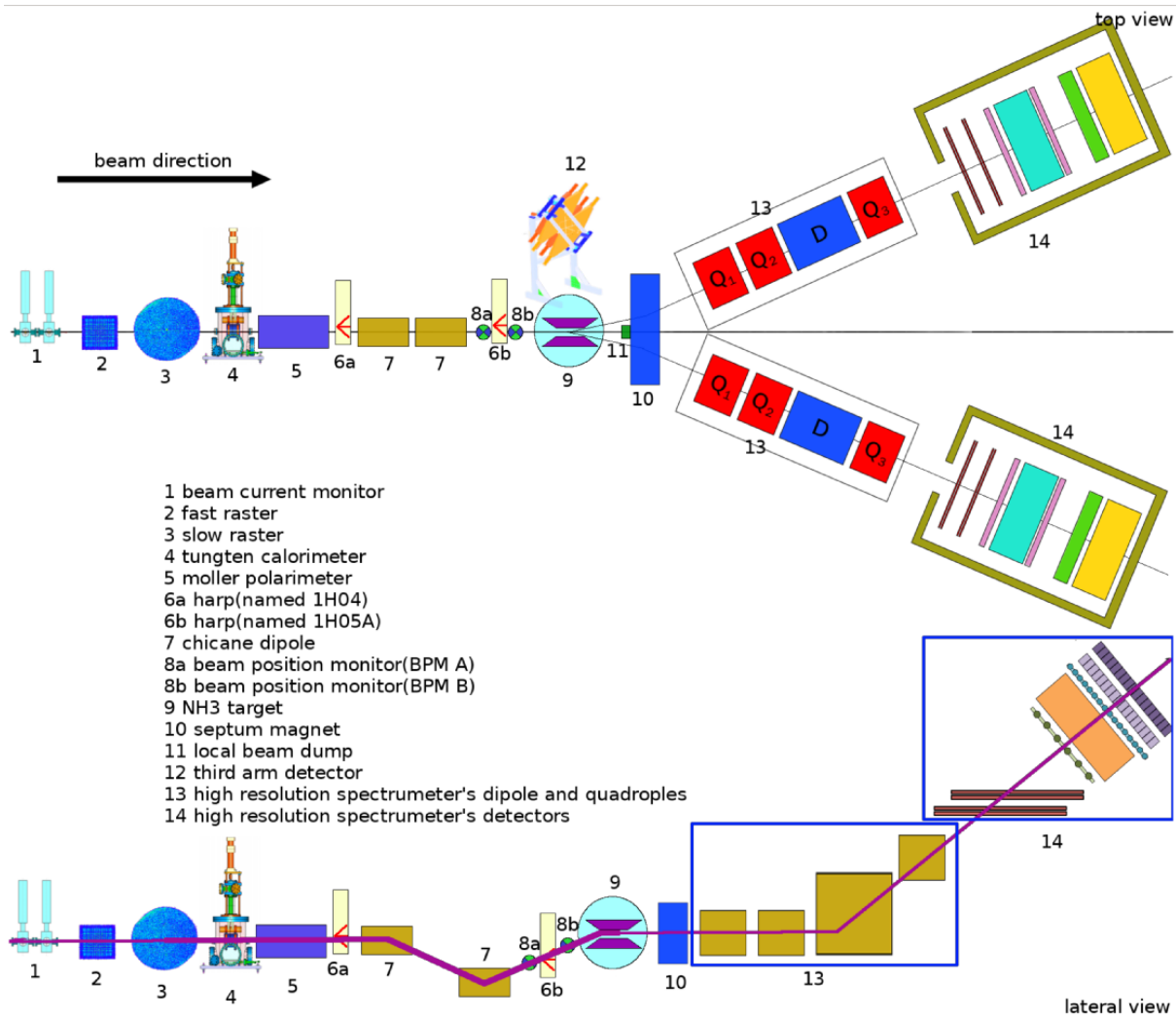


Figure 2.1: Schematic diagram of the GEp experimental setup. See text for description.

E (GeV)	arm	$\theta$ (deg)	$\theta^*$ (deg)	$\phi^*$ (deg)	E' (GeV)	$Q^2$ (GeV <sup>2</sup> )
2.253	left	6.0	85.7	0.3	2.224	0.055
1.712	left	6.0	87.3	0.6	1.695	0.032
1.157	left	7.4	89.0	0.6	1.145	0.022

Table 2.1: Central kinematics for the left arm.  $\theta$  is the scattering angle, while starred angles are the angles of the proton polarization axis relative to the recoil direction (see Sec. 1.1.2). Note that average values are different due to cross section weighting.

## 2.2 Kinematics

During the entire experiment, two HRs were tuned to detect elastic scattering at angles around 6 degrees. The experiment ran at 1.1, 1.7 and 2.2 GeV, central kinematics (i.e., the kinematics at the center of the acceptance) are listed in Table 2.1. Note that central kinematics are not the average values, which are affected by the cross section's strong dependence on the scattering angle (see Eq. (1.28)).

## 2.3 CEBAF

The Continuous Electron Beam Accelerator Facility (CEBAF) at Jefferson Lab [87] is composed of two superconducting electron linear accelerators, which are capable of delivering a 100% duty factor, polarized or unpolarized beam, to three experimental halls. Each linac contains 20 cryomodules with an average cavity gradient of 7.5 MV/m. The beam recirculates in a race-track shaped track for a total energy of up to about 6 GeV (See Fig. 2.2). (After this experiment, CEBAF was upgraded to 12 GeV [88]). After gaining proper energy, the beam is delivered to one (or more) of three experimental halls (today four), at currents of 1-150  $\mu$ A for two of the halls and 1-100 nA for the other.

The electron source is either a thermionic or a polarized gun. With the polarized gun (as used in this experiment) a strained GaAs cathode is illuminated by a 1497 MHz gain-switched diode laser, operated at 780 nm. The usage of a right or left circularly polarized laser light determines the electron helicity, and a polarization level of up to 80%-90% was achieved for this experiment. Electron helicity was pseudo-randomly flipped at a rate of 960.015 Hz. Occasionally, a half-wave plate (HWP) was inserted into the injector, to flip the helicity sign, and used for an additional systematic check of the obtained asymmetries.

## MACHINE CONFIGURATION

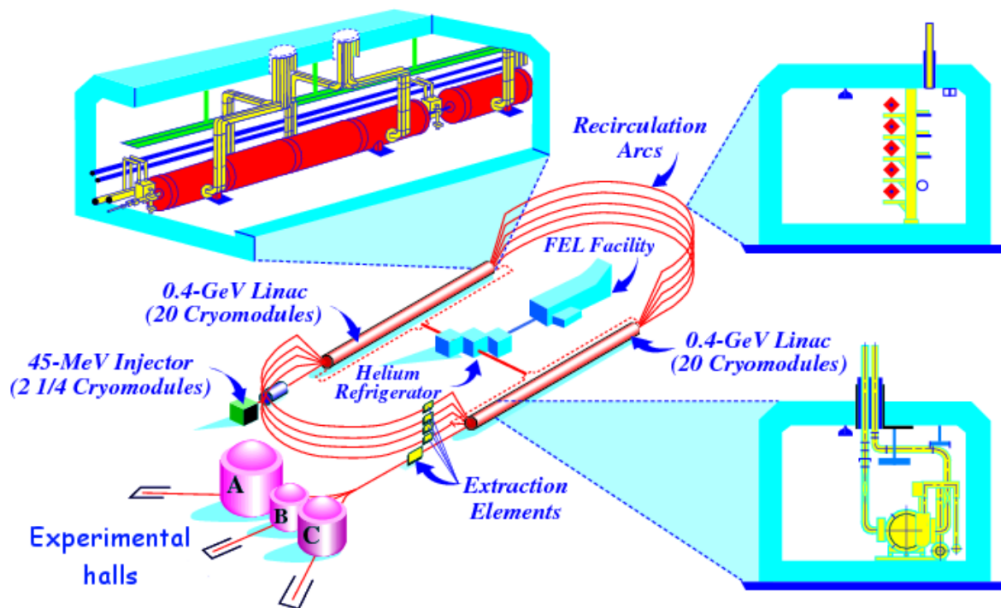


Figure 2.2: Schematic diagram of the Continuous Beam Accelerator Facility (CEBAF) at Jefferson Lab. The electron beam is produced by a Ti:Sap laser at the injector and further accelerated in each of two superconducting linacs. The beam can be extracted simultaneously to each of the three (today four) experimental halls.

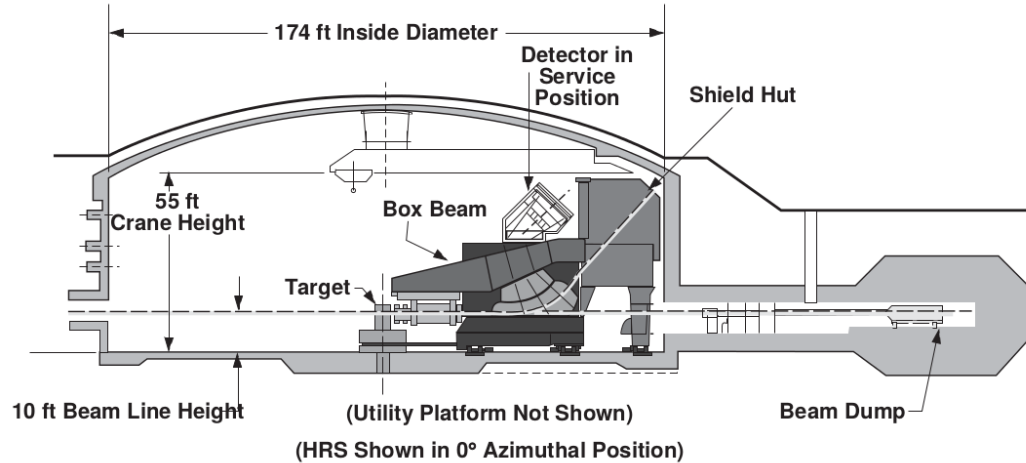


Figure 2.3: Schematic cross section of Hall A with one of the HRS spectrometers in the (fictitious)  $0^\circ$  position. Figure is taken from [84].

## 2.4 Experimental Hall A

### 2.4.1 General

Hall A, operational since May 1997, is the largest experimental hall at CEBAF. The basic layout of Hall A is shown in Fig. 2.3. The central elements are the target scattering chamber, and the two High Resolution Spectrometers (HRS), referred to as LHRS, or left arm, for the left HRS, and RHRS, or right arm, for the right HRS. The HRS enables accurate momentum and angle measurements at high luminosities, and the presence of two HRSs enables coincidence measurements (not used for GEp), or, in our case, an additional detection system for higher statistics and systematic studies.

### 2.4.2 Rasters

Two raster systems, fast and slow (see Fig. 2.1) were used to decrease target damage and polarization loss, and to reduce systematic uncertainties for the polarization measurements by Nuclear Magnetic Resonance (NMR), since the NMR coil was in contact only with the outer layer of the target [89]. The rasters were positioned about 17 meters upstream of the target. Both the fast and slow rasters consist of two dipole magnets. The fast raster magnets used a common triangular waveform with a frequency of 25 kHz, and results in a  $2 \times 2 \text{ mm}^2$  square (Fig. 2.4a). The slow raster applies two 30 Hz sine functions, with a relative phase of  $\pi/2$  between vertical and horizontal axes to obtain a circular pattern with a diameter of about 2 cm (Fig. 2.4b).

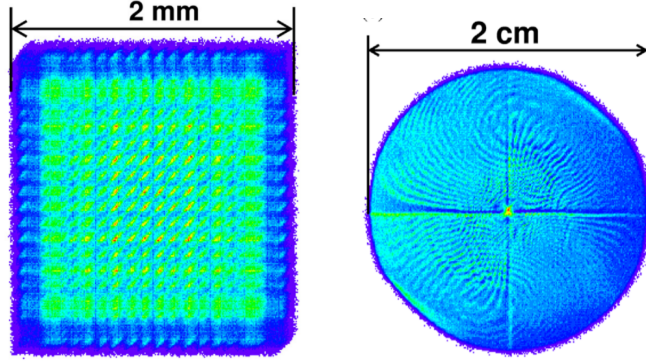


Figure 2.4: Fast (a) and slow (b) raster patterns.

### 2.4.3 Møller Polarimeter

Beam polarization was measured several times during the entire period of the experiment, before, between, and after production runs of GEp, by the Hall A Møller polarimeter [84, 90]. The principle of the Møller polarimeter is to use polarized electron targets and measure the cross section for the  $\bar{e}^+ + e^- \rightarrow e^- + e^-$  process. The cross section for this reaction is given by:

$$\sigma \propto \left[ 1 + \sum_{i=x,y,z} (A_{ii} \cdot P_{t,i} \cdot P_{b,i}) \right] \quad (2.1)$$

where  $i$  is the projection of the polarizations on the Cartesian axis,  $A$  is the analyzing power, which is a function of the scattering angle in the center-of-mass frame,  $\theta_{CM}$ , and  $P_b, P_t$  are beam and target polarizations, respectively. Assuming that the beam direction is along the  $z$ -axis and the scattering happens in the  $zx$  plane, the analyzing power is:

$$\begin{aligned} A_{xx} &= -\frac{\sin^4 \theta_{CM}}{(3 + \cos^2 \theta_{CM})^2}, \\ A_{yy} &= -A_{xx}, \\ A_{zz} &= -\frac{\sin^2 \theta_{CM} (7 + \cos^2 \theta_{CM})}{(3 + \cos^2 \theta_{CM})^2} \end{aligned} \quad (2.2)$$

Analyzing power peaks at  $\theta_{CM} = 90^\circ$ , with a ratio of 7 between the longitudinal and transverse components. Since we are only interested in the longitudinal component of the polarization, measurements were taken at  $\pm 20^\circ$  and averaged to cancel the transverse asymmetries which have opposite signs for these angles.

The polarized electron target is composed of a ferromagnetic foil, magnetized in a magnetic field of about 24 mT along its plane, and the detection is performed by a QQQD magnetic spectrometer (see Fig. 2.5). More details about the Møller polarimeter can be

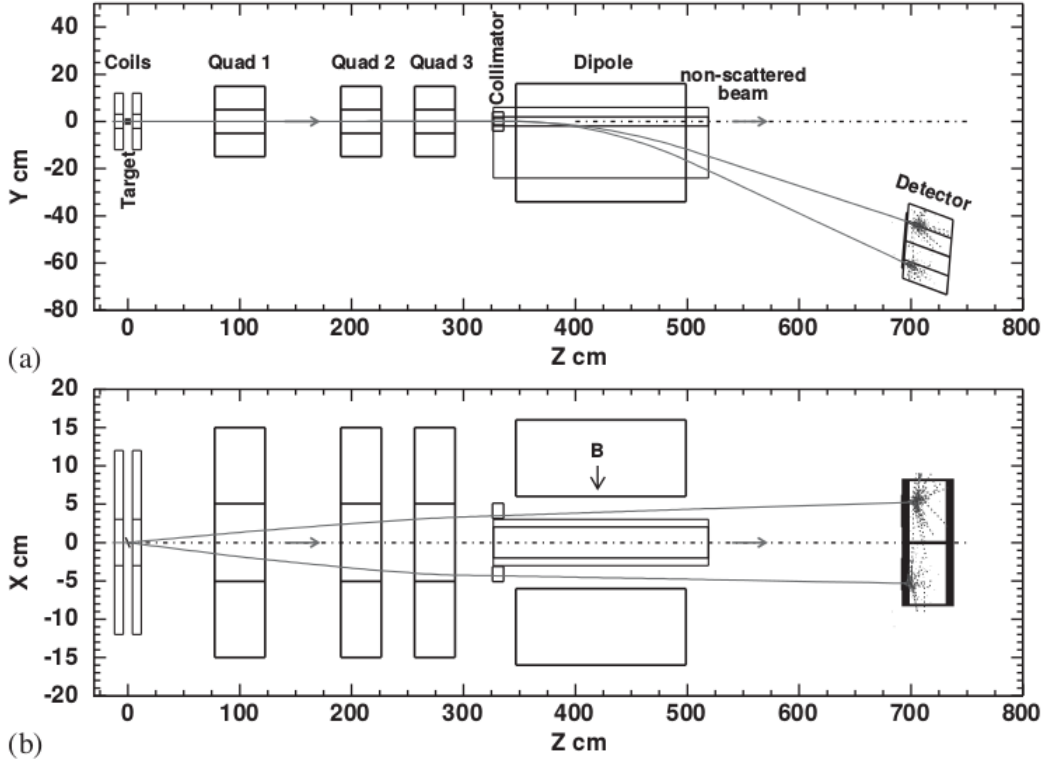


Figure 2.5: Layout of the Møller polarimeter, (a) presents a side view, while (b) presents a top view. The trajectories displayed belong to a simulated event of Møller scattering at  $\theta_{CM} = 80^\circ$  and  $\phi_{CM} = 0^\circ$ , at a beam energy of 4 GeV. Figure taken from [84].

found in [84], and details about the measurement for the GEp experiment can be found in [91]. The relevant results for the GEp experiment are summarized in Table 2.2.

#### 2.4.4 Chicane Magnets

The target is polarized by a 5T magnetic field, at  $5.6^\circ$  towards the x-axis (horizontally) in HCS (see Sec. 3.2.1 for coordinate system definitions). The transverse component of the field causes downwards deflection of the beam. To compensate for this effect, two chicane magnets were installed 5.92 m and 2.66 m upstream of the target (Fig. 2.6). The two dipole magnets were tuned, based on simulations, to direct the beam - after deflection - towards the target as close as possible to the center of the target at horizontal orientation. See also Sec. 3.2.3 for the resulting tilt angle correction that was needed.

date	beam polarization
03/03/2012	$-79.91 \pm 0.20$
03/30/2012	$-80.43 \pm 0.46$
03/30/2012	$+79.89 \pm 0.58$
04/10/2012	$-88.52 \pm 0.30$
04/23/2012	$+89.72 \pm 0.29$
05/04/2012	$-83.47 \pm 0.57$
05/04/2012	$-81.82 \pm 0.59$
05/04/2012	$+80.40 \pm 0.45$
05/15/2012	$+83.59 \pm 0.31$

Table 2.2: Beam polarization as measured by Møller polarimetry. Quoted uncertainties are statistical. Systematic uncertainties are estimated to be 1.7% for all measurements. For details see [91].

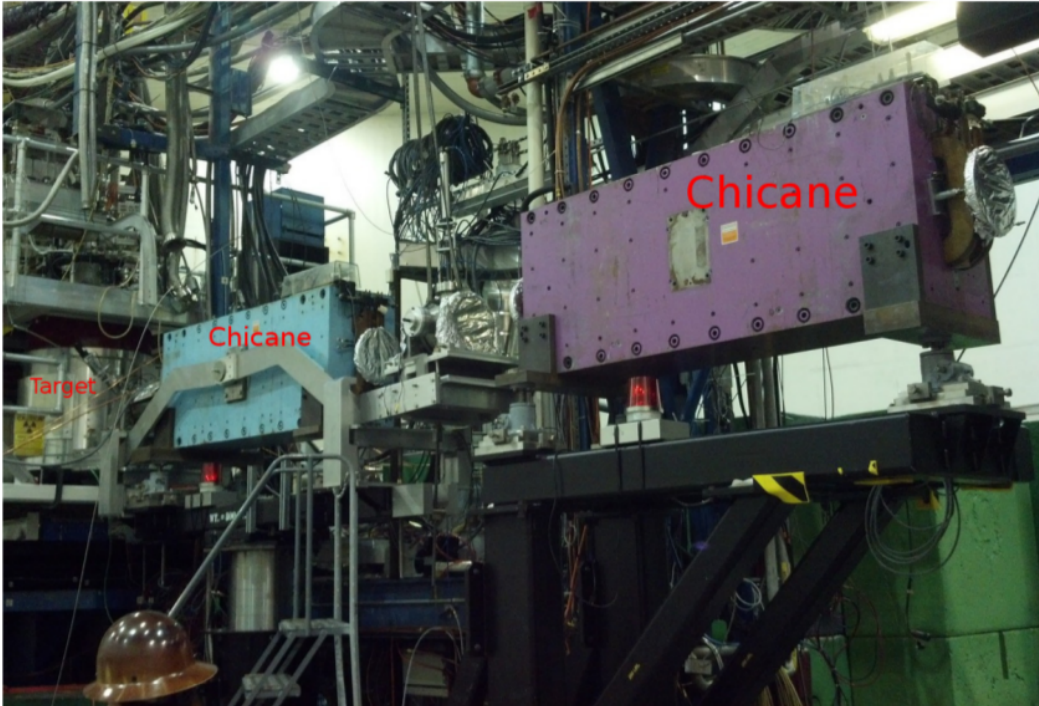


Figure 2.6: The two chicane magnets. Scattering chamber (“target”) is seen at the left of the image.

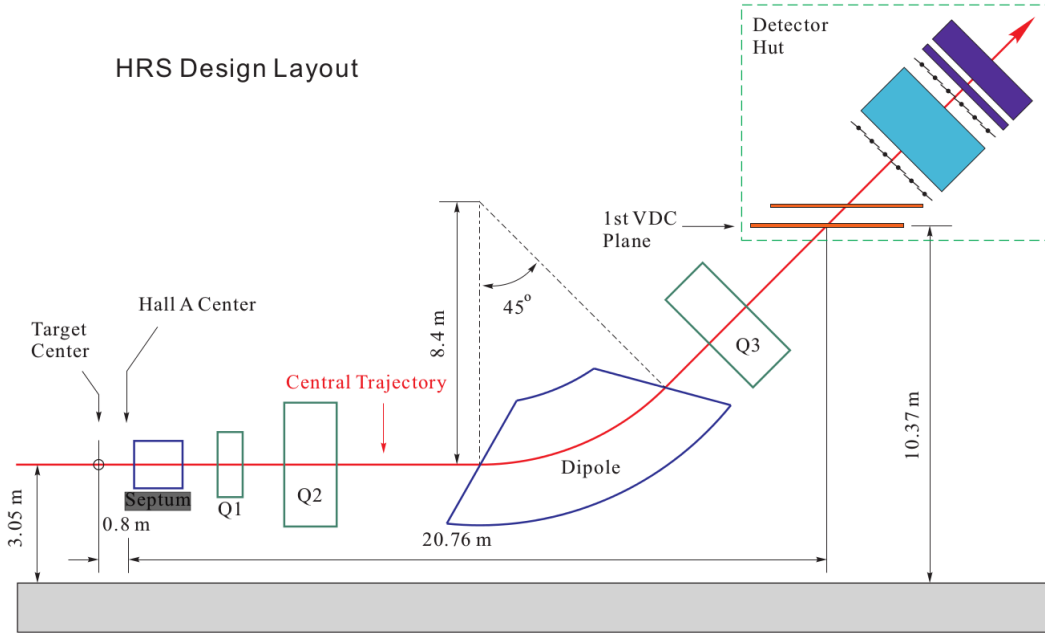


Figure 2.7: Layout of HRS magnets and detector package.

## 2.4.5 High Resolution Spectrometers

The data of the GEp experiment were taken using the standard Hall A HRS spectrometers [84]. Both spectrometers were in use, to increase statistics and for the study of systematic uncertainties. The spectrometers were positioned at their minimum possible angle,  $12.5^\circ$ , and septum magnets were used to achieve the required angles for the experiment (see Sec. 2.6). Here we describe the main characteristics of the HRSs. For a detailed description see [84].

### HRS Magnet System

The spectrometer is composed of a QQDQ arrangement. A schematic view of the HRS is shown in Fig. 2.7, and the main characteristics are given in Table 2.3. First, two superconducting  $\cos 2\theta$  quadrupoles are focus the beam in the vertical and transverse directions, the dipole magnet is used for bending the beam and mapping the momenta dispersion to position distribution, and the last quadrupole focuses in the transverse direction. The HRS has a vertical bend angle of  $45^\circ$ , followed by the HRS detector package.

Fig. 2.8 shows the detector package, which consists of several detection elements, providing information on particle trajectories, particle identification, and for triggering. A detailed description of all detection elements can be found in [84]. Here we focus on the relevant elements for this experiment. Electron momenta and trajectories were extracted using two

Configuration	QQD <sub>n</sub> Q vertical bend
Bending angle	45°
Optical length	23.4 m
Momentum range	0.3-4.0 GeV/c
Momentum acceptance	±4.5% ( $\delta p/p$ )
Momentum resolution	$1 \times 10^{-4}$
Dispersion at the focus (D)	12.4 m
Radial linear magnification (M)	-2.5
D/M	5.0
Horizontal angular acceptance	±30 mrad
Vertical angular acceptance	±60 mrad
Horizontal resolution	1.5 mrad
Vertical resolution	4.0 mrad
Solid angle at $\delta p/p = 0, y_0 = 0$	6 msr
Transverse length acceptance	± 5 cm
Transverse position resolution	1 mm

Table 2.3: Main design characteristics of the Hall A high resolution spectrometers; the resolution values are for the FWHM. Table from [84].

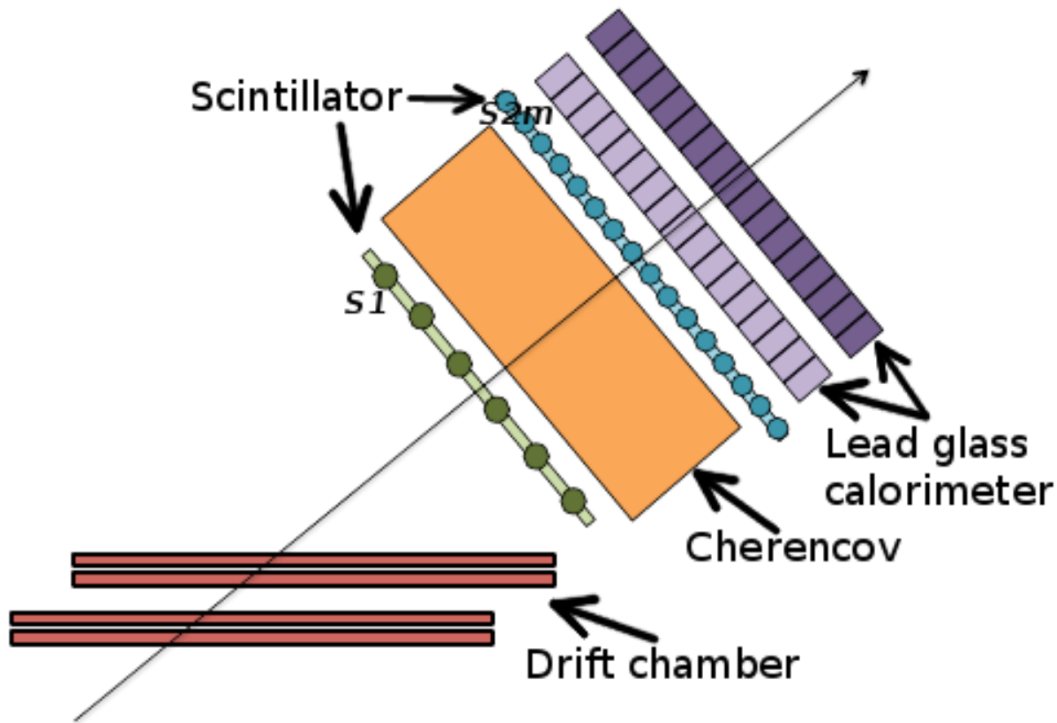


Figure 2.8: Layout of the detector package. The arrow illustrates particle trajectory.

Vertical Drift Chamber (VDC) detectors, and triggering was achieved by two scintillator planes (S1 and S2), separated by a distance of about 2 m. Due to the small scattering angle and energy transfer kinematics of the GEp experiment, particle identification was practically not needed, as  $\pi^-$  could not be emitted into the solid angle of the elastic peak with the proper momentum values (see Sec. 3.3.1).

### Vertical Drift Chamber

Each HRS detection package has a pair of VDC detectors (see Fig. 2.9). They are separated by about 335 mm, and aligned in a standard UV configuration, with their wires oriented at  $90^\circ$  to one another. The VDCs lie horizontally, and nominal particle trajectory is  $45^\circ$  to the VDC plane. There are a total of 368 sense wires in each plane, spaced 4.24 mm apart. The VDC is filled with a gas mixture of argon (62%) and ethane (38%), and the wires are grounded. An electric field is applied by gold plated Mylar planes, nominally at  $-4$  kV. Fig. 2.10 illustrates the detection process. When a charged particle passes through the VDC, it ionizes the gas along its trajectory, and the ionized electrons drift towards the wires along the geodesic path, which is the path of minimum drift time to the wires. Drift time information, collected by TDCs with a common stop signal, allows the reconstruction of the particle trajectory inside the chamber. In the focal plane, a position resolution of 100

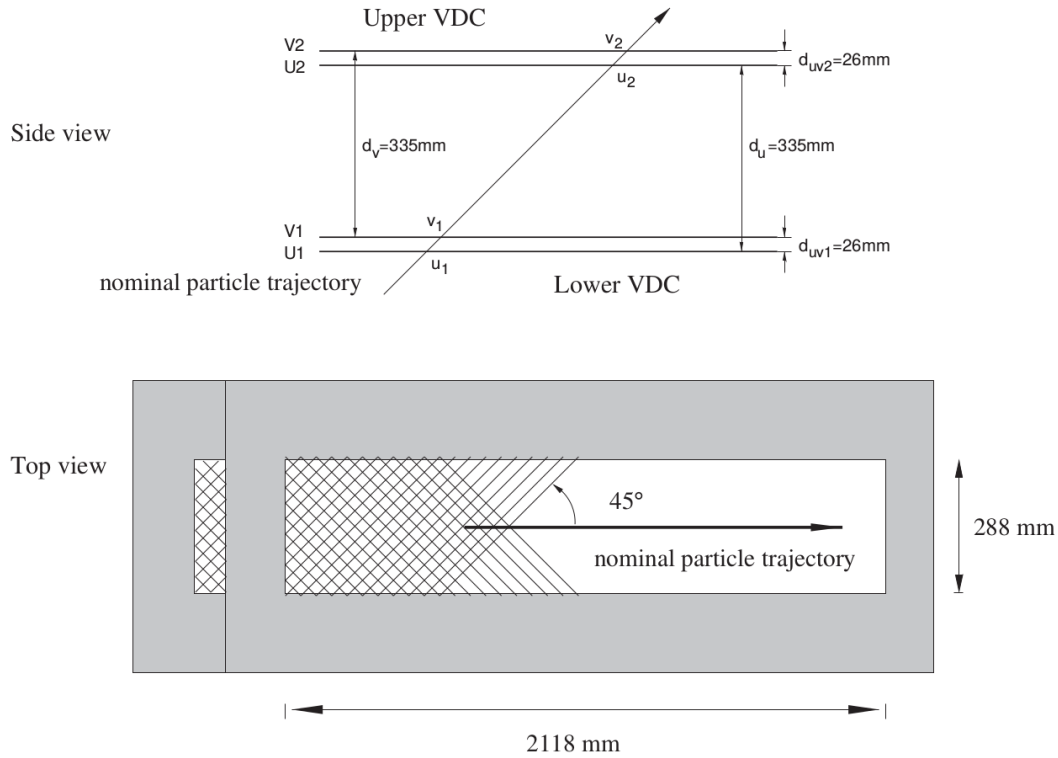


Figure 2.9: Layout of a VDC pair for one HRS (not to scale). The active area of each wire plane is rectangular and has a size of 2118 mm  $\times$  288 mm. Each VDC consists of one U and one V wire plane. The sense wires in each of them are orthogonal to each other and lie in the laboratory horizontal plane. They are inclined at an angle of 45° with respect to both the dispersive and the non-dispersive directions. The vertical distance between like wire planes is 335 mm. Figure from [84].

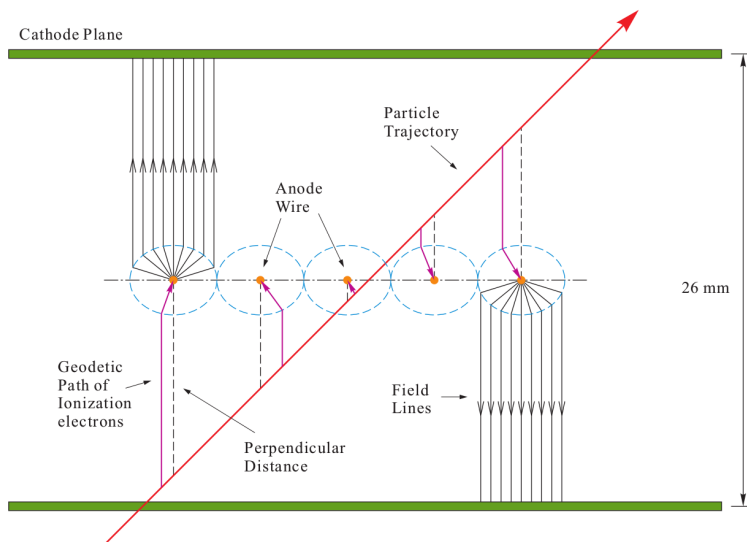


Figure 2.10: Particle detection in VDC. The charged particle ionizes the gas within the drift chamber, and the drift electrons are detected by the wires. Drift time information is used to reconstruct the trajectory within the VDC.

$\mu\text{m}$  and an angular resolution of 0.5 mrad is obtained.

### Scintillator Triggering Planes

Two scintillator planes, S1 and S2, were used for triggering (see Fig. 2.8), each plane consists of a set of plastic scintillators (5 mm BC408). S1 has 6 paddles in a  $1 \times 6$  configuration, and S2 has 16 in a  $1 \times 16$  configuration. The active area for the scintillators is  $0.5 \times 29.5 \times 35.5 \text{ cm}^3$  for S1 and  $0.5 \times 37.0 \times 54.0 \text{ cm}^3$  for S2. Each scintillator had 2 PMTs readouts, and the plane provide time resolution detection of 0.3 ns. Each scintillator could be turned on and off independently, and this feature was use in parts of the experiment to overcome DAQ rate limitations by dismissing irrelevant data on the focal plane. Fig. 2.11 shows the layout of a scintillators plane.

## 2.5 Polarized Target

A highly polarized proton target was needed for the GEp experiment. For this, we used the UVa solid  $\text{NH}_3$  target [92, 93], that was successfully used for several experiments at JLab [94]. The target operates at a temperature of 1 K, with a 5 T magnetic field, and the high polarization level is achieved by the Dynamic Nuclear Polarization (DNP) technique.

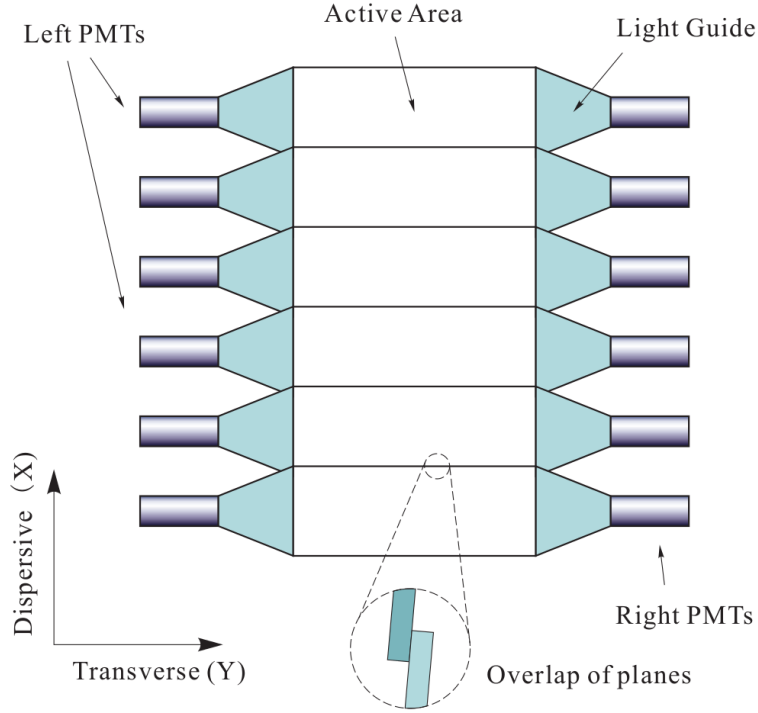


Figure 2.11: Layout of scintillators plane.

### 2.5.1 Dynamic Nuclear Polarization

Target polarization level is defined by the difference between positive and negative aligned nuclear spins relative to the polarization axis, divided by the total number of nuclear spins:

$$P = \frac{N_{\uparrow} - N_{\downarrow}}{N_{\uparrow} + N_{\downarrow}}. \quad (2.3)$$

A thermal equilibrium (TE) polarization is the case when a target is cooled to low temperatures, and placed in a high magnetic field. In that case, the population of two magnetic sub levels is determined by the Boltzmann distribution:

$$N_1 = N_2 \cdot \exp\left(\frac{-\Delta E}{k_B T}\right), \quad (2.4)$$

where  $T$  is the temperature of the target,  $k_B$  is the Boltzmann constant, and  $N_{1,2}$  are the number of nuclear spins in each sub level. For a spin-1/2 target, the polarization level obtained by TE is:

$$P = \tanh\left(\frac{g\mu B}{2k_B T}\right). \quad (2.5)$$

Here  $g$  and  $\mu$  are the particle g-factor and magnetic moments, respectively. Although for electrons TE polarization can reach above 90% polarization in practical conditions, the low

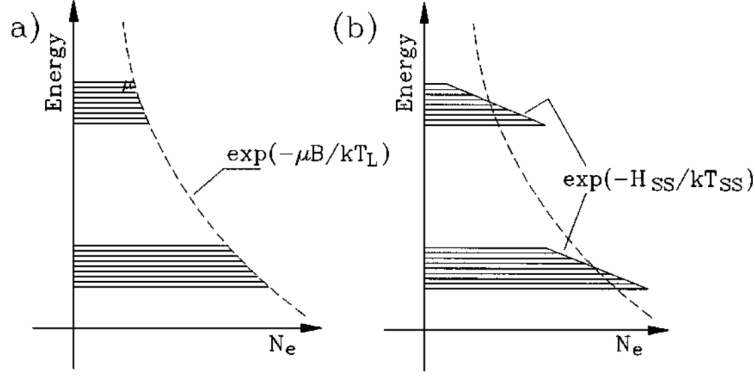


Figure 2.12: Population densities of the electron levels  $N_e$  at different temperatures of the spin-spin interaction reservoir  $T_{SS}$  and electron Zeeman reservoir  $T_{Ze}$ . (a) Spin-spin interaction reservoir and Zeeman reservoir in thermal equilibrium with the lattice:  $T_{SS} = T_{Ze} = T_L$ , (b)  $0 < T_{SS} < T_{Ze}$ . Figure from [95]

value of the proton magnetic moment,  $\mu_p$ , causes much lower polarization levels. For example, at temperature of 0.5 K and magnetic field of 5 T, the TE polarization of protons is about 0.01, whereas electron polarization is almost unity [95].

The DNP technique is a way to significantly increase nuclear polarization levels by applying microwave radiation on the target. In the UVa target, the relevant effect for the increase in polarization is described by the equal spin temperature theory (EST). The spin temperature model is needed since in solid  $\text{NH}_3$  target the electron density is high and spin-spin interaction (SSI) plays an important role in the description of the system. Fig. 2.12 illustrates the electron energy level schemes without (a) and with (b) microwave radiation. In the TE situation, there is the Zeeman splitting between the main two energy levels, while each of the Zeeman level contains a quasi-continuous band of spin-spin (SS) states. The entire level occupation distribution follows a Boltzmann distribution with a lattice temperature  $T_L$ . The EST theory describes the state occupation within each band, and the occupation of the different bands, using Boltzmann distributions with different temperatures denoted  $T_{SS}$  for the SSI reservoir and  $T_{Ze}$  for the electron Zeeman reservoir. Similarly, the nuclear Zeeman reservoir has its own temperature  $T_{Zn}$ . In the TE case, all temperatures are the same. However, while applying microwave radiation, different temperatures might be driven by changing the occupations of the different levels using the proper frequencies (Fig. 2.12b). In the DNP process, we apply microwave radiation with frequency of  $(\nu_e - \Delta)$ , where  $h\nu_e$  is the electron Zeeman energy gap, and  $-h\Delta$  is an additional small amount of energy observed by the electron SSI reservoir. If  $\Delta$  is positive, the SSI reservoir must emit energy and cool down. Finally, the microwave radiation generates thermal mixing between the SSI reservoir

and nuclear Zeeman reservoir. For this, a forbidden transition is driven with a frequency of  $\nu_n$ , corresponding to the nuclear Zeeman energy gap. This transition can be achieved only if  $\Delta \approx \nu_n$  falls into the range of the characteristic frequency of the SSI reservoir. As a result,  $T_{SS}$  and  $T_{Zn}$  are equalized. After this procedure, the polarization level will be determined by

$$P = \tanh\left(\frac{g\mu B}{2k_B T_{SS}}\right), \quad (2.6)$$

which in real condition can reach above 90%.

### 2.5.2 Target Material

The solid  $\text{NH}_3$  was prepared as  $\approx 2$  mm-diameter solid beads. The beads were prepared by the University of Virginia polarized target lab, by condensing ammonia gas and sealing it in a stainless steel tube coated with Teflon. The whole assembly is cooled in a liquid nitrogen bath. After the ammonia freezes, the solid is forced through a mesh to form the beads. The ammonia beads are then transferred to the Medical Industrial Radiation Facility (MIRF) at the National Institute of Standards and Technology (NIST) in Gaithersburg, MD, and irradiated by 14 MeV electron beam at  $\approx 10\mu\text{A}$  to reach the total dose of  $10^{17} \text{ e}^-/\text{cm}^2$ . This process introduces  $\text{NH}_2$  paramagnetic radicals to improve target polarization [92, 93, 96].

### 2.5.3 Target Assembly

The standard UVa polarized target was used for this experiment. Fig. 2.13 shows the general setup of the target. The main components of the target are the superconducting 5T magnet, the evaporation refrigerator, the microwave, the NMR readout system and the target insert.

#### Target Magnet

The original magnet of the target was replaced prior to the experiment due to technical problems. A replacement superconducting magnet from the Hall B polarized target was used. The magnet is designed with an open geometry, in order to allow the beam to pass through the target to the HRSs in various magnetic field configurations. There are some differences between the original magnet and the replacement magnet, with the most relevant difference being the smaller volume of the uniform magnetic field, a cylindrical volume 20 mm in diameter and 20 mm long, that does not cover the full volume of the  $\text{NH}_3$  target. However, we saw no adverse effect on the proton polarization. For further details about these differences see [97].

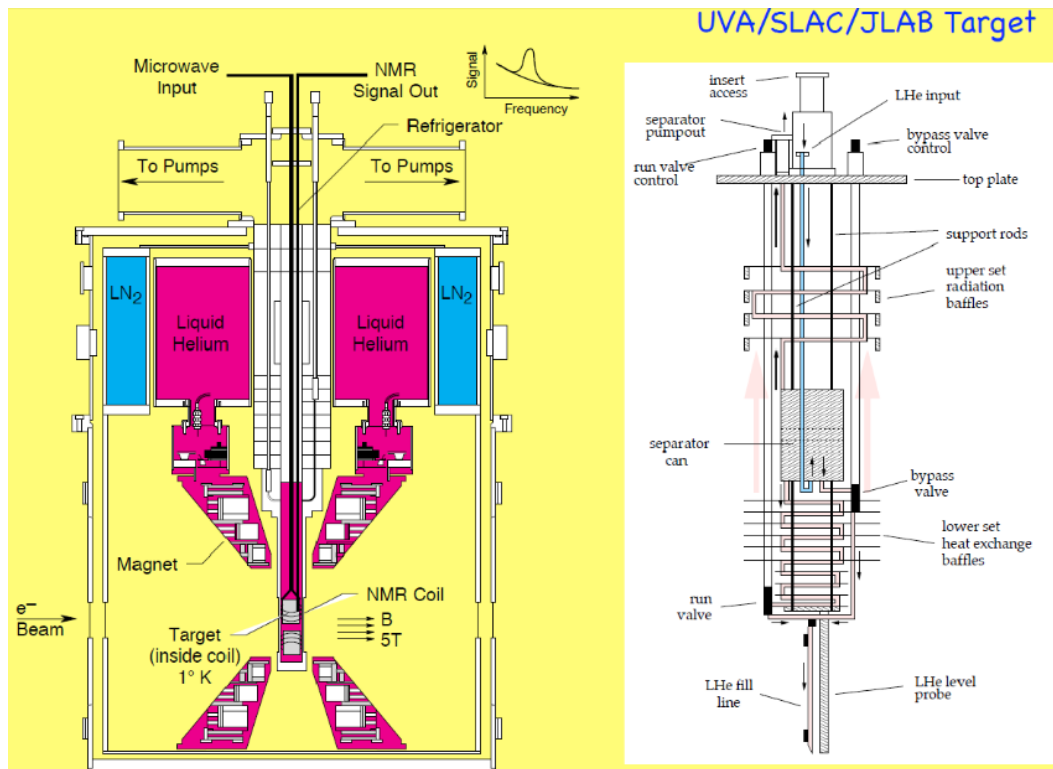


Figure 2.13: Target assembly.

## Evaporation Refrigerator

The original refrigerator of the target was damaged in a previous experiment, hence, a new  $^4\text{He}$  refrigerator was used for this experiment. The design of the refrigerator is shown in Fig. 2.14. The refrigerator is fed with liquid helium from the magnet dewar by an insulated transfer line onto the top of a stainless steel separator, where it drains through a 1 mm thick plate of stainless steel to remove vapor transferred with the liquid [97]. The liquid below the separator is delivered to the target nose, where the vapor is pumped away to reach a temperature of  $\sim 1$  K. For further details see [93, 97].

## The Microwave

The microwaves were generated by Extended Interaction Oscillator (EIO) tube. For a 5T magnetic field, microwaves at 140 GHz are needed. The tube has a tunable range of 1%, that was needed for flipping spin direction. The tube was mounted on top of the target lifter and move with the insert, and a circular waveguide was used to deliver the microwaves to the target insert. Microwave power of 1 W was delivered to the target cells.

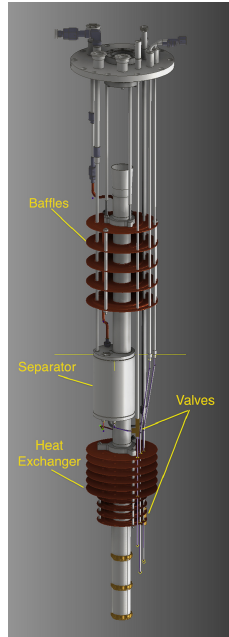


Figure 2.14: The evaporation refrigerator.

## NMR

An NMR system was used for continuous measurement of the polarization level in the target. The NMR system used in this experiment is the same as the one used in previous experiments with this target. The signal from the NMR coil was connected to a Q-meter circuit to measure the polarization of the target [98]. A scheme of the NMR circuit is shown in Fig. 2.19. The circuit inductor is a short coil of CuNi capillary installed inside the target cells.

The polarization level depends on the magnetic susceptibility:

$$P = K \int_0^{\infty} \chi''(\omega) d\omega, \quad (2.7)$$

where K is a constant, and the susceptibility:

$$\chi = \chi'(\omega) - i\chi''(\omega). \quad (2.8)$$

The NMR coil inductance is affected by the susceptibility:

$$L(\omega) = L_0 (1 + 4\pi\chi(\omega)), \quad (2.9)$$

where  $\eta$  is the effective filling factor of the coil. For protons, the susceptibility is zero for all frequencies except for a small band close to the proton resonance  $\omega_0$ , and the integral is evaluated only in this range, causing a peak in the output of the circuit. Changes in proton polarization, hence changes in  $\chi''$ , cause a change in the Q value of this resonant system and allows the evaluation of the polarization through the area of the NMR peak.

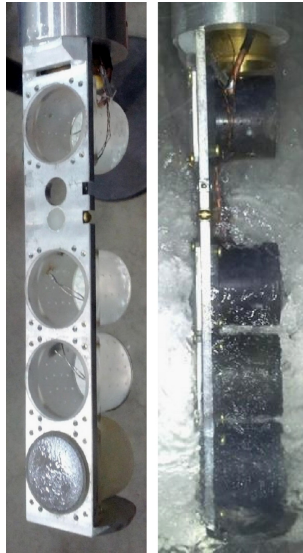


Figure 2.15: The target cells. On the left the cells are shown empty in air. On the right, the cells are full and submerged in liquid nitrogen. The top two cells seen contained the  $\text{NH}_3$  target material. The microwave horn can be seen at the top of the image. Figure from [97].

### Target Insert

The target insert consisted of a long, 1.65 inch diameter carbon fiber tube with an aluminum ladder piece attached to the end. The ladder contains two cells for production  $\text{NH}_3$  targets, the other cells are for carbon and dummy targets, used for optics purposes. The ladder is shown in Fig. 2.15.

## 2.6 Septum Magnets

The data were taken at forward angles of  $\sim 4^\circ - 7^\circ$ . Due to technical limitations, the HRSs could not be placed at angles below  $12.5^\circ$ . For this reason, the target was placed 88 cm upstream of the traditional Hall A center, and two septum magnets were installed in front of the spectrometer to redirect the scattered electrons from the forward angles to the actual HRSs position. During the experiment, between production of 2.2 GeV to 1.7 GeV configurations, a series of technical failures in the right septum occurred, and caused some additional complexity for the optics of the right arm data. A schematic diagram of the septum magnet is shown in Fig. 2.16.

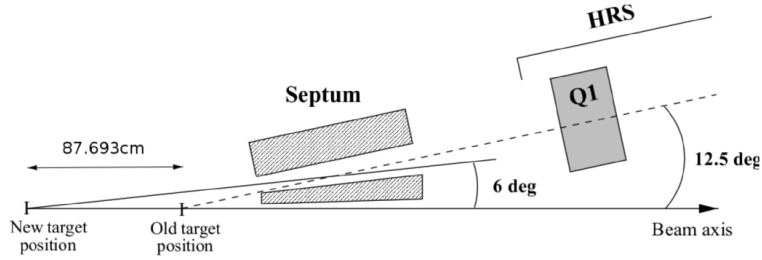


Figure 2.16: A schematic drawing of the septum magnet.

## 2.7 Data Acquisition

The standard Hall A DAQ for left and right HRSs were used for the experiment (Fig. 2.17). As a trigger, a logical AND between the S1 and S2 scintillator planes was used (see Sec. 2.4.5). Trigger efficiency was not determined for the purpose of asymmetry extraction, but was estimated to be above 99% based on Cherenkov analysis by the E08-027 experiment [85, 86]. The scalers has two modes. The SIS3800 is a counter where each trigger is counted once for the charge, trigger and clock signals, and the SIS3801 is a ring buffer triggered by helicity to save and clean the buffer, and was used to save the helicity dependent signals stored in the SIS3800.

Beam helicity was set by a helicity control board. The orientation of the laser polarization is controlled by the level of the high voltage supply, which in turn determines the helicity sign. The helicity is produced pseudo-randomly in either  $-++-$  or  $+--+$  patterns. The helicity control board sends four signals to the experimental hall with the helicity information (Fig. 2.18): T-Settle signal is used for triggering and helicity reliability, Pair Sync and Pattern Sync contain information on pair ( $-+ / +-$ ) and pattern ( $-++- / +--+$ ) helicities, respectively, for a double check of the helicity extraction. To prevent electronic cross-talk that could feed real-time helicity information to the DAQ system or experimental setup, the helicity signal received by the experimental DAQ is delayed by 8 windows, and the actual helicity of a physics event is predicted with the Delayed Helicity signal off-line by the same pseudo-random algorithm.

Target polarization was measured with a continuous-wave NMR coil and a Q-meter enclosure containing two separate Q-meters and Yale gain cards (Q-meter conditioning card) for the two different target cells (See Fig. 2.19) [95, 98]. A Rohde & Schwartz RF generator (R&S) produced a triangle wave of 1 kHz providing a sweep over frequency. The R&S responded to an external modulation sweeping linearly from 400 kHz below to 400 kHz above the Larmor frequency. The signal from the R&S was connected to the NMR coils within

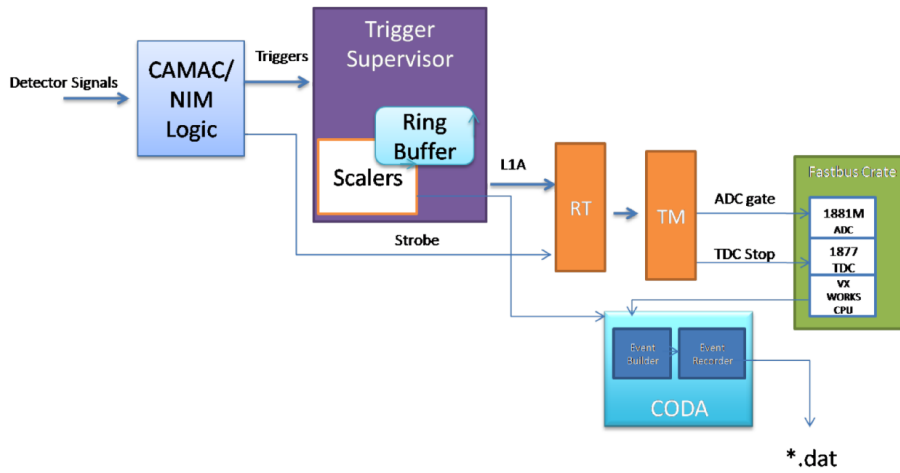


Figure 2.17: Hall A standard DAQ system.

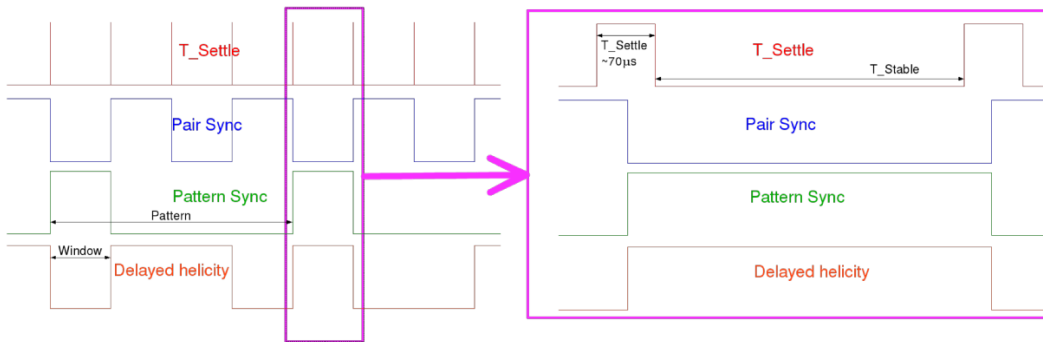


Figure 2.18: Helicity signals.

the target material. This connection was made with a  $\lambda/2$  semi-rigid cable with a Teflon dielectric. The signal from the Q-meter was passed through the Yale gain card before the signal was digitized. It is possible to enhance the signal to noise level by performing multiple frequency sweeps and averaging the signals. A completion of the set number of sweeps resulted in a single target event with a time stamp. The averaged signal was integrated to obtain a NMR polarization area for that event. Each target event contained all NMR system parameters and the target environment variables needed to calculate the final polarization.

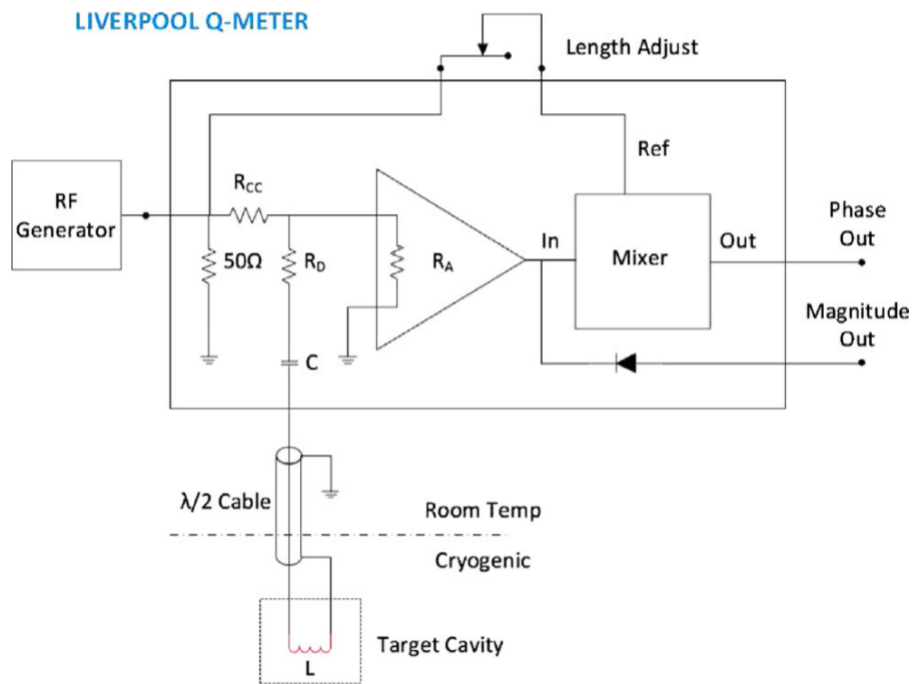


Figure 2.19: Schematic diagram depicting the RF generator, the Q-meter, and the target cavity. Figure from [96].

# Chapter 3

## Data Analysis

### 3.1 Target Polarization

The Q-meter uses the NMR coil as a polarization detector, by coupling inductively with the magnetic moments of the nuclei in the material leading to a linear relation between the coil impedance and the complex magnetic susceptibility of the target material (see Sec. 2.5.3). The NMR signal peaks above the Larmor frequency, while the absorption, which is the imaginary part, describes the spectral distribution of the precession frequencies of the spins near the Larmor frequency. Hence, the integral of the NMR signal around the peak is proportional to the target polarization.

In order to determine a calibration constant for the ratio between the the integrated NMR signal and the target polarization, thermal equilibrium measurements (TE) were used. In this measurement, the target polarization was measured in the presence of the same magnetic field as in the experiment, with the same target material, but without microwave radiation or beam on target. If we denote the area beneath the NMR signal during TE as  $A_{TE}$ , we can extract the calibration constant  $C_{TE}$  by:

$$C_{TE} = \frac{P_{TE}}{A_{TE}}, \quad (3.1)$$

where the thermal polarization level  $P_{TE}$  is calculated by Eq. 2.5. In real conditions, we can extract the actual polarization using the linear relation:

$$P = G \frac{A}{A_{TE}} P_{TE} = GC_{TE}A, \quad (3.2)$$

where  $G$  is the ratio of the gains from the Yale card used during TE and the experiment.

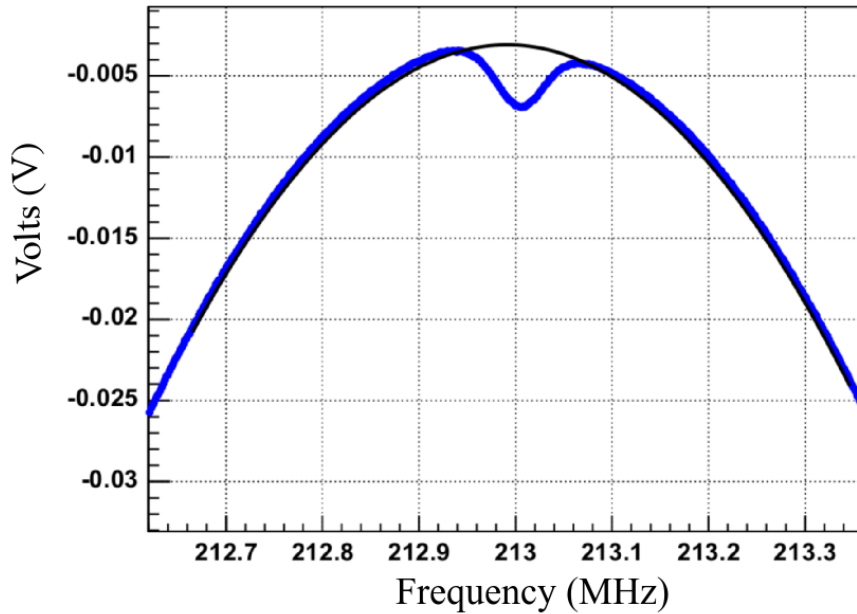


Figure 3.1: An example of raw NMR signal for one of the TE measurements. The black curve is the polynomial fit for the baseline.

### 3.1.1 NMR Signal Fitting and Integration

Fig. 3.1 is an example of the NMR signal for one of the TE measurements. The signal is the dip on top of the non linear baseline. A baseline spectrum was taken by adjusting the magnetic field to be off-resonance. A polynomial fit is used for the baseline, and the fitted baseline is shown in the figure.

Fig. 3.2 is an example of the subtracted signal for a TE measurement and for an enhanced signal during the experiment. The area is calculated using a Riemann sum, and the uncertainty is the combination of the baseline and the Riemann sum. As evident from Fig. 3.2 and Eq. 3.2, the contribution of the enhanced signal area uncertainty to the total uncertainty is negligible. In order to obtain an estimate in the TE Riemann sum, a Gaussian signal of average TE amplitude was generated on a standard baseline and the Riemann sum with background fit was used to obtain an area. The uncertainty from the background fit is calculated as the percent change in area using the various parameterizations of the polynomial during the  $\chi^2$  minimization,

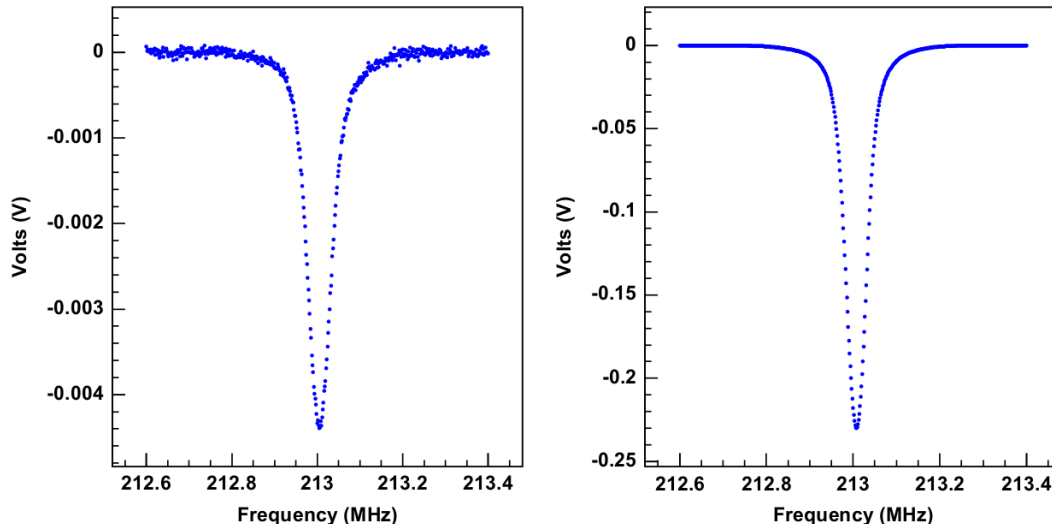


Figure 3.2: The TE (left) and the enhanced signal (right) after baseline and background subtraction.

### 3.1.2 Thermal Equilibrium Polarization

TE measurements were taken with each target material separately. Each TE required a thermalization period of several hours until thermal equilibrium was achieved at 1.5 K. Target temperature was measured using two independent liquid helium vapor pressure sensors connected to a Baratron 690A manometer. The standard accuracy of the manometer is about 0.12% with a  $10^{-6}$  full scale resolution. The temperature is calculated from the pressure according to:

$$T = \sum_{i=0}^9 a_i \left( \frac{\ln p - b}{c} \right)^i, \quad (3.3)$$

where the constants  $a_i$ ,  $b$  and  $c$  are a set of parameters which depend on the state and temperature scale of the helium [99]. There were two He bulbs and manometers. A  $^3\text{He}$  bulb  $\sim 3$  cm above the top cup, and a  $^4\text{He}$  bulb more than 5 cm above the full helium liquid level. The temperature difference maybe due to the distance or calibration variation between the two probes, and this difference, denoted  $\Delta T$ , is treated as the uncertainty on the temperature.

A quality check for each TE measurement was applied to determine whether the TE is usable. During each TE measurement, temperature and NMR signal area were taken many times. The procedure was to search for the set of data with the smallest slope over the largest number of points. The criteria for usability was a requirement of at least six points in area (pressure) spanning the time range in which a fit to a two parameter line gives a slope of less than 0.0035 area/min (Torr/min). In cases that such set of data points was

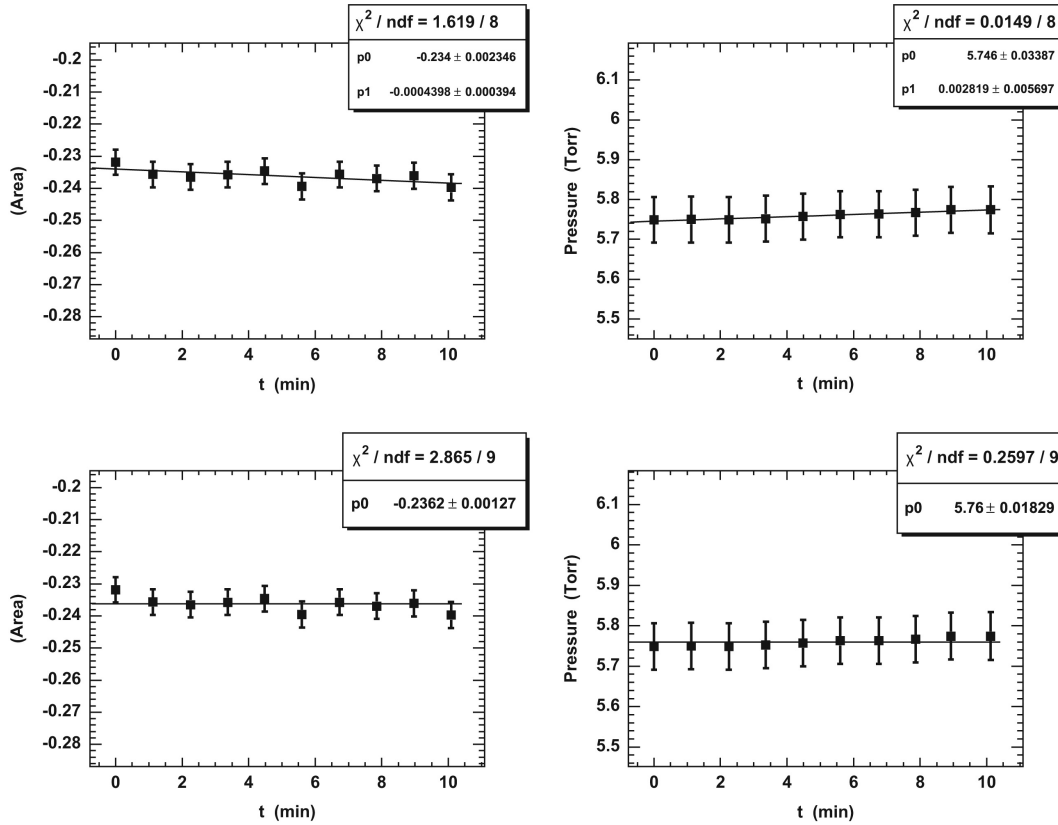


Figure 3.3: Example of fits in area and pressure analysis for TE. The top left (right) shows the two parameter check on the slope of the line for area (pressure). The bottom left (right) shows the final one parameter fit to a one parameter line for area (pressure). The error bars represents the total uncertainties, which are dominated by systematics. Figure from [96].

not found, the TE measurement was classified as unusable. In case that such data set was found, a fit for a constant number applied to obtain the value for the area (pressure). The uncertainties from these fits are used as the uncertainty for area and pressure, and not the individual single point uncertainties. Fig. 3.3 demonstrates this procedure. Table 3.1 shows the calibration constants  $C_{TE}$  that were used for GEp experiment.

For further details about the analysis of target polarization, Yale card and Q-meter characteristics, and quality checks, please refer to [96].

### 3.1.3 Polarization Data

Target polarization was measured regularly during data production, and the data were recorded with time stamps for proper association to HRS data. Polarization was charge-

runs	$E_{beam}$ (GeV)	cup	$C_{TE}$
3061-3070 , 22146-22155	2.2	top	-1.30 (3.05%)
3071-3084 , 22156-22172	2.2	bottom	-1.37 (3.76%)
3085-3130 , 22173-22217	2.2	top	-1.30 (3.05%)
4599-4695 , 23540-23618	1.7	bottom	-1.82 (3.01%)
5339-5344 , 24113-24118	1.1	top	-1.424 (2.87%)
5345-5346 , 24120-24121	1.1	bottom	-1.799 (3.28%)
5347-5484 , 24122-24258	1.1	bottom	-1.731 (3.18%)

Table 3.1: TE calibration constants and their relative uncertainties with the associated experimental production runs.

averaged assuming a linear change in polarization within a single run as function of time:

$$\bar{P}_{run} = \sum_i^n Q_i P_i. \quad (3.4)$$

Although we know that the polarization drops exponentially, we consider this assumption reasonable due to the small variation, in a single run. The error estimate for the charge-averaged polarization is calculated using:

$$\Delta \bar{P}_{run} = \sqrt{\sum_i^n Q_i^2 (\bar{P}_{run} - P_i)^2}. \quad (3.5)$$

Runs with  $\Delta \bar{P}_{run} / \bar{P}_{run} > 0.5\%$  were excluded. Fig. 3.4 shows the final polarization results used in the analysis.

### 3.1.4 Uncertainties

Eq. (3.2) is used for the polarization extraction. The relative uncertainty on the enhanced signal sum is negligible. The relative uncertainty on the TE signal sum is composed from the uncertainty on the Riemann sum,  $\Delta A_{TE} \approx 1.61\%$ , and the uncertainty on the baseline fit  $\Delta A_{fit} \approx 0.75\%$  (see Sec. 3.1.1). The polarization during TE,  $P_{TE}$ , is calculated according Eq. (2.5), and the uncertainty is:

$$\delta P_{TE} = \frac{\mu B}{kT} \sqrt{\left(\frac{\delta B}{B}\right)^2 + \left(\frac{\delta T}{T}\right)^2} \operatorname{sech}^2\left(\frac{\mu B}{kT}\right). \quad (3.6)$$

The uncertainty on the magnetic field originated from an instrumental uncertainty of about 0.01%, and the uncertainty of the field strength through the target material. The total



source	uncertainty (%)
$\Delta T$	1.45
$\Delta A_{TE}$	1.61
$\Delta A_{fit}$	0.75
$\Delta R_B$	0.50
$\Delta V_Q$	0.75
NMR tune	0.47
$\Delta B_{drift}$	0.25
$\Delta V_{Yale}$	0.10
$\Delta \bar{P}_{run}$	0.50
total	2.6

Table 3.2: Summary of polarization uncertainties, not including uncertainties associated with TE quality check described in Sec. 3.1.2. Note that the major contributions for the polarization uncertainty comes from the TE measurements, hence are scaling uncertainties for the whole set of runs associated with the same calibration constant (Table 3.1).

set of runs associated with the same calibration constant (Table 3.1). Due to the statistical behavior of most of the uncertainties related to the calibration constant, a set of several TE measurements would significantly reduce the systematics of the polarization measurements, which in turn will significantly reduce the uncertainties of the final asymmetries (see Table 4.4). Unfortunately, time constrains prevented such additional measurements.

## 3.2 Optics

The objective of the optics analysis is to obtain physical variables of the scattering process in the target from the measured quantities at the detector package. The standard optics study procedure for HRS was used [100], with modifications to account for the effect of the target and septa magnetic fields. A detailed description of this procedure is found in [101]. For optics studies, a sieve slit was placed before the entrance of the septum magnet. A diagram of the sieve slit is shown in Fig. 3.5.

### 3.2.1 Definition of Coordinate Systems

Several different coordinate systems are used in the optics and physics analysis of the experiment. Here we will define the different coordinate systems that are relevant for this

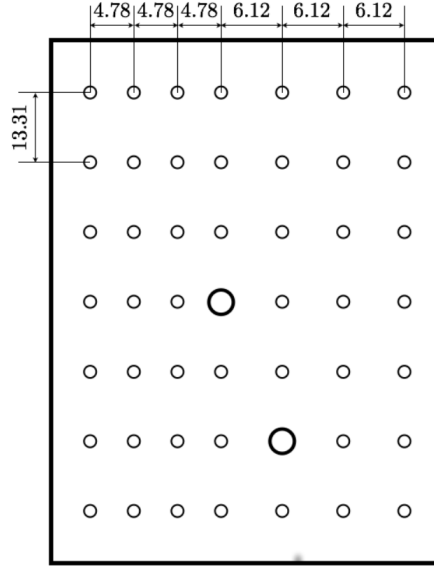


Figure 3.5: Geometric configuration of the sieve slit. Dimensions are in mm. The two large holes are used to determine the orientation of the sieve slit. The diameter is 1.4 mm and 2.7 mm for the normal holes and the large holes respectively. Figure from [101].

report. In general,  $\langle x, y, z \rangle$  coordinates are Cartesian, and spherical coordinates follow the convention:

$$\begin{aligned}
 x &= r \sin \theta \cos \phi, \\
 y &= r \sin \theta \sin \phi, \\
 z &= r \cos \theta.
 \end{aligned}
 \tag{3.8}$$

### Scattering Coordinate System

The scattering coordinate system defines the  $\hat{z}$  direction as the momentum direction of the incoming electron, and the scattering angle  $\theta$  as the angle between the incoming electron and the scattered electron (see Fig. 3.6). If we denote the incoming electron momentum as  $\vec{k}$  and the scattered electron momentum as  $\vec{k}'$ , the scattering coordinate system will be defined by:

$$\begin{aligned}
 \hat{z} &= \frac{\vec{k}}{|\vec{k}|}, \\
 \cos \theta &= \frac{\vec{k} \cdot \vec{k}'}{|\vec{k}| \cdot |\vec{k}'|}.
 \end{aligned}
 \tag{3.9}$$

In this analysis, the azimuthal angle  $\phi$  is arbitrary and has no use.

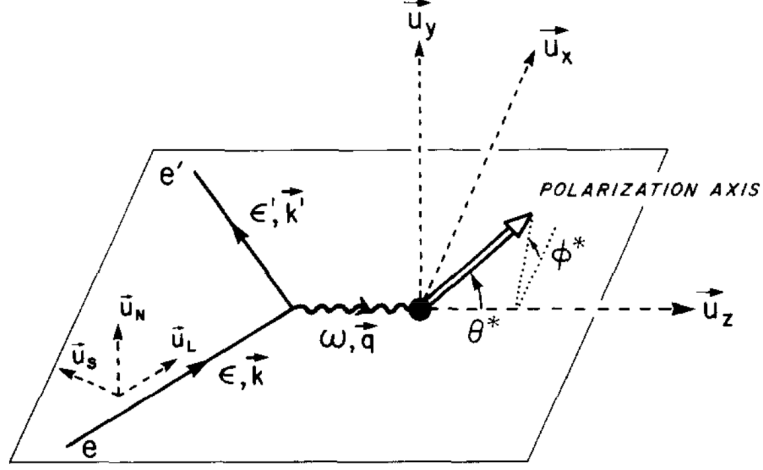


Figure 3.6: Coordinate systems for the scattering of polarized electrons from polarized target. In this figure, the unit vectors  $\vec{u}_S, \vec{u}_N, \vec{u}_L$  define the scattering coordinate system, while  $\vec{u}_x, \vec{u}_y, \vec{u}_z$  define the starred coordinate system. Figure from [16].

### Starred Coordinate System

The starred coordinate system is used for the asymmetry calculation, and defined by the virtual photon momentum  $\vec{q} = \vec{k} - \vec{k}'$  and target polarization axis  $\vec{S}$  (see Fig. 3.6). We denote normal to the scattering plane:

$$\vec{n}_1 = \vec{q} \times \vec{k}, \quad (3.10)$$

and normal to the plane containing the virtual photon momentum and target polarization:

$$\vec{n}_2 = \vec{q} \times \vec{S}. \quad (3.11)$$

The starred angles will be defined as:

$$\begin{aligned} \theta^* &= \arccos \left( \frac{\vec{q} \cdot \vec{S}}{|\vec{q}| \cdot |\vec{S}|} \right), \\ \phi^* &= \arccos \left( \frac{\vec{n}_1 \cdot \vec{n}_2}{|\vec{n}_1| \cdot |\vec{n}_2|} \right). \end{aligned} \quad (3.12)$$

For asymmetry calculation, the azimuthal angle  $\phi^*$  must be taken into account.

### Hall Coordinate System (HCS)

The Hall A coordinate system, HCS, is the Cartesian coordinate system of the experimental hall. The origin of the HCS is at the center of the Hall A, which is defined to be the intersection point of the beam and the vertical axis of the target.  $\hat{z}$  is along the beam line

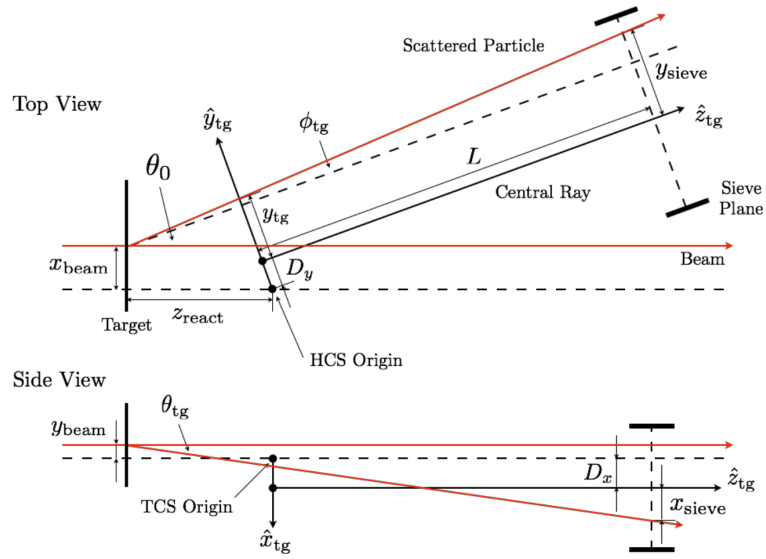


Figure 3.7: Target coordinate system (top and side views).  $\theta_0$  is the spectrometer central angle in HCS,  $L$  is the distance from the sieve slit to the TCS origin,  $D_x$  and  $D_y$  are the vertical and horizontal deviations of the spectrometer central ray to the HCS origin. Figure from [101].

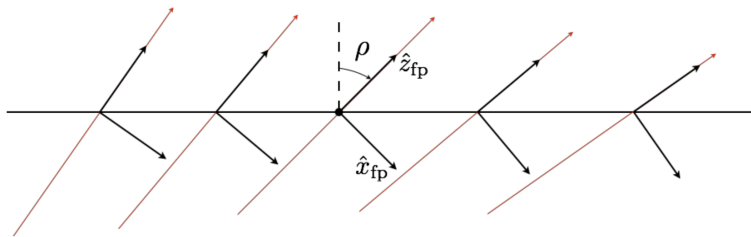


Figure 3.8: Focal plane coordinate system. The red trajectories represents trajectories with  $\theta_{tg} = \phi_{tg} = 0$ . Figure from [101].

and points downstream and  $\hat{y}$  is vertically up. Thus  $\hat{x}$  is to the left if looking along  $\hat{z}$ . This orientation is also used while referring to “left” and “right” HRSs.

### Target Coordinate System (TCS)

The  $\hat{z}$  axis of the TCS, also noted as  $z_{tg}$  angle, is defined by the central ray of the sieve collimator for a given spectrometer which is the line vertically passing through the center point of the central sieve slit hole (see Fig. 3.7). The angle between  $\hat{z}_{tg}$  of the TCS and the  $\hat{z}$  of the HCS is defined as the central angle  $\theta_0$  of the spectrometer. The out-of-plane angle  $\theta_{tg}$  and the in-plane  $\phi_{tg}$  angle with respect to the central ray are given by:

$$\begin{aligned}\tan \theta_{tg} &= \frac{dx}{dz}, \\ \tan \phi_{tg} &= \frac{dy}{dz}.\end{aligned}\tag{3.13}$$

Note that other reports might refer to the tangent of these angles without implicitly mentioning it.

### Detector Coordinate System (DCS)

DCS are the coordinates of the detected particle as measured in the VDCs.  $\hat{z}_{det}$  is perpendicular to the VDC plane pointing vertically up, and  $\hat{x}_{det}$  is parallel to the long symmetry axis of the lower VDC pointing downstream. Thus  $\hat{y}_{det}$  is parallel to the short symmetry axis of the lower VDC. When a particle is detected, two angular coordinates  $\theta_{det}, \phi_{det}$  and two spatial coordinates  $x_{det}, y_{det}$  are calculated in this coordinate system.

### Transport Coordinate System at the focal plane (TRCS)

The TRCS is an intermediate coordinate system that is used to transport the DCS to the focal plane coordinate system. It is done by rotating DCS clockwise by  $\rho = 45^\circ$ . The implicit transformation is given by:

$$\begin{aligned}\theta_{tra} &= \frac{\theta_{det} + \tan \rho_0}{1 - \theta_{det} \tan \rho_0}, \\ \phi_{tra} &= \frac{\phi_{det}}{\cos \rho_0 (1 - \theta_{det} \tan \rho_0)}, \\ x_{tra} &= x_{det} \cos \rho_0 (1 + \theta_{tra} \tan \rho_0), \\ y_{tra} &= y_{det} + \sin \rho_0 \phi_{tra} x_{det}.\end{aligned}\tag{3.14}$$

### Focal Plane Coordinate System (FCS)

The FCS is a rotation of DCS that fixes  $\hat{z}_{fp}$  parallel to trajectories with  $\theta_{tg} = \phi_{tg} = 0$ , and rotating DCS clockwise around its  $\hat{y}$  by the angle  $\rho$  between  $\hat{z}_{fp}$  and  $\hat{z}_{det}$  (see Fig. 3.8). This rotation is calculated by:

$$\begin{aligned}
 x_{fp} &= x_{tra}, \\
 \tan \rho &= \sum C_{i000}^t x_{fp}^i, \\
 y_{fp} &= y_{tra} - \sum C_{i000}^y x_{fp}^i, \\
 \theta_{fp} &= \frac{\theta_{det} + \tan \rho}{1 - \theta_{det} \tan \rho}, \\
 \phi_{fp} &= \frac{\phi_{det} - \sum C_{i000}^p x_{fp}^i}{\cos \rho (1 - \theta_{det} \tan \rho)}.
 \end{aligned} \tag{3.15}$$

Where the coefficients  $C_{i000}^t, C_{i000}^y, C_{i000}^p$  include the corrections due to the systematic offset of the VDCs.

Further details of the different Hall A coordinate systems can be found in [100].

### 3.2.2 Reaction Variables Reconstruction

The standard HRS variables reconstruction procedure described in [100] is able to reconstruct the trajectories in cases where no target field is applied. In our case, a 5T magnetic field around the target adds more complexity to the procedure. For this, optics calibration and analysis is broken into two parts. The trajectories between the target and septa entrance are calculated by simulations of the electron motion in magnetic field. The magnetic field is characterized by applying the Biot-Savart law to the current density distribution, and a cross-check is done by direct measurement of the target field. The uncertainty of the field map is less than 1.2% over the whole region [102]. The reconstruction of the trajectories from focal plane to the entrance of the septa is done using the optics matrix. The optics matrix is a matrix that correlates focal plane variables with TCS variables  $\theta_{tg}, y_{tg}, \phi_{tg}$  and the delta momentum variable defined as:

$$\delta = \frac{P - P_0}{P_0}, \tag{3.16}$$

where  $P$  is particle momentum and  $P_0$  is HRS central momentum. During the calibration,  $x_{tg}$  is effectively set to zero. The optics matrix, to the first order approximation, can be expressed as:

$$\begin{pmatrix} \delta \\ \theta \\ y \\ \phi \end{pmatrix}_{tg} = \begin{pmatrix} \langle \delta|x \rangle & \langle \delta|\theta \rangle & 0 & 0 \\ \langle \theta|x \rangle & \langle \theta|\theta \rangle & 0 & 0 \\ 0 & 0 & \langle y|y \rangle & \langle y|\phi \rangle \\ 0 & 0 & \langle \phi|y \rangle & \langle \phi|\phi \rangle \end{pmatrix} \begin{pmatrix} x \\ \theta \\ y \\ \phi \end{pmatrix}_{fp} \quad (3.17)$$

In practice, the full matrix is optimized up to third order.

The optimization of the optics matrix is done using the sieve slit, and based on the well known behavior of elastic scattering and on survey data described in [103, 104]. The simulation of the magnetic field is also required for the optics matrix optimization, since linear propagation of the trajectories from the target to the sieve slit cannot be assumed.

### 3.2.3 Tilt Angle

In addition to the bending of the scattered electron, the presence of the target field results in bending the beam prior to the interaction. To compensate for this effect, two chicane magnets were installed to lower then lift beam trajectory in the precise amount to guide the beam as parallel to  $z_{HCS}$  as possible, and at the center of the target. However, even after this correction, the beam had deviations from the center and was slightly tilted relative to  $z_{HCS}$ .

During production runs, beam current was reduced to  $\sim 10$  nA to decrease target polarization degradation. As a result, beam position information could not be extracted. The position information required for the interaction variables reconstruction obtained using BdL simulation, and the results are given using average quantities. Note that this information is used twice: first for the reconstruction of HCS variable, and second for the transformation from HCS to scattering coordinate system, which is where the physics analysis is done.

### 3.2.4 Elastic peak correction

The accuracy of the above procedure can be checked against the elastic scattering formula (see Append. A):

$$E' = \frac{E}{1 + \frac{E}{M}(1 - \cos \theta)}. \quad (3.18)$$

One can see that the decrease in the scattered electron energy depends on  $E/M$ . This results in a separation between different elements on the focal plane. Fig. 3.9a shows an example of the event distribution in TRCS. The separation between the hydrogen and the other heavier elements ( $^{14}\text{N}$  and  $^4\text{He}$ ) is evident even on the focal plane. Fig. 3.9b shows the same picture

after applying the above variable reconstruction procedure. The red curves represent Eq. 3.18 correlations for the different elements. The separation between the hydrogen elastic events and the heavy elements is, in general, consistent with Eq. 3.18. A quantitative check of this consistency can be done by cutting on hydrogen events and then adding a tight cut on the scattering angle  $\theta$  around some fixed angle  $\theta_0$ , and plotting the angular distribution of the inverse relationship:

$$\cos \theta = 1 + M \left( \frac{1}{E} - \frac{1}{E'} \right). \quad (3.19)$$

Ideally, this distribution should be centered around  $\theta_0$ , with some broadening due to the resolution of the experimental assembly (experimental broadening, detection resolution and reconstruction resolution). In practice, as shown in Fig. 3.10, a deviation of the mean from  $\theta_0$  is found for most configurations. It should be mentioned that all these comparisons are done after adding an average value to correct for the energy losses before ( $E_{loss,b}$ ) and after ( $E_{loss,a}$ ) the interaction:

$$\begin{aligned} E &= E_{beam} - E_{loss,b}, \\ E' &= E_{detected} + E_{loss,a}. \end{aligned} \quad (3.20)$$

The energy losses are calculated using g2psim (see Sec. 3.4.2).

In principle, this deviation indicates that the reconstruction procedure suffers from an inaccuracy in the reconstruction of the scattering angle or the momentum - or both. In practice, the reconstruction of the momentum is considered much more reliable, and it is almost not affected by the target and septum fields. On the other hand, the reconstruction of the scattering angle is significantly affected by the modeling of the trajectories in the magnetic fields, before and after the interaction. For these reasons, we applied an additional correction on the scattering angle to account for this deviation, assuming that the momentum reconstruction is reliable and using Eq. 3.19.

A direct reconstruction of the scattering angle, on an event-by-event basis, based on detected momentum and the elastic scattering relations, is not applicable due to the significant smearing of the momentum in the target and along the electron trajectory. Instead, we used the current scattering angle reconstruction as a basis, created histograms of the calculated scattering angle using Eq. 3.19 on tight slices of the reconstructed scattering angle, and created correction functions for each experimental configuration (see Fig. 3.11). These functions were used as a correction on an event-by-event basis for the scattering angle reconstruction.

The uncertainty on the above procedure is estimated to be  $\sim 1$  MeV, based on HRS resolution, electron energy loss approximation, and deviation of the invariant masses of

hydrogen peaks from 0.9383 MeV. This translates into a  $\sim 2$  mrad systematic uncertainty in the scattering angle.

### 3.2.5 The g2p Helicity Decoder

The helicity of the first window of each pattern is determined by a pseudo-random generator in the helicity control board. The generator is a 30 bit shift register, hence can be predicted using any sequence of 30 helicity patterns. The helicity reconstruction is done off-line with a dedicated code package, reported separately in [105]. The helicity decoder has about 93% efficiency, meaning that for 7% of the events the helicity state cannot be reconstructed. These events are not used in the analysis, and the only effect of this inefficiency is a reduction in the statistics.

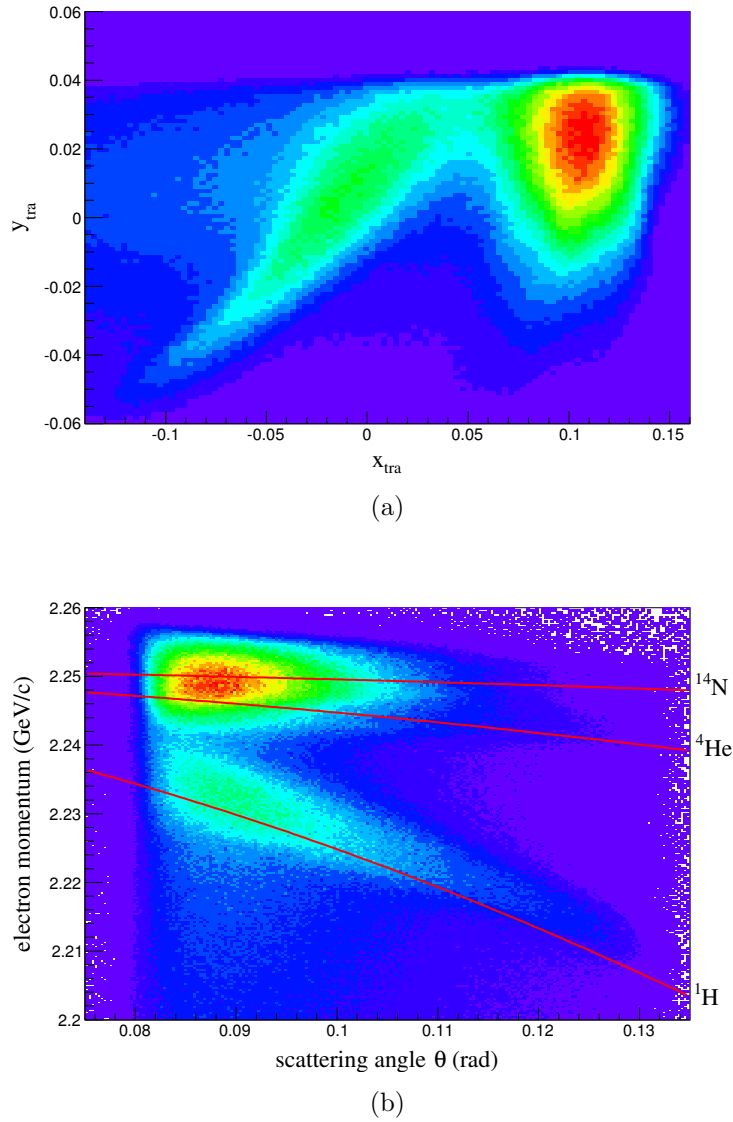


Figure 3.9: Typical focal plane plot in TRCS (a), compared to the reconstructed variables of momentum and scattering angle (b). The separation between elastic scattering on hydrogen and the heavier elements  $^{14}\text{N}$  and  $^4\text{He}$  is evident already on the focal plane, and the red curves compare the reconstructed variables to the elastic stripe formula (Eq. 3.18).

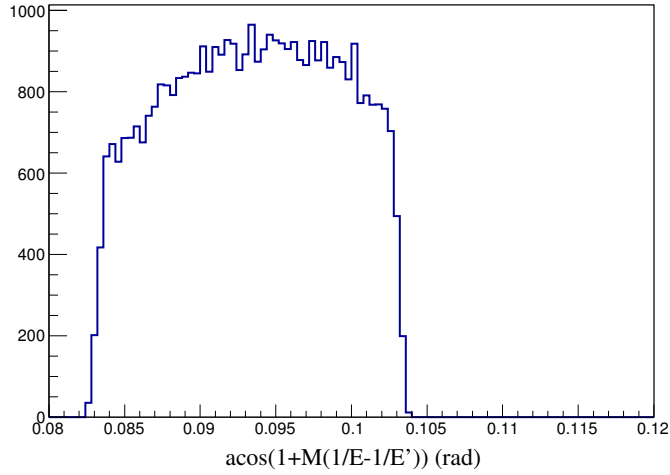


Figure 3.10: Angular distribution of the angles calculated by Eq. 3.19, using the cut  $|\theta - 0.1| < 5 \times 10^{-4}$ , and cutting on hydrogen elastic events. A deviation of the mean from 0.1 indicates an inaccuracy in the reconstruction of the scattering variables.

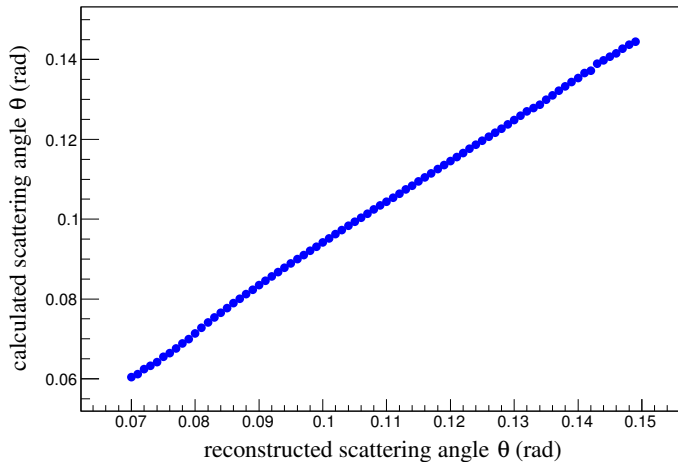


Figure 3.11: Scattering angle correction function for the left arm 2.2 GeV configuration. This function is calculated based on the mean detected momenta and the elastic scattering relation (Eq. 3.19). The function is used as a correction of the scattering angle on an event-by-event basis.

## 3.3 Asymmetries

Physical asymmetries were extracted for the left HRS at all experimental configurations. For the two higher energies, 2.2 and 1.7 GeV, the acceptance was divided into two bins in scattering angle. This was not possible at the 1.1 GeV configuration due to the poor separation between the hydrogen and the heavy-elements at small angles (see Fig. 3.12f). In total, asymmetries for 5  $Q^2$  points were extracted for the left HRS. The optics analysis of the right HRS was slower, and at this point right HRS asymmetries are not available. However, we will present here raw asymmetries for the right HRS. The full process from raw asymmetries to physical asymmetries is described below.

### 3.3.1 Cuts

The main cut used for asymmetry extraction is a cut on the elastic peak in the invariant mass  $W$  (see Fig. 3.12). The invariant mass is calculated, using the target momentum  $P^\mu = (M_p, 0, 0, 0)$  and the momentum transfer  $q^\mu = k^\mu - k'^\mu$ , as:

$$P_{tot}^\mu = q^\mu + P^\mu, \quad (3.21)$$

$$W = \sqrt{P_{\mu,tot} P_{tot}^\mu}. \quad (3.22)$$

The use of the invariant mass allows a one-dimensional analysis which is equivalent to a two-dimensional analysis on momentum and scattering angle, such as in Fig. 3.9b. The deviation from the known proton mass serves as an indication of the quality of the optics calibration. The center of the each  $W$  cut is determined as the peak of the hydrogen elastic events. In principle, the width of the cut should have no effect on the physical asymmetry, but only on the statistical uncertainty. In practice, inaccuracies in the background evaluation will result in cut-dependent asymmetries. For this reason, for each data point the asymmetries are extracted for a range of cut widths and a mean value is used for the asymmetry. This is also used as an evaluation on the cut-related uncertainties, as discussed in Sec. 3.4.4.

GEp kinematics cuts are well below  $\pi^-$  threshold:  $W_{\pi^-} = M_p + m_{\pi^-}$ . The cut on the invariant mass also serves as an acceptance cut for scattering angle and momentum. We also applied additional cut on  $\phi_{HCS}$ , as shown in Fig. 3.13.

### 3.3.2 Raw Asymmetries

Asymmetries were calculated for each run separately. The asymmetry and the corresponding statistical uncertainty were calculated using:

$$A = \frac{N^+ - N^-}{N^+ + N^-}, \quad (3.23)$$

$$\Delta A = \sqrt{\frac{4N^+N^-}{(N^+ + N^-)^3}}. \quad (3.24)$$

Fig. 3.14 shows raw asymmetries for left HRS runs. It should be noted that the asymmetry flips sign several times during the experiment. This is due to proactively flipping of target spin direction by changing microwave frequency, and beam helicity by introducing and removing a half-wave plate. A decrease in absolute asymmetry with time is due to polarization degradation of the target. All these effects should be corrected if dividing the asymmetry by beam and target polarization and half-wave plate status,  $A_{raw}/P_B P_T$ . The red dots in Fig. 3.14 represent this correction.

During the production of the 2.2 GeV data, target material was changed for runs 3071-3089 to the bottom slot of the target insert, before the original top target was used again. This change requires additional systematic studies due to the differences in the packing fraction of the two targets, and the statistical significance of these runs is low. We decided to omit these runs from the analysis, and this is the reason for the gap in Figs. 3.14a and 3.14b.

For the right HRS data, delays in the optics analysis prevent a complete analysis at this point. However, loose two-dimensional cuts on the focal plane were used for the extraction of raw asymmetries, as presented in Fig. 3.15.

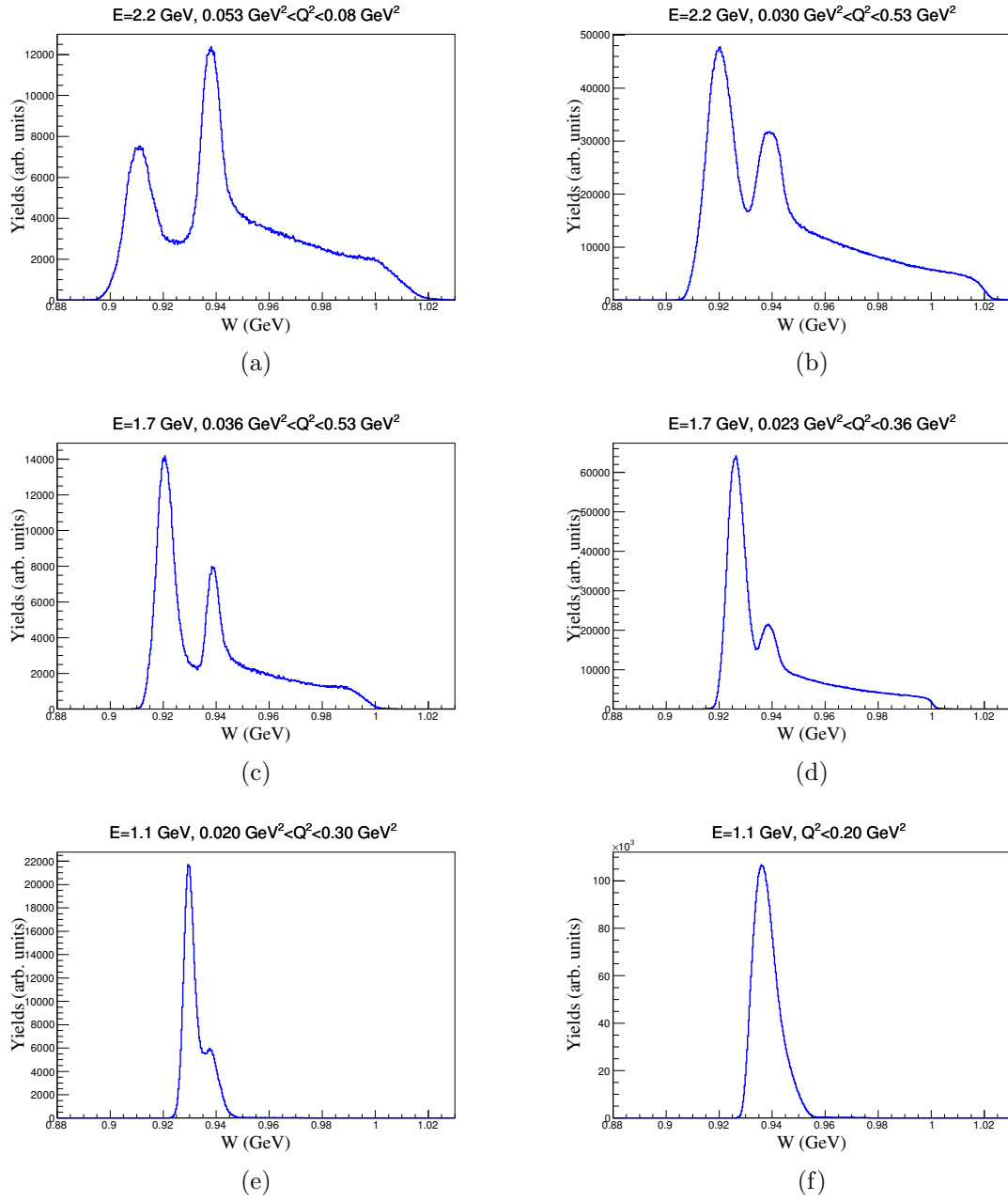


Figure 3.12: Invariant mass distributions for the left HRS at all experimental configurations. Except for the lowest  $Q^2$  setting, the hydrogen elastic events can be identified as the peak at  $\sim 938$  MeV.

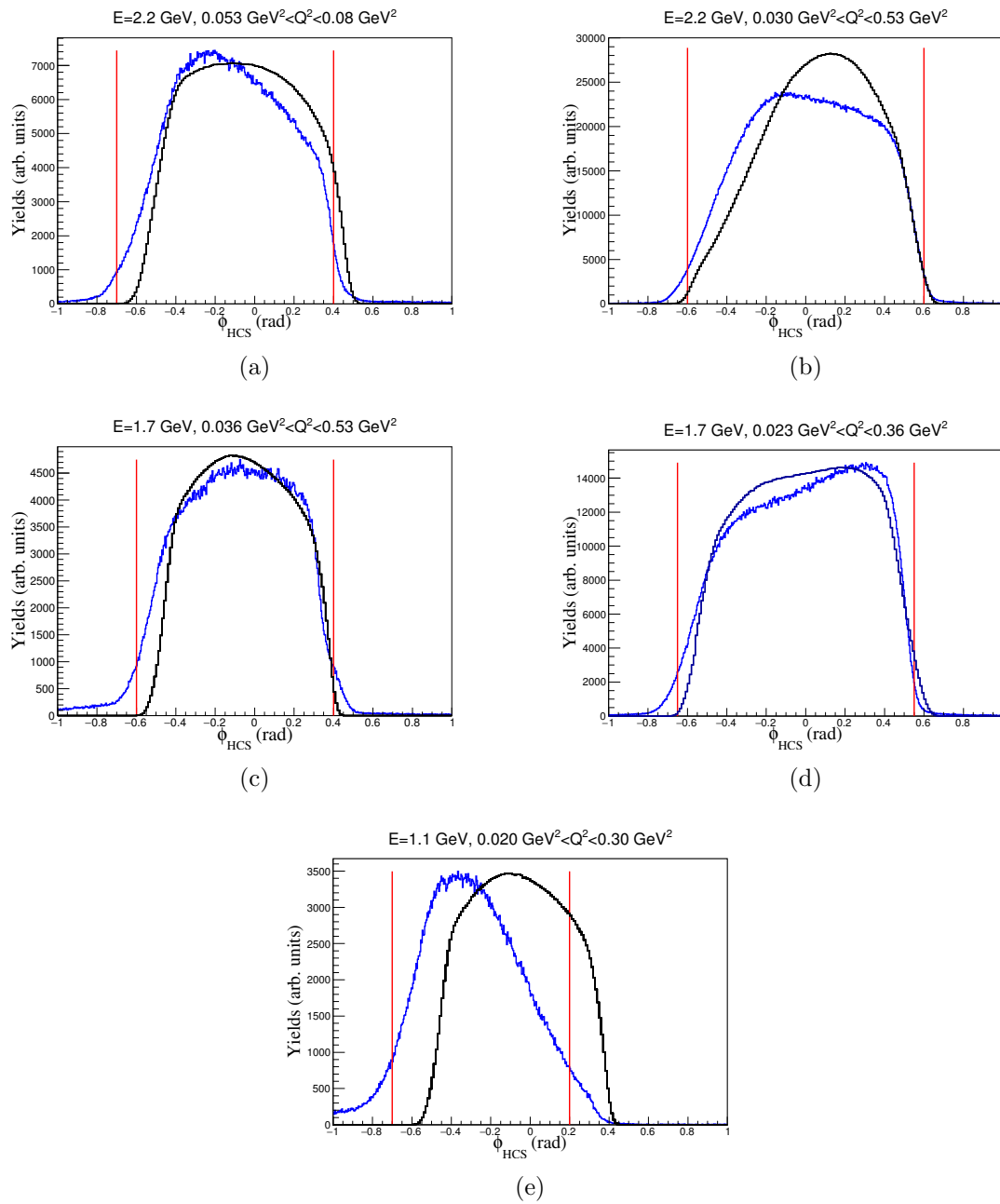


Figure 3.13:  $\phi_{HCS}$  distributions for the left HRS at all experimental configurations (blue), compared to g2psim (black, see Sec. 3.4.2). In red are the cuts that were used for the analysis.

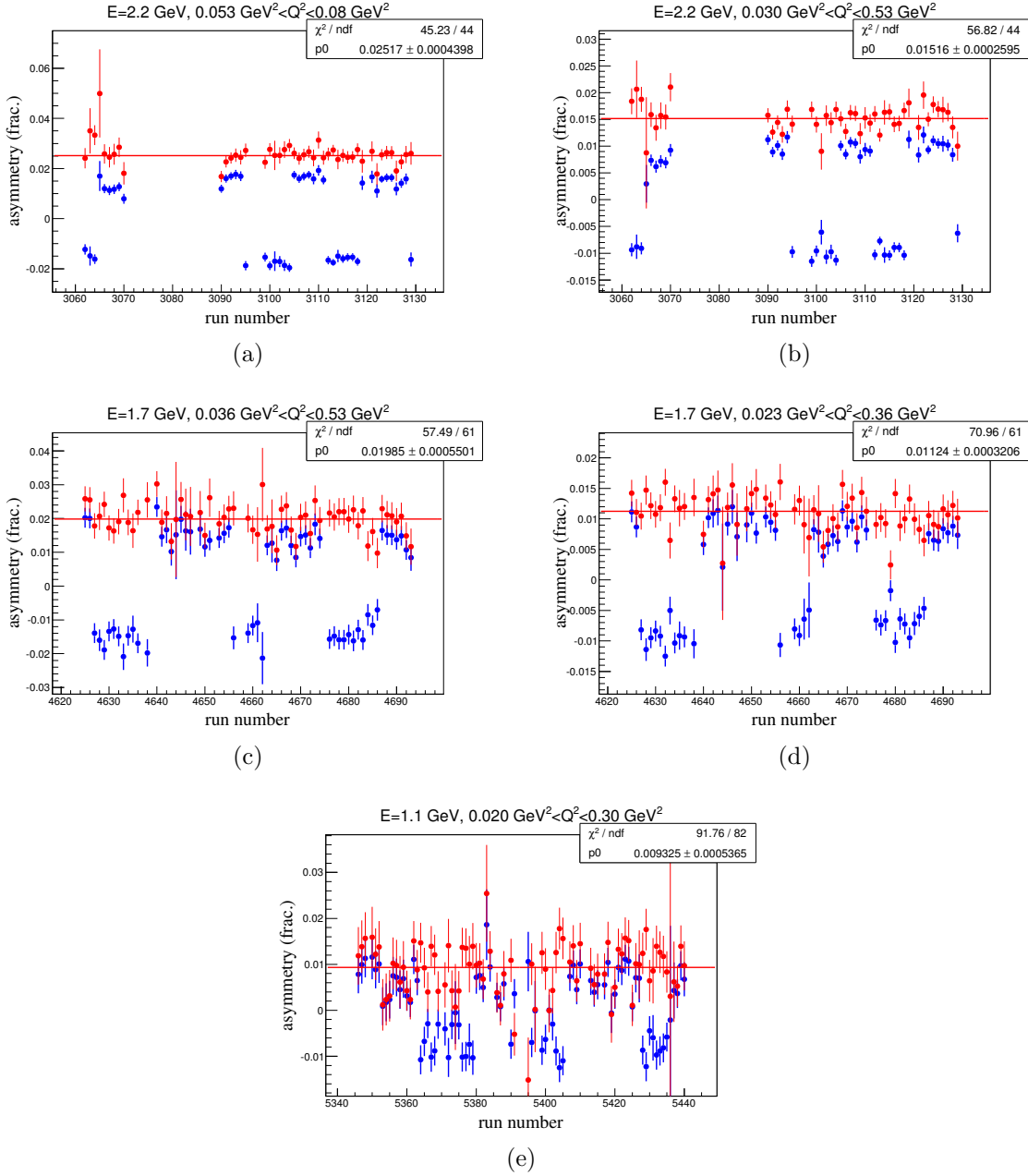
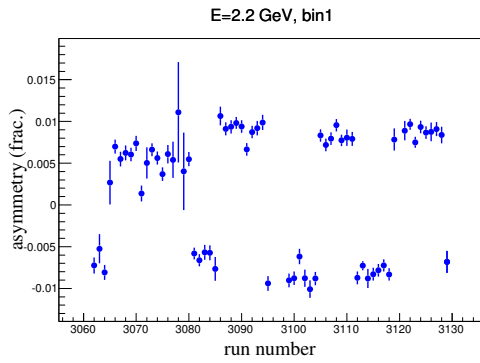
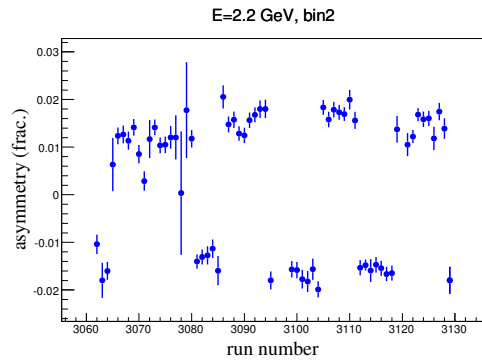


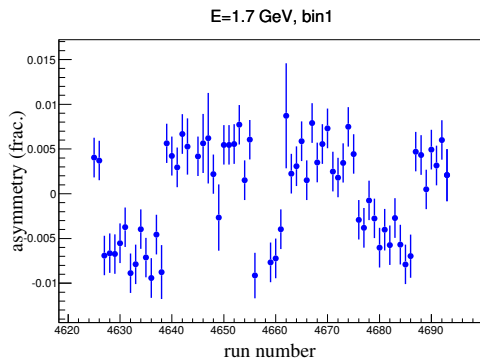
Figure 3.14: Blue: raw asymmetries for all left HRS runs. Red: raw asymmetries corrected for half-wave plate, beam and target polarizations. The fits for a constant value are done for the corrected asymmetries, and the  $\chi^2/\text{NDF}$  values show consistent statistical behavior after these corrections. The gap in the 2.2 GeV runs (a+b) is due to the change in the target material (see text).



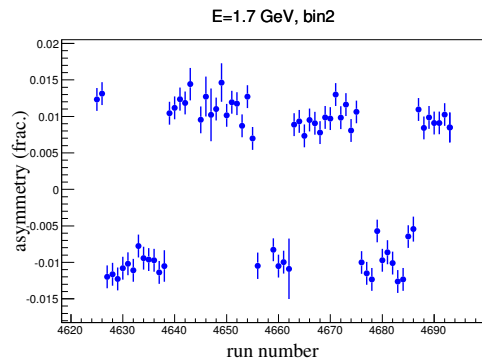
(a)



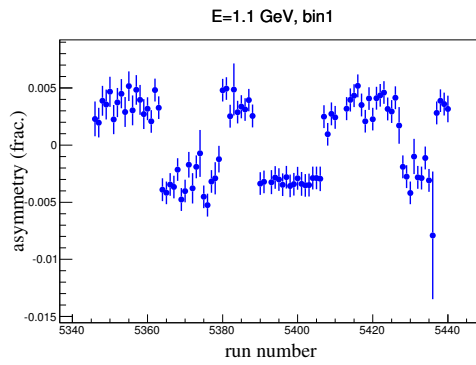
(b)



(c)



(d)



(e)

Figure 3.15: Raw asymmetries for all right HRS runs.

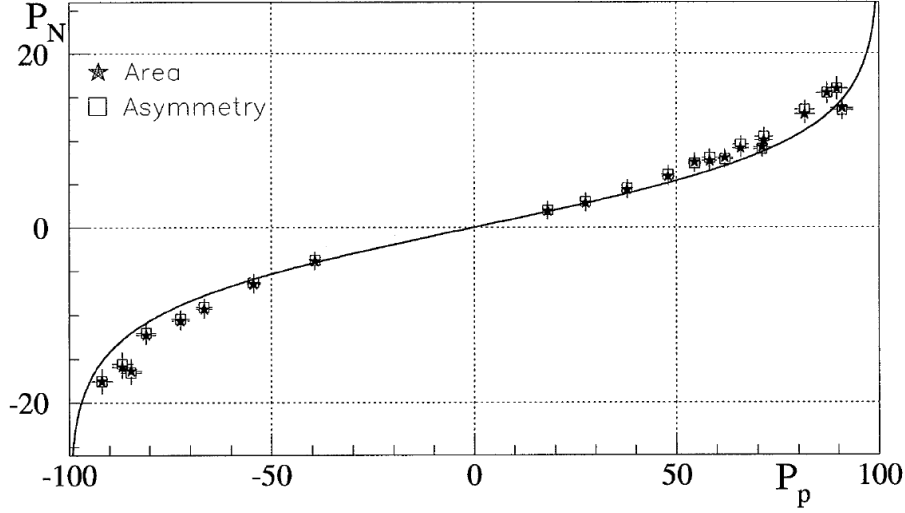


Figure 3.16:  $^{14}\text{N}$  polarization as function of proton polarization. The squares and the stars represents two methods of measurements, while the solid curve represents an EST-based calculation. Further details of the measurements and calculation can be found in [106].

## 3.4 Dilution analysis

### 3.4.1 General

The asymmetry at the proton elastic peak around  $W = 938$  MeV is diluted by two main sources of background. The first one is the radiative tail from elastic scattering off heavy elements (mainly  $^{14}\text{N}$  and  $^4\text{He}$ , but also minor contribution from  $^{27}\text{Al}$  at the entrance window). In addition, there is the background from the high energy region of the quasi-elastic (single nucleon knock-out) peaks from the heavy elements.

For an unpolarized background  $B$ , the experimental asymmetry (assuming 100% beam and target polarization) is:

$$A_{raw} = \frac{N^+ - N^-}{N^+ + N^- + B} = \frac{A_{phys}}{1 + \frac{B}{N^+ + N^-}}, \quad (3.25)$$

$$A_{raw} = A_{phys} \cdot \left(1 - \frac{B}{T}\right) \quad (3.26)$$

Where  $A_{phys}$  is the physical asymmetry, and  $T = N^+ + N^- + B$  is the total event count. We define the dilution factor  $f = 1 - B/T$  and adding the corrections for the beam and target polarization to obtain:

$$A_{phys} = \frac{A_{raw}}{f P_B P_T}. \quad (3.27)$$

In order to evaluate the amount of background below the proton elastic peak precise knowledge of relative yields between all the five reactions is required (proton elastic scattering,  $^4\text{He}$  and  $^{14}\text{N}$  elastic and quasi-elastic scattering). Monte-Carlo simulation of the experimental assembly can use cross section models and study acceptance, solid angle and radiative corrections for the evaluation of the background level within a specific cut. Although cross sections for elastic scattering are available, no experimental cross section data for  $^4\text{He}$  or  $^{14}\text{N}$  quasi-elastic reaction in the relevant kinematics exist. Furthermore, the packing fraction (i.e., the ratio between  $\text{NH}_3$  and liquid He in the target) can be extracted only to poor accuracy. In Sec. 3.4.2 we will describe our approach for dealing with the background level evaluation.

The above formula (Eq. 3.27) is correct only if the background does not contribute to the asymmetry. In our case,  $^4\text{He}$  has spin 0 and hence, does not contribute to the background.  $^{14}\text{N}$  has spin 1 and a certain amount of polarization is obtained for it. In a previous work by the Spin Muon Collaboration on a similar target, the polarization of the nitrogen was estimated to be 9%-14% for a proton polarization of 70%-90% [106] (see Fig. 3.16). The measured asymmetry is related to the physical asymmetries of the nitrogen and the proton by:

$$A_{raw} = fP_B P_T \left( A_p + \frac{n_N P_N}{n_p P_p} \frac{\sigma_N A_N}{\sigma_p} \right), \quad (3.28)$$

where  $P_N/P_p$  is the ratio between nitrogen and proton polarizations,  $n_N/n_p$  is the ratio between nitrogen and proton nuclei in the target,  $\sigma_N/\sigma_p$  is the cross section ratio, and  $A_p, A_N$  are the proton and nitrogen physical asymmetries, respectively. The authors of [106] also estimate, based on a simplified shell model approximation treating the nitrogen as a spinless carbon core with an extra proton and neutron in a  $1p_{1/2}$  orbital state, that the nitrogen asymmetry is:

$$\sigma_N A_N = -\frac{1}{3} (\sigma_p A_p + \sigma_n A_n), \quad (3.29)$$

where  $\sigma_n, A_n$  are the neutron cross section and asymmetry respectively. In our low  $Q^2$  forward kinematics an additional approximation of  $\sigma_n \ll \sigma_p$  can be used to give:

$$A_{raw} = fP_B P_T A_{phys} \left( 1 - \frac{1}{3} \frac{n_N P_N}{n_p P_p} \right), \quad (3.30)$$

$$A_{phys} \approx \frac{A_{raw}}{0.983 \cdot fP_B P_T}. \quad (3.31)$$

This approximation was originally done for deep inelastic scattering, and does not necessarily hold for the cases of elastic and quasi-elastic scattering. In addition, the ratio between nitrogen and proton contributions for the asymmetry in Eq. 3.28 does not take into account

the radiative tail from the nitrogen elastic peak. However, this approximation is the only available one, and can be used as a general estimation for the significance of this correction. Unfortunately, there is no available experimental data for nitrogen asymmetry. In Sec. 3.4.3 we will describe our method to address this problem, and will show first experimental results for nitrogen asymmetries.

### 3.4.2 g2psim

As part of the optics analysis, g2psim, a Monte-Carlo simulation of the experimental setup was developed. The simulation contains the materials and the field map along the trajectory of the scattered electron, and was used for the calibration of the optics matrix (see Sec. 3.2.2). The trajectories are calculated by integration of the equation of motion in the magnetic fields using the Runge-Kutta-Nyström method. Energy losses due to ionization, electron scattering, internal and external Bremsstrahlung are calculated, as described in [107]. As an input to the simulation, elastic models for protons,  $^4\text{He}$ ,  $^{12}\text{C}$  and  $^{14}\text{N}$  were coded based on experiment-based form factor parameterizations [108, 109]. Inelastic data at the relevant kinematics are not available. g2psim uses two models, QFS [110] and PBosted [111] as an input for the inelastic scattering. The two models produce significantly different yields at the quasi-elastic region in our kinematics. Unpublished nitrogen data at close, but not identical, kinematics were compared to these models, and PBosted model seems to produce more accurately the quasi-elastic peak. This is also indicated by the low energy region of quasi-elastic peaks in our data.

Fig. 3.17 shows a comparison between the experimental spectrum and the simulated contributions of the five reactions by g2psim. Although the yields in this figure are arbitrary, it is clear that g2psim underestimates resolution effects of the experimental system. The position of the proton elastic peak also indicates small inaccuracies in the energy loss calculation.

In order to use g2psim results for the background analysis, we treat the simulation results in two steps. The first step is to apply Gaussian smearing and shifting on an event-by-event basis. That means that each simulated event with energy  $E$  is replaced by a different energy  $E'$  normally distributed as  $E' \sim N(E + \mu, \sigma)$ , where the parameters  $\mu, \sigma$  are adjusted to agree with the experimental proton elastic peak, that serves as a clear calibration for the experimental resolution and electron energy. The same Gaussian correction is applied to all five interactions. This step accounts for the inaccuracy in the transport simulation. To deal with the lack of knowledge of the absolute yields, the magnitude of each contribution

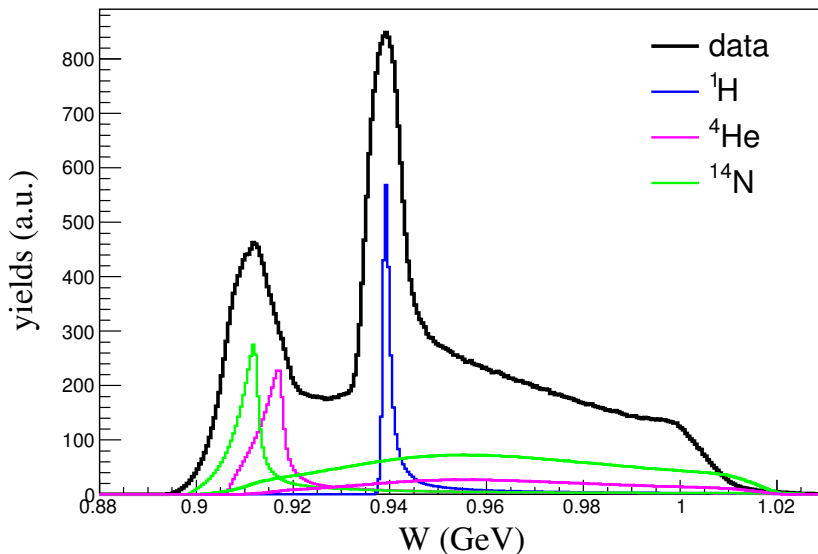


Figure 3.17: Comparison between experimental data at 2.2 GeV and g2psim output. For the heavy elements, elastic interactions (low W peaks) and quasi-elastic interactions (high W peaks) are calculated separately. The absolute yields are arbitrary for all interactions.

is scaled to the data using a minimum  $\chi^2$  fit. Fig. 3.18 shows the simulation results for all experimental configurations after the correction and the fit.

The above fitting procedure is not very sensitive to the differences between  $^4\text{He}$  and  $^{14}\text{N}$  elastic peaks, and it is almost completely insensitive to the differences between the quasi-elastic peaks of these two elements. Nevertheless, the differentiation between the three main regions in the spectrum, heavy elastics, proton elastics and quasi-elastics is very clear. For the sake of determining the background level below the proton elastic peak, we consider the above procedure sufficient. The uncertainties will be discussed in Sec. 3.4.4. We do not consider these results reliable in terms of the differences between  $^4\text{He}$  and  $^{14}\text{N}$  yields.

The azimuthal angle,  $\phi$ , was not directly used for the background analysis, but a comparison between the experimental  $\phi_{HCS}$  distribution and g2psim results can be used as an indication of the magnetic field modeling accuracy. Fig. 3.13 shows a reasonable agreement for the 2.2 GeV and 1.7 GeV configurations, while for the 1.1 GeV case the simulation underestimates the bending of the beam in the magnetic field. The procedure for the systematic studies described in Sec. 3.4.4 should account for these inaccuracies.

### 3.4.3 Physical Asymmetries Extraction

In the previous section we described how we use simulations to divide the experimental yields into the partial contributions of the different reactions. As discussed in Sec. 3.4.1, this enables the use of Eq. 3.27 to extract the physical asymmetry from the raw asymmetry, in the theoretical case of unpolarized background. If the asymmetry contribution from the nitrogen was known, we could, in principle, extract the proton physical asymmetry from the data using the procedure discussed in Sec. 3.4.1. Due to the lack of experimental data for nitrogen asymmetry for the elastic and quasi-elastic regions, the unknown packing fraction and the insensitivity of the simulations to the differences between helium and nitrogen, it is hard to evaluate the reliability of this approach.

A different approach would be to use the data itself for the extraction of physical asymmetries for all the reactions in the experiment. To deal with the packing fraction problem, and the insensitivity of the simulation to the differences between helium and nitrogen, we ignore the differences between them and treat the data as if it consisted of three reactions: proton elastics, heavy-element elastics, and quasi-elastics. To each of these reactions we attribute a physical asymmetry  $A_1, A_2, A_3$ , respectively. Each of these reactions dominates a different region in invariant mass, with some level of mixture in all three regions (see Fig. 3.19). From the data, after appropriate cuts on invariant mass, we extract raw asymmetries for each region,  $A_{raw,1}, A_{raw,2}, A_{raw,3}$ . The raw asymmetries are related to the physical asymmetries by:

$$A_{raw,i} = \sum_{j=1}^3 C_{i,j} A_j, \quad (3.32)$$

where the coefficient  $C_{i,j}$  is the partial contribution of reaction  $j$  to the yields in region  $i$ , and it is calculated from the simulation. This set of linear equations can be solved to extract the physical asymmetries for the three reactions  $A_1, A_2, A_3$ .

The main advantage of this approach is that it is based on data, and does not require knowledge of the nitrogen polarization level and asymmetry, packing fraction, elastic or quasi-elastic cross sections. It is also based on the most accurate part of the simulations. It is to be noted, that the strengths of the three main regions are very clear in the data, and the successful reproduction of the quasi-elastic region by the simulation makes the determination of  $C_{i,j}$  quite robust. A quantitative estimation of the uncertainties will be discussed in Sec. 3.4.4. An additional important advantage is that we are also extracting, for the first time, physical asymmetries for  $^{14}\text{N}$  elastic and quasi-elastic scattering. Indeed, the unknown level of  $^4\text{He}$  background implies large uncertainties on the nitrogen asymmetries. A disadvantage of this approach is that we introduce additional statistical and systematic uncertainties to

the proton asymmetries. This is due to the large relative statistical uncertainties on the small nitrogen elastic and quasi-elastic asymmetries, and the systematic uncertainties on the fit at these regions. These are introduced to the proton asymmetries through the non-diagonal coefficients in Eq. 3.32.

For the 1.1 GeV configuration, the above procedure could not be applied. The reason is that during the experiment the trigger was changed to exclude events far from the proton peak. It was done by turning off most of the s2 scintillators. This effect could not be simulated, hence statistics from the runs with the adjusted trigger were unusable for the quasi-elastic region. The physical asymmetry for this configuration was extracted using Eq. 3.27, and larger systematic uncertainty is quoted for the unknown background asymmetry.

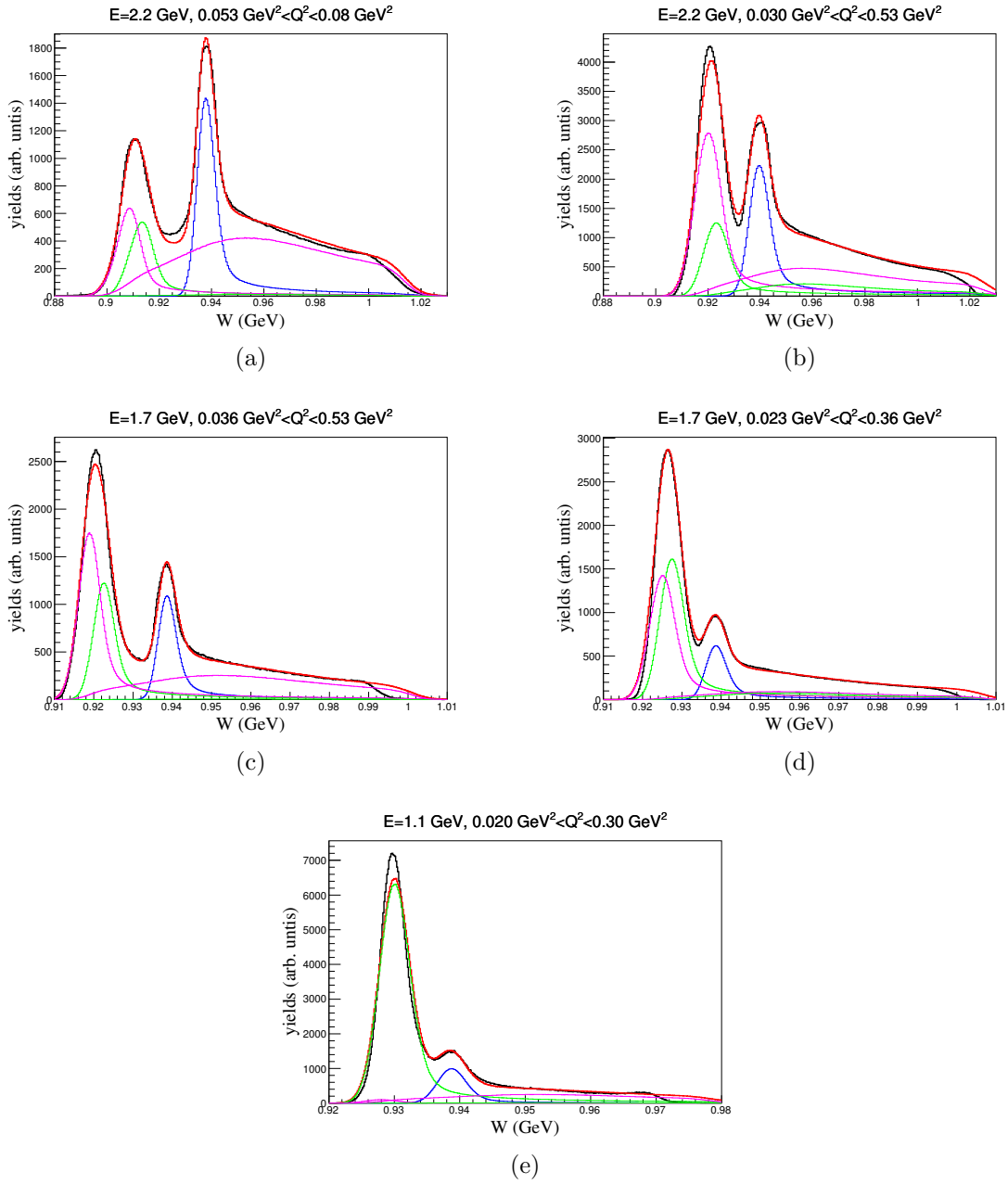


Figure 3.18: Simulation results for all experimental configurations. The black curves are the experimental data, the red curves are the total simulated yields, the blue, green and purple curves are the proton, helium and nitrogen partial contributions, respectively.

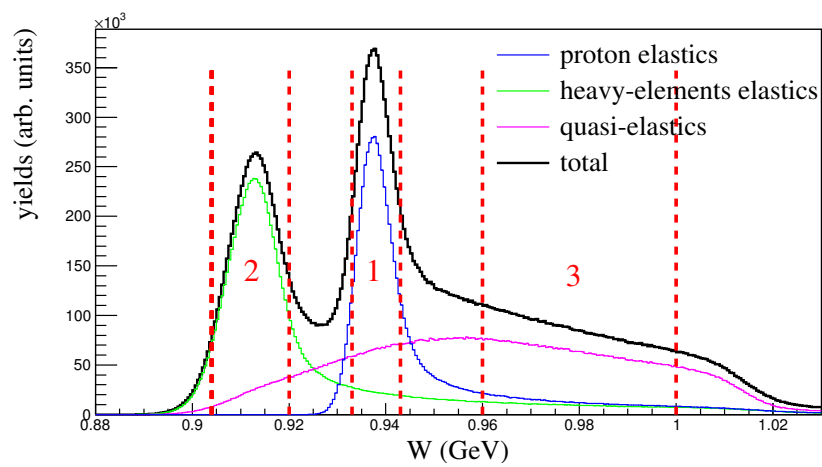


Figure 3.19: An example of invariant mass histogram divided into three regions, each dominated by different reaction: proton elastics (1), heavy-elements elastics (2) and quasi-elastics (3). The partial contribution of each reaction is determined based on simulation.

$\times 10^{-7}$	$A_1$	$A_2$	$A_3$
$A_1$	4.66	0.21	-1.57
$A_2$	0.21	3.00	-0.79
$A_3$	-1.57	-0.79	3.07

(a)  $0.053 < Q^2 < 0.080 \text{ GeV}^2$

$\times 10^{-7}$	$A_1$	$A_2$	$A_3$
$A_1$	1.92	-0.06	-0.64
$A_2$	-0.06	0.46	-0.16
$A_3$	-0.64	-0.16	1.36

(b)  $0.030 < Q^2 < 0.053 \text{ GeV}^2$

$\times 10^{-7}$	$A_1$	$A_2$	$A_3$
$A_1$	6.62	0.01	-1.93
$A_2$	0.01	1.03	-0.48
$A_3$	-1.93	-0.48	4.49

(c)  $0.036 < Q^2 < 0.053 \text{ GeV}^2$

$\times 10^{-7}$	$A_1$	$A_2$	$A_3$
$A_1$	0.36	-0.07	-0.86
$A_2$	-0.07	0.24	-0.16
$A_3$	-0.86	-0.16	2.13

(d)  $0.023 < Q^2 < 0.036 \text{ GeV}^2$

Table 3.3: Covariance matrices for 2.2 GeV (top) and 1.7 GeV (bottom) configurations. See text for the meaning of  $A_1, A_2, A_3$ . The matrices are calculated with 5 MeV invariant mass cut at 2.2 GeV and 2.5 MeV invariant mass cut at 1.7 GeV. All values should be multiplied by  $10^{-7}$ .

### 3.4.4 Uncertainties

In this section we will discuss the uncertainties related to the dilution analysis and asymmetry extraction procedure described above.

Statistical asymmetries were extracted in two steps. The first step was to assign statistical uncertainties to each experimental raw asymmetry according to Eq. 3.24. The statistical uncertainties of the physical asymmetries,  $A_1, A_2$ , and  $A_3$  should be derived from Eq. 3.32, to account for the mixture between the asymmetries in the raw asymmetries. We calculated these uncertainties with brute force by Monte-Carlo. For each extraction of physical asymmetries, Eq. 3.24 was solved  $10^6$  times, each of them with  $A_{raw,i}$  randomly generated around the experimental values with the appropriate variance. The mean of the resulting distribution was used as the physical asymmetry, and the variance as the statistical uncertainty. The correlations between the three reactions were also calculated by Monte-Carlo using the definition:

$$\Sigma_{i,j} = \sum_n (X_{i,n} - \bar{X}_i)(X_{j,n} - \bar{X}_j)/N, \quad (3.33)$$

where  $X_{i,n}$  is the  $n$ 's calculated asymmetry for reaction  $i$ ,  $\bar{X}_i$  is the mean asymmetry for reaction  $i$ , and  $N$  is the total number of events in the Monte-Carlo. Table 3.3 lists the covariance matrices for the 1.7 and 2.2 GeV configurations.

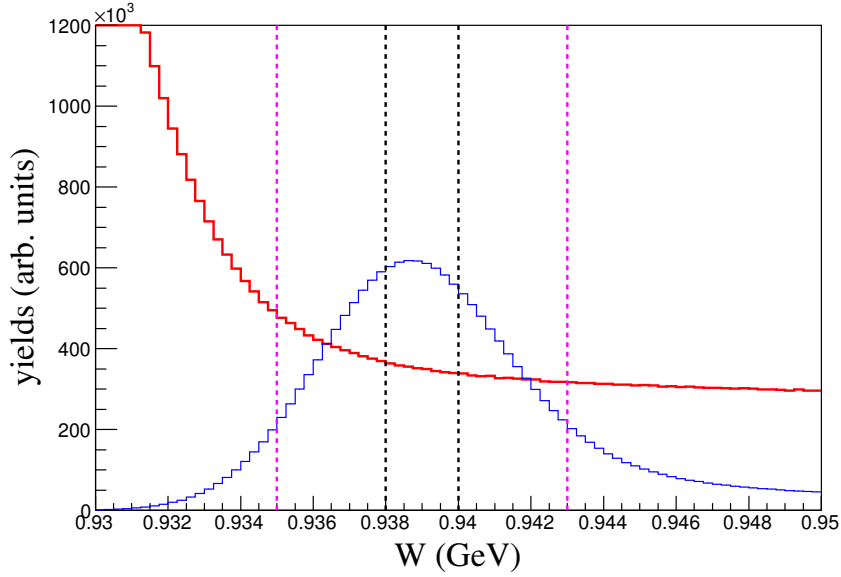


Figure 3.20: An example of simulated background (red) relative to the simulated proton elastic peak (blue). Invariant mass cuts of  $\pm 1$  MeV (black) and  $\pm 4$  MeV (purple) are drawn in dashed lines. The proton-to-background ratio changes significantly with cut width.

The systematic robustness of the dilution analysis and asymmetry extraction are tested in two ways. The first way is to change the invariant mass cut width over a wide range relative to the proton peak width, and the second way is to change the simulation energy and resolution calibrations,  $\mu$  and  $\sigma$ , in ranges that produce reasonable agreement with data. These specific tests follow the analysis procedure, they have some degree of correlation, and not necessarily represent all the aspects of the systematic effects. However, we treat them as uncorrelated and sufficient for the reasons listed below.

The systematic uncertainties should not be studied on their own, but as they affect the asymmetries. Fig. 3.20 shows an example of the total background, as calculated by the simulation, relative to the proton elastic peak from the same simulation. The change in cut width has significant effect on the dilution factor,  $f$ . In the presented example, changing the cut from  $\pm 1$  to  $\pm 4$  MeV reduces the dilution factor from 0.629 to 0.544, which translates to  $\sim 15\%$  difference in the experimental asymmetry. In Fig. 3.21 the drop in the raw asymmetry is evident as  $W$  cut increases and the proton peak is more diluted. A perfect dilution analysis would eliminate this drop. Fig. 3.22 shows the physical asymmetries as were extracted with different cut widths. The variations in physical asymmetries indicate the effect of the inaccuracies in the background model on the extracted asymmetries. Qualitatively, the fact that in all configurations, in spite of non-trivial background shape and significant differences in

beam energy (GeV)	$Q^2$ (GeV <sup>2</sup> )	relative uncertainty (%)
2.2	0.053-0.080	0.26
2.2	0.030-0.053	0.19
1.7	0.036-0.053	0.36
1.7	0.023-0.036	0.01
1.1	0.020-0.030	1.08

Table 3.4: Systematic uncertainties due to invariant mass cut width. The uncertainties are given relative to the extracted asymmetries.

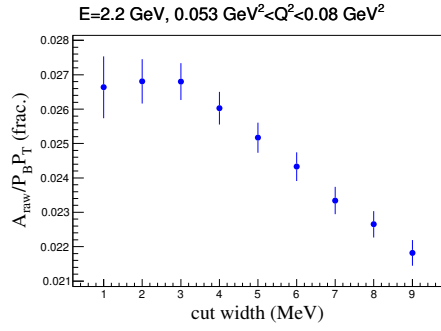
proton-to-background ratios, the fluctuation in physical asymmetries as a function of invariant mass cut width are small, indicates that the simulations and the extraction procedure are reliable. Exceptions are the tightest cuts, that in some cases show significant deviation from the other cuts. This is reasonable since they are most sensitive to fine resolution effects that are not accounted for by the simulation. These are smeared in the wider cuts. A quantitative estimation of the systematic effects, however, is not done based on cut widths but by changing the simulation parameters as follows. Since  $W$  cut width is an additional arbitrary parameter in the analysis that has effect on the results, we still use the fluctuations of the extracted asymmetries with cut width as an additional uncorrelated systematic uncertainty. The systematic uncertainties due to the cut width are listed in Table 3.4.

An additional systematic check of the simulations was done by changing the simulation energy and resolution calibration,  $\mu$  and  $\sigma$ , as described in Sec. 3.4.2. The smearing and shifting parameters are scanned within a reasonable range (in terms of reproducing the data), and the full asymmetry extraction procedure is done for each  $(\mu, \sigma)$ . The uncertainty is estimated based on the range of asymmetries obtained. We used conservative estimations of 2% for the proton asymmetries, 10% for the heavy-elastic peak asymmetries and 25% for the quasi-elastic peak asymmetries. For the 1.1 GeV case, nitrogen asymmetries could not be extracted and the systematic uncertainty for proton asymmetry was estimated to 3.5%. Fig. 3.23 illustrates this procedure.

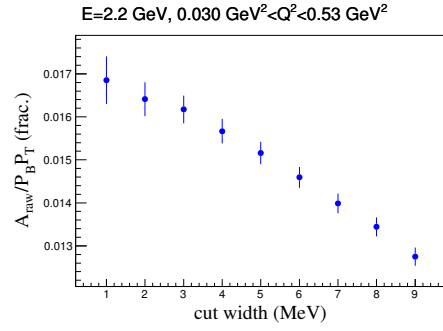
Nitrogen polarization was calculated from proton polarization based on [106] (see Sec. 3.4.1). The uncertainty of the nitrogen polarization is evaluated, based on the differences between the EST model and the experimental data in Fig. 3.16, to be 15% relative.

Nitrogen elastic and quasi-elastic asymmetries are diluted by the presence of <sup>4</sup>He. The ratio between helium and nitrogen in the data could not be extracted from the simulation. Due to the low accuracy extraction of nitrogen asymmetries in this experiment, a dilution

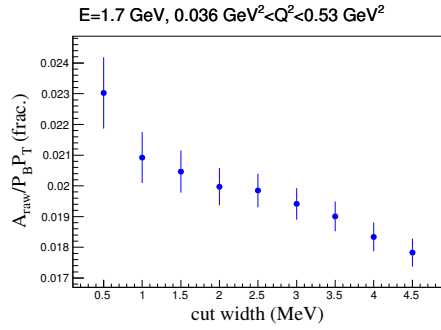
factor of  $f_{14N} = 0.75 \pm 0.25$  is used.



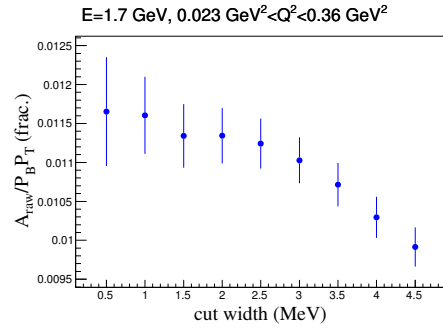
(a)



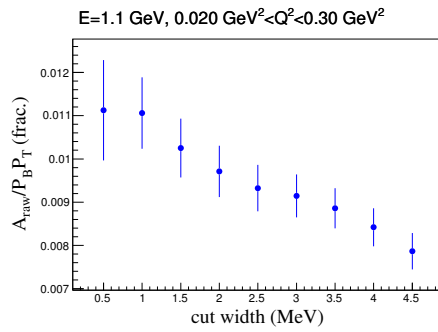
(b)



(c)

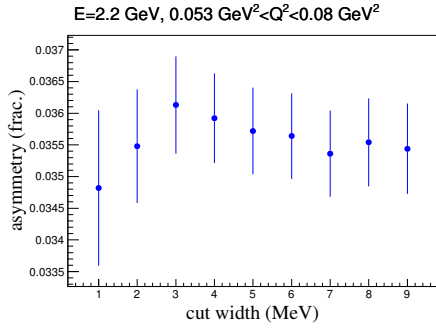


(d)

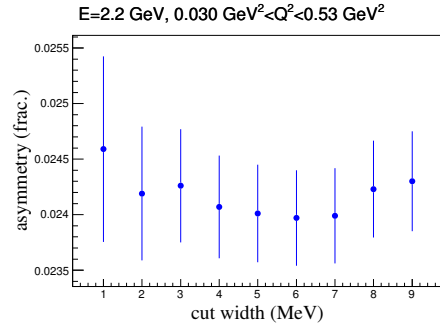


(e)

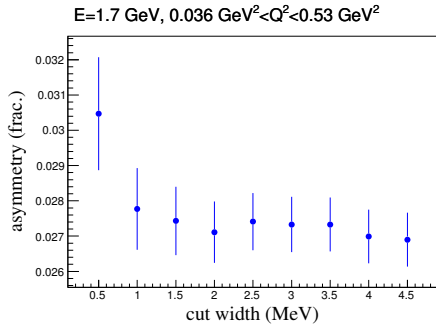
Figure 3.21: Polarization-corrected raw asymmetries,  $A_{raw}/P_B P_T$  as function of invariant mass cut width. A decrease in raw asymmetry is evident as cut width increases due to the lower proton-to-background ratio. Error bars represents statistical uncertainties, which are highly correlated between different cuts.



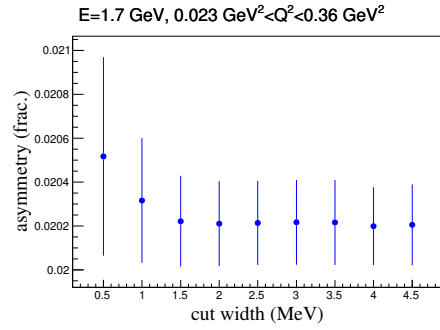
(a)



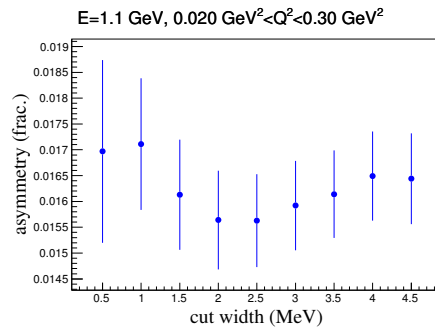
(b)



(c)

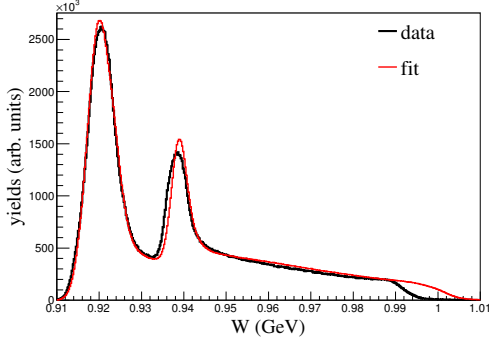


(d)

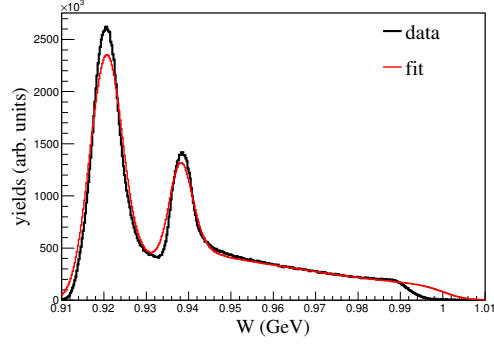


(e)

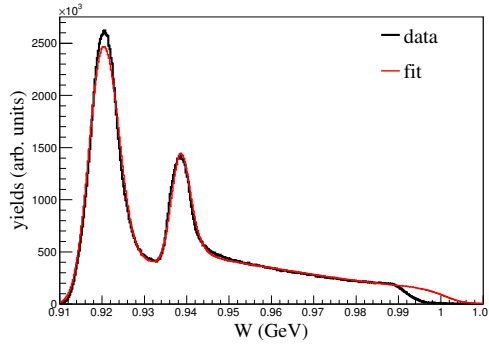
Figure 3.22: Physical asymmetries as a function of invariant mass cut width. Physical asymmetries extracted according to the procedure described in the text. Except for the tightest cuts, consistent values obtained for the different cut widths. Error bars represents statistical uncertainties, which are highly correlated between different cuts.



(a)  $\mu = 0.1$  MeV,  $\sigma = 1.6$  MeV



(b)  $\mu = 1.0$  MeV,  $\sigma = 2.5$  MeV



(c)  $\mu = 0.5$  MeV,  $\sigma = 2.0$  MeV

Figure 3.23: Systematic study of simulation-related uncertainty. The uncertainty is estimated by changing the parameters of the smearing Gaussian, which represents energy calibration ( $\mu$ ) and resolution adjustment ( $\sigma$ ). The plots show two extreme parameterizations that still produce reasonable fits (top), and the parameterization that is used for the asymmetry extraction (bottom). The extracted asymmetries in this case varies between 2.72%-2.77% for protons, 0.078%-0.081% for the heavy-elastic peak, and 0.186%-0.233% for the quasi-elastic peak. Based on the entire data set, conservative systematic uncertainties of 2%, 10% and 25%, respectively, were estimated.

# Chapter 4

## Results and Discussion

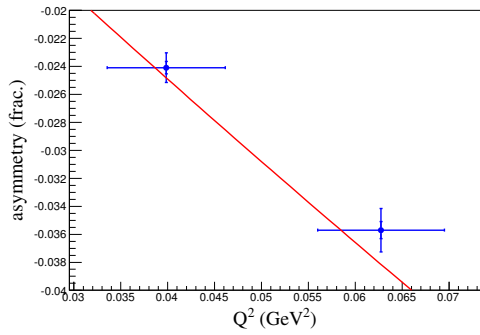
The analysis of the experiment is not yet completed, and form factor ratios have yet to be extracted. These will have to wait for the complete analysis of both arms. We will show here our results for the asymmetries. Since the analysis of the right arm should improve our understanding of the system and the extraction of the asymmetries, the below results should be treated as preliminary results.

### 4.1 Proton Asymmetries

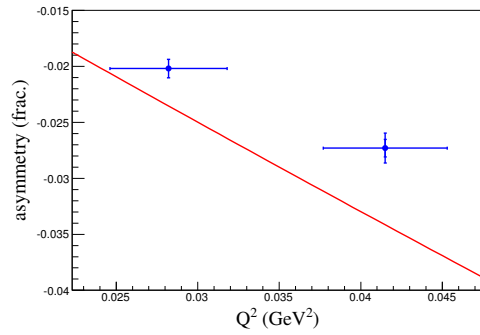
Results of physical asymmetries for electron-proton elastic scattering are listed in Table 4.1 and plotted in Fig. 4.1. The results are for the left arm asymmetries. Right arm asymmetries are still under analysis. The asymmetries were extracted for the  $Q^2$  ranges listed in Table 4.1. The  $Q^2$  values plotted in Fig. 4.1 are the RMS values of  $Q^2$  distributions within bin cuts, and the horizontal error bars are the STD values of these distributions. These should not be confused with the weighted-averaged  $Q^2$  values and their uncertainties that are model dependent and were not calculated here.

beam energy (GeV)	$Q^2$ (GeV <sup>2</sup> )	$A$ (%)	$\Delta A_{stat}$ (%)	$\Delta A_{sys}$ (%)
2.2	0.053-0.080	-3.57	0.061	0.142
2.2	0.030-0.053	-2.41	0.044	0.096
1.7	0.036-0.053	-2.73	0.078	0.109
1.7	0.023-0.036	-2.02	0.019	0.081
1.1	0.020-0.030	-1.63	0.083	0.082

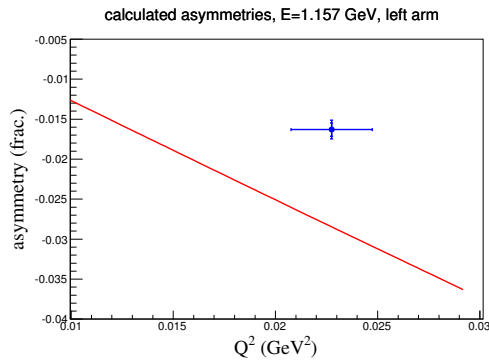
Table 4.1: Proton asymmetries with their absolute statistical and systematic uncertainties.



(a)  $E = 2.2$  GeV



(b)  $E = 1.7$  GeV



(c)  $E = 1.1$  GeV

Figure 4.1: Physical asymmetries for electron-proton elastic scattering. The solid line is the calculated asymmetry using the dipole parametrization (Eq.1.53). See text for the meaning of the the horizontal error bars.

beam energy (GeV)	$Q^2$ (GeV <sup>2</sup> )	$A$ (%)	$\Delta A_{stat}$ (%)	$\Delta A_{sys}$ (%)
2.2	0.053-0.080	0.66	0.54	0.32
2.2	0.030-0.053	0.62	0.21	0.30
1.7	0.036-0.053	0.76	0.29	0.36
1.7	0.023-0.036	0.49	0.14	0.24

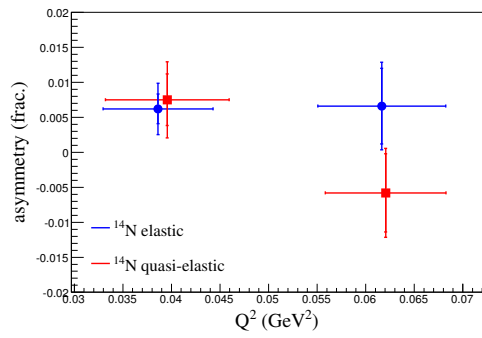
Table 4.2: <sup>14</sup>N elastic asymmetries with their absolute statistical and systematic uncertainties.

beam energy (GeV)	$Q^2$ (GeV <sup>2</sup> )	$A$ (%)	$\Delta A_{stat}$ (%)	$\Delta A_{sys}$ (%)
2.2	0.053-0.080	-0.58	0.56	0.31
2.2	0.030-0.053	0.75	0.37	0.40
1.7	0.036-0.053	-1.82	0.61	0.97
1.7	0.023-0.036	-0.77	0.41	0.41

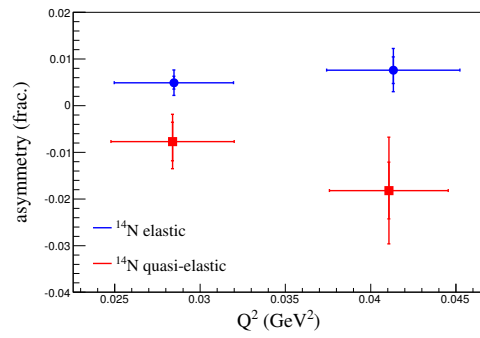
Table 4.3: <sup>14</sup>N quasi-elastic asymmetries with their absolute statistical and systematic uncertainties.

## 4.2 Nitrogen Asymmetries

Results for physical asymmetries for electron-<sup>14</sup>N elastic scattering are listed in Table 4.2 and asymmetries for electron-<sup>14</sup>N quasi-elastics scattering are listed in Table 4.3. Fig. 4.2 compares both asymmetries. See Sec. 4.1 for the meaning of the horizontal error bars in this figure. The results are for the left arm asymmetries. Right arm asymmetries are still under analysis.



(a)  $E = 2.2$  GeV



(b)  $E = 1.7$  GeV

Figure 4.2: Physical asymmetries for electron- $^{14}\text{N}$  elastic (blue circles) and quasi-elastic (red squares) scattering. See text for the meaning of the the horizontal error bars.

origin	statistical (%)	systematic (%)
beam polarization	0.20	1.70
target polarization	0.75	2.9
asymmetry cuts	-	0-1.1
asymmetry extraction	0.9-5.1	2.0-3.5

(a) Proton elastic uncertainties

origin	statistical (%)	systematic (%)
beam polarization	0.20	1.70
target polarization	0.75	15
asymmetry extraction	30-80	10
$^4\text{He}$ dilution	-	44

(b)  $^{14}\text{N}$  elastic uncertainties

origin	statistical (%)	systematic (%)
beam polarization	0.20	1.70
target polarization	0.75	15
asymmetry extraction	30-100	25
$^4\text{He}$ dilution	-	44

(c)  $^{14}\text{N}$  quasi-elastic uncertainties

Table 4.4: A summary of asymmetry uncertainties for electron-proton elastic (a), electron- $^{14}\text{N}$  elastic (b) and electron- $^{14}\text{N}$  quasi-elastic scattering (c). The tables list ranges over the whole dataset, and specific total uncertainties are listed in Tables 4.1,4.2,4.3.

### 4.3 Summary of Uncertainties

A detailed description of the various sources of uncertainties in this experiment can be found throughout this report. Table 4.4 contains a summary of the relative uncertainties of the physical asymmetries extraction. As explained in Sec. 3.2.4, an uncertainty of 2 mrad is associated with the scattering angle.

## 4.4 Discussion

### 4.4.1 Proton Asymmetries

As mentioned above and in Sec. 4.5, the analysis of the right arm might improve our understanding of the system, the optics, the simulations, and the polarization levels. The proton asymmetries presented here should be treated as preliminary asymmetries. Furthermore, a physical interpretation of the asymmetries should start with a proper averaging of  $Q^2$  distributions over bin acceptance, using form factor models, to determine the mean values of the kinematic parameters  $Q^2$ ,  $\theta$ ,  $\theta^*$ , and  $\phi^*$ . However, the general trend of the data suggests significantly lower asymmetries (in absolute values) than could be expected by the existing models, especially for the 1.7 GeV and 1.1 GeV configurations. In the most general terms, this discrepancy might originate from either inaccuracies in the experiment or its analysis, or from inaccuracies in the form factor ratio models at low  $Q^2$ .

An additional inaccuracy in the experiment might be the reconstruction of the scattering angle. Misalignment of the chicane magnets, error in the field map, or in the optic matrix can all result in wrong scattering angles. The elastic peak correction should eliminate the possibility of large errors in the scattering angle, and the position of the proton peak in the invariant mass distribution should indicate such an error. Such indications were not found in the data. Significant underestimates of the energy losses along the electron trajectory might result in a larger reconstructed scattering angle that would not be corrected by position of the elastic peak and decrease the discrepancy between the extracted asymmetries and the models, but only if accompanied by an independent angle reconstruction error to the same direction. Another possible inaccuracy might stem from underestimating the background evaluation by the simulations (current elastic peak corrections are to the opposite direction). At least for the proton asymmetries, the systematic checks described in Sec. 3.4.4, the good agreement with data, and the fact that the simulations sometimes overestimate and sometimes underestimate the data at the region between the elastic peaks make it unlikely that a systematic and significant under estimation of the background exists. The final potential option for experimental inaccuracy is a systematic overestimation of the beam or target polarizations. Both Møller measurement of beam polarization, and UVa polarized target analysis are well-established procedures that were used for many experiments in the past.

If the extracted asymmetries are correct, and a proper weighting will indicate lower asymmetries relative to the existing models, this might be an indication of a form factor ratio greater than unity at low  $Q^2$ . Although such a trend might be seen below  $Q^2=0.2$  GeV

in the BLAST data [34] and in one parametrization [49], it would have to be a very strong increase to account for the extracted asymmetries in this experiment. We believe that any conclusions about the ratios must wait for the finalization of the right arm analysis.

#### 4.4.2 Nitrogen Asymmetries

Nitrogen asymmetries were extracted experimentally for the first time. These asymmetries are important for the analysis of experiments with polarized  $\text{NH}_3$  targets. The accuracy of our results is low, but sufficient to evaluate the significance of the nitrogen asymmetries for experiments with such targets. We also demonstrate a method for the extraction of these asymmetries.

These asymmetries are also interesting on their own, for the study of the  $^{14}\text{N}$  nucleus and shell model approximations. The extracted asymmetries show general agreement with the approximations made by [106] for DIS, at least in absolute values. Regarding the sign of the asymmetries, it seems that  $^{14}\text{N}$  elastic and quasi-elastic asymmetries have opposite signs. While the elastic asymmetries are very clean and it is very clear that they show opposite sign relative to the proton asymmetries, the quasi-elastic asymmetries are heavily mixed with radiative tails from both nitrogen and proton elastic peaks. Although the uncertainties were carefully studied and conservatively estimated, a significant unknown error in the radiative model or in the simulations might change the sign of the nitrogen quasi-elastic asymmetries. Note that such a change might be due to underestimation of the proton elastic strength in the quasi-elastic low energy region. It is likely that such error will result in even lower proton asymmetries, due to the decrease in the strength of the quasi-elastic background level. Hence, a change in the sign of the quasi-elastic asymmetries is correlated with a decrease in proton asymmetries (in absolute values). With the appropriate caution for preliminary results, we can state that it is unlikely that  $^{14}\text{N}$  elastic and quasi-elastic asymmetries share the same sign. This experimental result should motivate further studies.

### 4.5 Future Outlook

Right HRS data analysis is ongoing. When right arm optics, simulations, and asymmetries are ready, an extensive study should be done to compare systematic effects between the two arms. In Sec. 4.4.1 we listed several potential causes for unknown errors in the analysis. Some of these causes are common for both arms, such as beam and target polarization, and some are partially independent, such as scattering angle reconstruction and some aspects

of the the simulations. Septum magnetic field is also different, and, as a result, scattering angles are not the same. The results from the right arm should improve our understanding on whether the discrepancies between the extracted asymmetries and the models are the result of yet unknown systematics or if are they representing a real deviation of the from factors from the models.

Similar experiments in the future are advised to spend more time on systematic studies during the experiment itself. A dedicated measurement of nitrogen yields in the same kinematics and magnetic fields might obviate the need of simulations. More TE measurements of the target might significantly decrease the systematics of the polarization level.

Much more precise measurement of nitrogen asymmetries might be achieved by increasing the scattering angle. This will improve the separation between the three reactions, and even enable evaluating the exact level of the unpolarized  $^4\text{He}$  background. In parallel, a shell model approximation of the ratio between proton and nitrogen asymmetries at the elastic and quasi-elastic region can be performed, to examine if there are theoretical reasons for the opposite signs of the asymmetries.

# Bibliography

- [1] I. Estermann, R. Frisch, and O. Stern. Magnetic moment of the proton. *Nature*, 132: 169–170, 1933. doi: 10.1038/132169a0.
- [2] G Peter Lepage and S J Brodsky. Exclusive processes in perturbative quantum chromodynamics. *Phys. Rev. D*, 22(9):2157, 1980.
- [3] CF Perdrisat, V Punjabi, and M Vanderhaeghen. Nucleon electromagnetic form factors. *Progs. Part. Nucl. Phys.*, 59(2):694–764, 2007.
- [4] J Arrington. How well do we know the electromagnetic form factors of the proton? *Phys. Rev. C*, 68(3):034325, 2003.
- [5] J Arrington. Implications of the discrepancy between proton form factor measurements. *Phys. Rev. C*, 69(2):022201, 2004.
- [6] C E Hyde-Wright and K De Jager. Electromagnetic form factors of the nucleon and compton scattering. *arXiv preprint nucl-ex/0507001*, 2005.
- [7] J Arrington, CD Roberts, and JM Zanotti. Nucleon electromagnetic form factors. *J. Phys. G: Nucl. Part. Phys.*, 34(7):S23, 2007.
- [8] R Pohl et al. The size of the proton. *Nature*, 466:213–216, July 2010. URL <http://dx.doi.org/10.1038/nature09250>.
- [9] A Antognini et al. Proton structure from the measurement of 2s-2p transition frequencies of muonic hydrogen. *Sci.*, 339(6118):417–420, 2013. doi: 10.1126/science.1230016. URL <http://science.sciencemag.org/content/339/6118/417>.
- [10] M E Peskin and D V Schroeder. *An Introduction to Quantum Field Theory*. Reading, USA: Addison-Wesley, 1995.

- [11] R. G. Sachs. High-energy behavior of nucleon electromagnetic form factors. *Phys. Rev.*, 126:2256–2260, 1962. doi: 10.1103/PhysRev.126.2256. URL <http://link.aps.org/doi/10.1103/PhysRev.126.2256>.
- [12] L. N. Hand, D. G. Miller, and Richard Wilson. Electric and magnetic form factors of the nucleon. *Rev. Mod. Phys.*, 35:335–349, 1963. doi: 10.1103/RevModPhys.35.335. URL <http://link.aps.org/doi/10.1103/RevModPhys.35.335>.
- [13] MN Rosenbluth. High energy elastic scattering of electrons on protons. *Phys. Rev.*, 79(4):615, 1950.
- [14] Akheizer A. I. and Rekalov M. P. Polarization effects in the scattering of leptons by hadrons. *Sov. J. Part. Nucl.*, 4(3), 1974.
- [15] Raymond G. Arnold, Carl E. Carlson, and Franz Gross. Polarization transfer in elastic electron scattering from nucleons and deuterons. *Phys. Rev. C*, 23:363–374, 1981. doi: 10.1103/PhysRevC.23.363. URL <http://link.aps.org/doi/10.1103/PhysRevC.23.363>.
- [16] T.W Donnelly and A.S Raskin. Considerations of polarization in inclusive electron scattering from nuclei. *Ann. Phys.*, 169(2):247 – 351, 1986. ISSN 0003-4916. doi: [http://dx.doi.org/10.1016/0003-4916\(86\)90173-9](http://dx.doi.org/10.1016/0003-4916(86)90173-9). URL <http://www.sciencedirect.com/science/article/pii/0003491686901739>.
- [17] IA Qattan et al. Precision rosenbluth measurement of the proton elastic form factors. *Phys. Rev. Lett.*, 94(14):142301, 2005.
- [18] L Andivahis et al. Measurements of the electric and magnetic form factors of the proton from  $Q^2=1.75$  to  $8.83$  (GeV/c) $^2$ . *Phys. Rev. D*, 50(9):5491, 1994.
- [19] RC Walker, , et al. Measurements of the proton elastic form factors for  $1 \leq Q^2 \leq 3$  (GeV/c) $^2$  at slac. *Phys. Rev. D*, 49(11):5671, 1994.
- [20] GG Simon, Ch Schmitt, F Borkowski, and VH Walther. Absolute electron-proton cross sections at low momentum transfer measured with a high pressure gas target system. *Nucl. Phys. A*, 333(3):381–391, 1980.
- [21] F Borkowski, P Peuser, GG Simon, VH Walther, and RD Wendling. Electromagnetic form factors of the proton at low four-momentum transfer. *Nucl. Phys. A*, 222(2): 269–275, 1974.

- [22] JJ Murphy, YM Shin, and DM Skopik. Proton form factor from 0.15 to 0.79 fm<sup>2</sup>. *Phys. Rev. C*, 9:2125–2129, 1974.
- [23] W Bartel, F-W Büsser, W-R Dix, R Felst, D Harms, H Krehbiel, PE Kuhlmann, J McElroy, J Meyer, and G Weber. Measurement of proton and neutron electromagnetic form factors at squared four-momentum transfers up to 3 (GeV/c)<sup>2</sup>. *Nucl. Phys. B*, 58(2):429–475, 1973.
- [24] KM Hanson, JR Dunning Jr, M Goitein, T Kirk, LE Price, and R Wilson. Large-angle quasielastic electron-deuteron scattering. *Phys. Rev. D*, 8(3):753, 1973.
- [25] LE Price, JR Dunning Jr, M Goitein, K Hanson, T Kirk, and R Wilson. Backward-angle electron-proton elastic scattering and proton electromagnetic form factors. *Phys. Rev. D*, 4(1):45, 1971.
- [26] Ch Berger, V Burkert, G Knop, B Langenbeck, and K Rith. Electromagnetic form factors of the proton at squared four-momentum transfers between 10 and 50 fm<sup>2</sup>. *Phys. Lett. B*, 35(1):87–89, 1971.
- [27] J Litt et al. Measurement of the ratio of the proton form factors,  $G_E/G_M$ , at high momentum transfers and the question of scaling. *Phys. Lett. B*, 31(1):40–44, 1970.
- [28] T Janssens, R Hofstadter, EB Hughes, and MR Yearian. Proton form factors from elastic electron-proton scattering. *Phys. Rev.*, 142(4):922, 1966.
- [29] ME Christy, , et al. Measurements of electron-proton elastic cross sections for  $0.4 < Q^2 < 5.5$  (GeV/c)<sup>2</sup>. *Phys. Rev. C*, 70(1):015206, 2004.
- [30] Xiaohui Zhan. *High Precision Measurement of the Proton Elastic Form Factor Ratio at Low  $Q^2$* . PhD thesis, MIT, 2010.
- [31] P E Bosted et al. Measurements of the deuteron and proton magnetic form factors at large momentum transfers. *Phys. Rev. C*, 42(1):38, 1990.
- [32] AF Sill, , et al. Measurements of elastic electron-proton scattering at large momentum transfer. *Phys. Rev. D*, 48(1):29, 1993.
- [33] J Arrington, W Melnitchouk, and JA Tjon. Global analysis of proton elastic form factor data with two-photon exchange corrections. *Phys. Rev. C*, 76(3):035205, 2007.

- [34] C. B. Crawford et al. Measurement of the proton's electric to magnetic form factor ratio from  ${}^1\vec{H}(\vec{e}, e'p)$ . *Phys. Rev. Lett.*, 98:052301, 2007. doi: 10.1103/PhysRevLett.98.052301. URL <http://link.aps.org/doi/10.1103/PhysRevLett.98.052301>.
- [35] BD Milbrath et al. Comparison of polarization observables in electron scattering from the proton and deuteron. *Phys. Rev. Lett.*, 80(3):452, 1998.
- [36] DH Barkhuff et al. Measurement of recoil proton polarizations in the electrodisintegration of deuterium by polarized electrons. *Phys. Lett. B*, 470(1):39–44, 1999.
- [37] T Pospischil et al. Measurement of  $G_{E_p}/G_{M_p}$  via polarization transfer at  $Q^2=0.4$  (GeV/c) $^2$ . *Eur. Phys. J. A*, 12(1):125–127, 2001.
- [38] S. Dieterich et al. Polarization transfer in the  ${}^4\text{He}(\vec{e}, e'\vec{p}){}^3\text{H}$  reaction. *Phys. Lett. B*, 500(12):47 – 52, 2001. ISSN 0370-2693. doi: [http://dx.doi.org/10.1016/S0370-2693\(01\)00052-1](http://dx.doi.org/10.1016/S0370-2693(01)00052-1). URL <http://www.sciencedirect.com/science/article/pii/S0370269301000521>.
- [39] O Gayou et al. Measurements of the elastic electromagnetic form factor ratio  $\mu_p G_{E_p}/G_{M_p}$  via polarization transfer. *Phys. Rev. C*, 64(3):038202, 2001.
- [40] O Gayou. Nuclear physics measurement of  $\mu_p G_{E_p}/G_{M_p}$  in  $ep \rightarrow ep$  to  $Q^2=5.6$  GeV $^2$ . *Phys. Rev. Lett.*, 88(9):92301–92500, 2002.
- [41] M. K. Jones et al.  $G_{E_p}/G_{M_p}$  ratio by polarization transfer in  $\vec{e} p \rightarrow e \vec{p}$ . *Phys. Rev. Lett.*, 84:1398–1402, Feb 2000. doi: 10.1103/PhysRevLett.84.1398. URL <http://link.aps.org/doi/10.1103/PhysRevLett.84.1398>.
- [42] V Punjabi et al. Proton elastic form factor ratios to  $Q^2= 3.5$  GeV $^2$  by polarization transfer. *Phys. Rev. C*, 71(5):055202, 2005.
- [43] S Strauch et al. Polarization transfer in the  ${}^4\text{He}(\vec{e}, e'\vec{p}){}^3\text{H}$  reaction up to  $Q^2=2.6$  (GeV/c) $^2$ . *Phys. Rev. Lett.*, 91(5):052301, 2003.
- [44] Bitao H et al. Polarization transfer in the  ${}^2\text{H}(\vec{e}, e'\vec{p})n$  reaction up to  $Q^2= 1.61$  (GeV/c) $^2$ . *Phys. Rev. C*, 73(6):064004, 2006.
- [45] X Zhan et al. High-precision measurement of the proton elastic form factor ratio  $\mu_p G_{E_p}/G_{M_p}$  at low  $Q^2$ . *Phys. Lett. B*, 705(1):59–64, 2011.

- [46] G Ron et al. Low- $Q^2$  measurements of the proton form factor ratio  $\mu_p G_{E_p}/G_{M_p}$ . *Phys. Rev. C*, 84(5):055204, 2011.
- [47] M Paolone et al. Polarization transfer in the  ${}^4\text{He}(\vec{e}, e'\vec{p}){}^3\text{H}$  reaction at  $Q^2 = 0.8$  and  $1.3$  (GeV/c) $^2$ . *Phys. Rev. Lett.*, 105(7):072001, 2010.
- [48] G A Miller and M R Frank.  $Q^2$  independence of  $QF_2/F_1$ , poincaré invariance, and the nonconservation of helicity. *Phys. Rev. C*, 65(6):065205, 2002.
- [49] S. Boffi, L.Ya. Glozman, W. Klink, W. Plessas, M. Radici, and R.F. Wagenbrunn. Covariant electroweak nucleon form factors in a chiral constituent-quark model. *Eur. Phys. J. A*, 14(1):17–21, 2002. ISSN 1434-601X. doi: 10.1140/epja/iepja1403. URL <http://dx.doi.org/10.1140/epja/iepja1403>.
- [50] A Faessler, T Gutsche, V E Lyubovitskij, and K Pumsa-Ard. Chiral dynamics of baryons in a lorentz covariant quark model. *Phys. Rev. D*, 73(11):114021, 2006.
- [51] MA Belushkin, H-W Hammer, and Ulf-G Meißner. Dispersion analysis of the nucleon form factors including meson continua. *Phys. Rev. C*, 75(3):035202, 2007.
- [52] JPBC De Melo, T Frederico, E Pace, S Pisano, and G Salme. Timelike and spacelike nucleon electromagnetic form factors beyond relativistic constituent quark models. *Phys. Lett. B*, 671(1):153–157, 2009.
- [53] I Sick. On the rms-radius of the proton. *Phys. Lett. B*, 576(1):62–67, 2003.
- [54] P J Mohr, B N Taylor, and D B Newell. CODATA recommended values of the fundamental physical constants: 2006a). *J. Phys. Chem. Ref. Data*, 37(3):1187–1284, 2008.
- [55] J C Bernauer et al. High-precision determination of the electric and magnetic form factors of the proton. *Phys. Rev. Lett.*, 105(24):242001, 2010.
- [56] P J Mohr, B N Taylor, and D B Newell. CODATA recommended values of the fundamental phys. constants: 2010a). *J. Phys. Chem. Ref. Data*, 41(4):043109, 2012.
- [57] R Gilman et al. Studying the proton "radius" puzzle with  $\mu p$  elastic scattering. *arXiv preprint arXiv:1303.2160*, 2013.
- [58] V Punjabi, CF Perdrisat, MK Jones, EJ Brash, and CE Carlson. The structure of the nucleon: Elastic electromagnetic form factors. *Eur. Phys. J. A*, 51(7):1–44, 2015.

- [59] F Iachello, AD Jackson, and A Lande. Semi-phenomenological fits to nucleon electromagnetic form factors. *Phys. Lett. B*, 43(3):191–196, 1973.
- [60] E L Lomon. Extended gari-krümpelmann model fits to nucleon electromagnetic form factors. *Phys. Rev. C*, 64(3):035204, 2001.
- [61] William R Frazer and Jose R Fulco. Effect of a pion-pion scattering resonance on nucleon structure. *Phys. Rev. Lett.*, 2(8):365, 1959.
- [62] E L Lomon. Effect of revised  $R_n$  measurements on extended gari-krumpelmann model fits to nucleon electromagnetic form factors. *arXiv preprint nucl-th/0609020*, 2006.
- [63] R Bijker and Francesco Iachello. Reanalysis of the nucleon spacelike and timelike electromagnetic form factors in a two-component model. *Phys. Rev. C*, 69(6):068201, 2004.
- [64] Franz Gross, G Ramalho, and MT Pena. Pure s-wave covariant model for the nucleon. *Phys. Rev. C*, 77(1):015202, 2008.
- [65] PL Chung and F Coester. Relativistic constituent-quark model of nucleon form factors. *Phys. Rev. D*, 44(1):229, 1991.
- [66] F Cardarelli, E Pace, G Salme, and S Simula. Nucleon and pion electromagnetic form factors in a light-front constituent quark model. *Phys. Lett. B*, 357(3):267–272, 1995.
- [67] VB Berestetsky and MV Terentev. Nucleon form-factors and dynamics of the light front. *Sov. J. Nucl. Phys*, 25:347–354, 1977.
- [68] E Pace, G Salme, F Cardarelli, and S Simula. A light-front description of electromagnetic form factors for  $J \leq 3/2$  hadrons. *Nucl. Phys. A*, 666:33–37, 2000.
- [69] L Ya Glozman, Z Papp, W Plessas, K Varga, and RF Wagenbrunn. Effective q- q interactions in constituent quark models. *Phys. Rev. C*, 57(6):3406, 1998.
- [70] Kenneth G. Wilson. Confinement of quarks. *Phys. Rev. D*, 10:2445–2459.
- [71] JJ Kelly. Simple parametrization of nucleon form factors. *Phys. Rev. C*, 70(6):068202, 2004.
- [72] T Eden et al. Electric form factor of the neutron from the  ${}^2\text{H}(\vec{e}, e'\vec{n}){}^1\text{H}$  reaction at  $Q^2=0.255$  (GeV/c) $^2$ . *Phys. Rev. C*, 50(4):R1749, 1994.

- [73] C Herberg et al. Determination of the neutron electric form factor in the  $D(e, e'n)p$  reaction and the influence of nuclear binding. *Eur Phys. J. A.*, 5(2):131–135, 1999.
- [74] I Passchier et al. Charge form factor of the neutron from the reaction  ${}^2\vec{H}(\vec{e}, e'n)p$ . *Phys. Rev. Lett.*, 82(25):4988, 1999.
- [75] J Golak, G Ziemer, Hiroyuki Kamada, H Witała, and Walter Gloeckle. Extraction of electromagnetic neutron form factors through inclusive and exclusive polarized electron scattering on a polarized  ${}^3\text{He}$  target. *Phys. Rev. C*, 63(3):034006, 2001.
- [76] D Rohe et al. Measurement of the neutron electric form factor  $G_{E_n}$  at  $0.67 (\text{GeV}/c)^2$  via  ${}^3\vec{H}e(\vec{e}, e'n)$ . *Phys. Rev. Lett.*, 83(21):4257, 1999.
- [77] R Madey et al. Measurements of  $G_{E_n}/G_{M_n}$  from the  ${}^2\vec{H}(\vec{e}, e'n){}^1\text{H}$  reaction to  $Q^2 = 1.45 (\text{GeV}/c)^2$ . *Phys. Rev. Lett.*, 91(12):122002, 2003.
- [78] G Warren et al. Measurement of the electric form factor of the neutron at  $Q^2 = 0.5$  and  $1.0 \text{ GeV}^2/c^2$ . *Phys. Rev. Lett.*, 92(4):042301, 2004.
- [79] R Schiavilla and I Sick. Neutron charge form factor at large  $Q^2$ . *Phys. Rev. C*, 64(4):041002, 2001.
- [80] J Arrington and I Sick. Precise determination of low- $Q$  nucleon electromagnetic form factors and their impact on parity-violating e-p elastic scattering. *Phys. Rev. C*, 76(3):035201, 2007.
- [81] R J Hill and G Paz. Model-independent extraction of the proton charge radius from electron scattering. *Phys. Rev. D*, 82(11):113005, 2010.
- [82] IT Lorenz and Ulf-G Meißner. Reduction of the proton radius discrepancy by  $3\sigma$ . *Phys. Lett. B*, 737:57–59, 2014.
- [83] J C Bernauer and M O Distler. Avoiding common pitfalls and misconceptions in extractions of the proton radius. *arXiv:1606.02159v1*, 2016.
- [84] J. Alcorn et al. Basic instrumentation for hall a at Jefferson Lab. *Nucl. Instrum. Method. A*, 522(3):294 – 346, 2004. ISSN 0168-9002. doi: <http://dx.doi.org/10.1016/j.nima.2003.11.415>. URL <http://www.sciencedirect.com/science/article/pii/S0168900203033977>.

- [85] Pengjia Zhu. *A Measurement of the Protons Spin Structure Function  $g_2$  at Low  $Q^2$* . PhD thesis, University of Sci. and Technology of China, 2015.
- [86] Melissa A. Cummings. *Investigating Proton Spin Structure: A Measurement of  $g_2$  at Low  $Q^2$* . PhD thesis, The College of William and Mary, 2016.
- [87] Christoph W. L, David R. D, and Geoffrey A. K. The continuous electron beam accelerator facility: CEBAF at the Jefferson Laboratory. *Annu. Rev. Nucl. Part. Sci.*, 51:41350, 2001. URL <http://www.annualreviews.org/doi/abs/10.1146/annurev.nucl.51.101701.132327>.
- [88] T. Allison, R. Bachimanchi, E. Daly, M. Drury, C. Hovater, G. Lahti, C. Mounts, R. Nelson, and T. Plawski. CEBAF srf performance during initial 12 GeV commissioning. In *Proceedings of IPAC2015*, 2015.
- [89] Pengjia Z et al. Beam position reconstruction for the g2p experiment in hall a at Jefferson Lab. *Nucl. Instrum. Method. A*, 808:1 – 10, 2016. ISSN 0168-9002. doi: <http://dx.doi.org/10.1016/j.nima.2015.10.086>. URL <http://www.sciencedirect.com/science/article/pii/S0168900215013200>.
- [90] M Baylac, E Burtin, C Cavata, S Escoffier, B Frois, D Lhuillier, F Marie, J Martino, D Neyret, T Pussieux, P.Y Bertin, C.W de Jager, and J Mitchell. First electron beam polarization measurements with a compton polarimeter at Jefferson Laboratory. *Phys. Lett. B*, 539(12):8 – 12, 2002. ISSN 0370-2693. doi: [http://dx.doi.org/10.1016/S0370-2693\(02\)02091-9](http://dx.doi.org/10.1016/S0370-2693(02)02091-9). URL <http://www.sciencedirect.com/science/article/pii/S0370269302020919>.
- [91] Møller measurements for E08-027 (g2p) and E08-007, 2012. URL <http://hallaweb.jlab.org/equipment/moller/e08-027.html>.
- [92] D.G. Crabb and D.B. Day. The Virginia/Basel/SLAC polarized target: operation and performance during experiment E143 at SLAC. *Nucl. Instrum. Method. A*, 356(1):9 – 19, 1995. ISSN 0168-9002. doi: [http://dx.doi.org/10.1016/0168-9002\(94\)01436-1](http://dx.doi.org/10.1016/0168-9002(94)01436-1). URL <http://www.sciencedirect.com/science/article/pii/S0168900294014361>.
- [93] T.D. Averett et al. A solid polarized target for high-luminosity experiments. *Nucl. Instrum. Method. A*, 427(3):440 – 454, 1999. ISSN 0168-9002. doi: [http://dx.doi.org/10.1016/S0168-9002\(99\)00143-1](http://dx.doi.org/10.1016/S0168-9002(99)00143-1).

org/10.1016/S0168-9002(98)01431-4. URL <http://www.sciencedirect.com/science/article/pii/S0168900298014314>.

- [94] Or A Rondón. The RSS and SANE experiments at Jefferson Lab. In *AIP Conference Proceedings*, volume 1155, 2009.
- [95] D. G. Crabb and W. Meyer. Solid polarized targets for nuclear and particle physics experiments. *Annu. Rev. Nucl. Part. Sci.*, 47(1):67–109, 1997. doi: 10.1146/annurev.nucl.47.1.67. URL <http://dx.doi.org/10.1146/annurev.nucl.47.1.67>.
- [96] D. Keller. Uncertainty minimization in NMR measurements of dynamic nuclear polarization of a proton target for nuclear physics experiments. *Nucl. Instrum. Method. A*, 728:133 – 144, 2013. ISSN 0168-9002. doi: <http://dx.doi.org/10.1016/j.nima.2013.06.103>. URL <http://www.sciencedirect.com/science/article/pii/S0168900213009625>.
- [97] J. Pierce et al. Dynamically polarized target for the and experiments at Jefferson Lab. *Nucl. Instrum. Method. A*, 738:54 – 60, 2014. ISSN 0168-9002. doi: <http://dx.doi.org/10.1016/j.nima.2013.12.016>.
- [98] G.R. Court, D.W. Gifford, P. Harrison, W.G. Heyes, and M.A. Houlden. A high precision q-meter for the measurement of proton polarization in polarised targets. *Nucl. Instrum. Method. A*, 324(3):433 – 440, 1993. ISSN 0168-9002. doi: [http://dx.doi.org/10.1016/0168-9002\(93\)91047-Q](http://dx.doi.org/10.1016/0168-9002(93)91047-Q). URL <http://www.sciencedirect.com/science/article/pii/016890029391047Q>.
- [99] R J. Donnelly and C F. Barenghi. The observed properties of liquid helium at the saturated vapor pressure. *J. Phys. Chem. Ref. Data*, 27(6), 1998.
- [100] Nilanga Liyanage. Calibration of the hall a high resolution spectrometers using the new optimizer. Technical report, Jefferson Lab, Newport News, VA, United States, July 2002. URL <http://hallaweb.jlab.org/publications/Technotes/files/2002/02-012.pdf>.
- [101] Chao Gu. Spectrometer optics study for E08-027. Technical report, University of Virginia, Charlottesville, VA, United States, January 2016. URL [http://hallaweb.jlab.org/experiment/g2p/technotes/E08027\\_TN2016\\_18.pdf](http://hallaweb.jlab.org/experiment/g2p/technotes/E08027_TN2016_18.pdf).
- [102] Chao Gu. Target field mapping and uncertainty estimation. Technical report, University of Virginia, Charlottesville, VA, United States, 2015.

- [103] Survey report a1453. Technical report, . URL <http://hallaweb.jlab.org/experiment/g2p/survey/>.
- [104] Survey report a1465. Technical report, . URL <http://hallaweb.jlab.org/experiment/g2p/survey/>.
- [105] Chao Gu. Helicity decoder for E08-027. Technical report, University of Virginia, Charlottesville, VA, United States, August 2014. URL [http://hallaweb.jlab.org/experiment/g2p/collaborators/chao/technotes/Chao\\_TechNote\\_HelicityDecoder.pdf](http://hallaweb.jlab.org/experiment/g2p/collaborators/chao/technotes/Chao_TechNote_HelicityDecoder.pdf).
- [106] B. Adeva et al. Measurement of proton and nitrogen polarization in ammonia and a test of equal spin temperature. *Nucl. Instrum. Method. A*, 419(1):60 – 82, 1998. ISSN 0168-9002. doi: [http://dx.doi.org/10.1016/S0168-9002\(98\)00916-4](http://dx.doi.org/10.1016/S0168-9002(98)00916-4). URL <http://www.sciencedirect.com/science/article/pii/S0168900298009164>.
- [107] Jie Liu. Radiation effects in simulation. Technical report, University of Virginia, May 2015. URL [http://hallaweb.jlab.org/experiment/g2p/collaborators/jie/2015\\_05\\_13\\_simu\\_rad\\_technotes/radiation\\_simulation\\_technotes.pdf](http://hallaweb.jlab.org/experiment/g2p/collaborators/jie/2015_05_13_simu_rad_technotes/radiation_simulation_technotes.pdf).
- [108] J. Arrington. Implications of the discrepancy between proton form factor measurements. *Phys. Rev. C*, 69:022201, Feb 2004. doi: 10.1103/PhysRevC.69.022201. URL <http://link.aps.org/doi/10.1103/PhysRevC.69.022201>.
- [109] C.W. De Jager, H. De Vries, and C. De Vries. Nuclear charge and moment distributions nuclear charge- and magnetization-density-distribution parameters from elastic electron scattering. *Atom. Data Nucl. Data Tab.*, 14(5):479 – 508, 1974. ISSN 0092-640X. doi: [http://dx.doi.org/10.1016/S0092-640X\(74\)80002-1](http://dx.doi.org/10.1016/S0092-640X(74)80002-1). URL <http://www.sciencedirect.com/science/article/pii/S0092640X74800021>.
- [110] J. W. Lightbody and J. S. OConnell. Modeling single arm electron scattering and nucleon production from nuclei by gev electrons. *Computers in Phys.*, 2(3):57–64, 1988. doi: <http://dx.doi.org/10.1063/1.168298>. URL <http://scitation.aip.org/content/aip/journal/cip/2/3/10.1063/1.168298>.
- [111] P. E. Bosted and V. Mamyan. Empirical Fit to electron-nucleus scattering. *ArXiv e-prints*, 2012. URL <http://adsabs.harvard.edu/abs/2012arXiv1203.2262B>.

# Appendix A

## Elastic Scattering Kinematics

Electron-proton elastic scattering kinematics imply some correlations between incoming electron energy, scattered electron energy, scattering angle, and  $Q^2$ . We use these correlations throughout this report, and we will show these correlations in this chapter.

An incoming electron with four-momentum  $k^\mu = (E, 0, 0, k)$  is scattered off a static nucleus in the lab frame,  $P^\mu = (M, 0, 0, 0)$ . The electron is scattered in the  $x - z$  plane with  $k'^\mu = (E', k' \sin \theta, 0, k' \cos \theta)$ , and the proton recoils with  $P'^\mu = (E'_p, -P' \sin \phi, 0, P' \cos \phi)$  (see Fig. A.1). Energy-momentum conservation implies:

$$k^\mu + P^\mu = k'^\mu + P'^\mu. \quad (\text{A.1})$$

Or implicitly:

$$E + M = E' + E'_p \quad (\text{A.2})$$

$$k' \sin \theta = P' \sin \phi \quad (\text{A.3})$$

$$k = k' \cos \theta + P' \cos \phi \quad (\text{A.4})$$

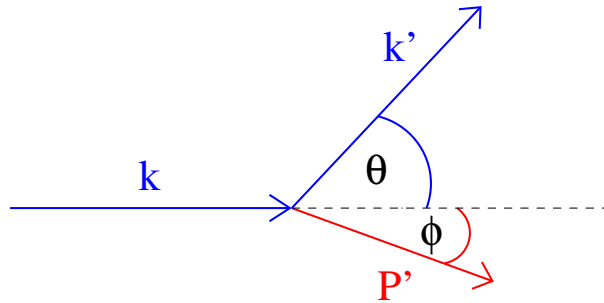


Figure A.1: Notations for elastic scattering.

We want to solve these equations. We start by calculating the magnitude of the 3-momentum:

$$\vec{P}'^2 = P'^2 \cos^2 \phi + P'^2 \sin^2 \phi \quad (\text{A.5})$$

$$P' \cos \phi = k - k' \cos \theta \quad (\text{A.6})$$

$$\vec{P}'^2 = k'^2 \sin^2 \theta + k^2 + k'^2 \cos^2 \theta - 2kk' \cos \theta \quad (\text{A.7})$$

$$\vec{P}'^2 = k^2 + k'^2 - 2kk' \cos \theta. \quad (\text{A.8})$$

Now using Eq. A.2:

$$E_p'^2 = E^2 + M^2 + E'^2 + 2EM - 2E'M - 2EE' \quad (\text{A.9})$$

The relativistic energy is:

$$E_p'^2 = \vec{P}'^2 + M^2 = k^2 + k'^2 - 2kk' \cos \theta + M^2 \quad (\text{A.10})$$

For ultra relativistic electrons  $E \approx k$ :

$$E_p'^2 = E^2 + E'^2 - 2EE' \cos \theta + M^2 \quad (\text{A.11})$$

$$\implies E^2 + E'^2 - 2EE' \cos \theta + M^2 = E^2 + M^2 + E'^2 + 2EM - 2E'M - 2EE' \quad (\text{A.12})$$

$$E' [M + E (1 - \cos \theta)] = EM \quad (\text{A.13})$$

$$E' = \frac{E}{1 + \frac{E}{M} (1 - \cos \theta)} \quad (\text{A.14})$$

We also want to calculate  $Q^2 = -q_\mu q^\mu$ . We start by writing the momentum transfer:

$$q^\mu = k^\mu - k'^\mu \quad (\text{A.15})$$

$$q^\mu = (E - E', -k' \sin \theta, 0, k - k' \cos \theta) \quad (\text{A.16})$$

$$q^2 = (E - E')^2 - k'^2 \sin^2 \theta - (k - k' \cos \theta)^2 \quad (\text{A.17})$$

$$q^2 = E^2 + E'^2 - 2EE' - k'^2 (\sin^2 \theta + \cos^2 \theta) - k^2 + 2kk' \cos \theta \quad (\text{A.18})$$

Using  $E \approx k, E' \approx k'$ :

$$q^2 = -2EE'(1 - \cos \theta) \quad (\text{A.19})$$

Using the identity:

$$\sin^2 \left( \frac{\theta}{2} \right) = \frac{1 - \cos \theta}{2}, \quad (\text{A.20})$$

we get:

$$Q^2 = -q^2 = 4EE' \sin^2 \left( \frac{\theta}{2} \right). \quad (\text{A.21})$$

# Appendix B

## The Breit Frame

The Breit frame, or the brick wall frame, is defined as the frame where the interaction only flips the sign of the nucleon three momentum, without changing its magnitude:

$$\vec{p}_B = -\vec{p}'_B = -\frac{\vec{q}_B}{2}. \quad (\text{B.1})$$

In elastic scattering, there is no energy transfer in the Breit frame:

$$\omega_B = 0 \quad (\text{B.2})$$

$$Q^2 = -q_{B,\mu}q_B^\mu = \vec{q}_B^2. \quad (\text{B.3})$$

For the electron:

$$\begin{aligned} E_B &= E'_B, \\ \vec{k}_B^2 &= \vec{k}'_B{}^2, \\ \vec{k}_B &= \vec{q}_B + \vec{k}'_B. \end{aligned} \quad (\text{B.4})$$

Choosing the 3-axis parallel to  $\vec{q}$  implies:

$$\begin{aligned} k_{B1} = k'_{B1} &= \frac{|\vec{q}_B|}{2} \cot \frac{\theta_B}{2} = \frac{\sqrt{Q^2}}{2} \cot \frac{\theta_B}{2}, \\ k_{B2} = k'_{B2} &= 0, \\ k_{B3} = -k'_{B3} &= \frac{\vec{q}_B}{2} = \frac{\sqrt{Q^2}}{2}. \end{aligned} \quad (\text{B.5})$$

Back to the lab frame, the 1 and 2 components are unaffected by the Lorentz transformation:

$$k_1 = k_{B1}; k_2 = k_{B2}, \quad (\text{B.6})$$

and we use the fact that  $\vec{q}$  is along the 3-axis to write:

$$\begin{aligned}
k_3^2 &= \frac{(\vec{k} \cdot \vec{q})^2}{\vec{q}^2} \\
&= \frac{\vec{k} \cdot \vec{k} - \vec{k} \cdot \vec{k}'}{\vec{q}^2} \\
&= \frac{E^2 + (EE' \cos \theta)^2 - 2E^2 EE' \cos \theta}{\vec{q}^2},
\end{aligned} \tag{B.7}$$

where  $\theta$  is the scattering angle in the lab frame.

$$\begin{aligned}
k_1^2 &= \vec{k}^2 - k_3^2, \\
&= \frac{\vec{k}^2 \vec{q}^2 - (\vec{k} \cdot \vec{q})^2}{\vec{q}^2}, \\
&= \frac{E^2 E'^2 \sin^2 \theta}{\vec{q}^2}, \\
&= \frac{4E^2 E'^2}{\vec{q}^2} \sin^2 \frac{\theta}{2} \cos^2 \frac{\theta}{2}.
\end{aligned} \tag{B.8}$$

Using the relation  $Q^2 = 4EE' \sin^2 \left(\frac{\theta}{2}\right)$  we get:

$$k_1^2 = \frac{(Q^2)^2}{4\vec{q}^2} \cot^2 \frac{\theta}{2}. \tag{B.9}$$

Since:

$$q^\mu = p'^\mu - p^\mu \tag{B.10}$$

$$p_\mu p^\mu = p'_\mu p'^\mu = M_p^2, \tag{B.11}$$

we get:

$$p'_\mu p'^\mu = q_\mu q^\mu + 2p_{\mu\nu} q^\mu + p_\mu p^\mu \tag{B.12}$$

$$q_\mu q^\mu = -2q_\mu p^\mu = -2\omega M_p \tag{B.13}$$

$$\omega = -\frac{Q^2}{2M_p}. \tag{B.14}$$

hence:

$$\vec{q}^2 = Q^2 \left(1 + \frac{Q^2}{4M_p^2}\right) = Q^2(1 + \tau). \tag{B.15}$$

We can now rewrite Eq. (B.9) as:

$$k_1^2 = \frac{Q^2}{4(1 + \tau)} \cot^2 \frac{\theta}{2}, \tag{B.16}$$

and, together with Eq. (B.6) gives the transformation between the scattering angles in the Breit frame and the lab as:

$$\cot^2 \frac{\theta_B}{2} = \frac{\cot^2 \frac{\theta}{2}}{1 + \tau}. \tag{B.17}$$

# מדידת יחס גורמי המבנה של הפרוטון במעבר תנע נמוך

חיבור לשם קבלת תואר דוקטור לפילוסופיה

מאת

משה פרידמן

הוגש לסנט האוניברסיטה העברית בירושלים

אב תשע"ו - אוגוסט 2016

עבודה זו נעשתה בהדרכתו  
של פרופסור גיא רון.

## תקציר

ניסוי E08-007-II מדד את יחס גורמי המבנה של הפרוטון,  $\mu\text{G}_E/\text{G}_M$ , במעברי תנע בתחום  $Q^2 \approx 0.02-0.08 \text{ GeV}^2$ . זהו תחום מעברי התנע הנמוך ביותר שנמדד בשיטות המבוססות על דרגות חופש של הספין. הניסוי נערך במעבדה הלאומית על שם תומאס ג'פרסון, הממוקמת בניופורט ניוז במדינת וירג'יניה, במהלך שנת 2012. קרן אלקטרונים מקוטבת באנרגיות של 1.1, 1.7 ו-2.2 GeV פוזרה על גבי מטרת אמוניה מוצקה מקוטבת. האסימטריה בין חתך הפעולה לפיזור אלסטי עבור אלקטרונים במצבי בורגיות חיוביים ושליילים נמדדה. מתוך אסימטריה זו ניתן לחלץ את יחס גורמי המבנה של הפרוטון.

בתזה זו אנו מציגים את אנליזת האסימטריה של הניסוי, דנים באתגרים השונים ומציגים תוצאות ראשוניות וחלקיות של הניסוי. תוצאות ראשוניות אלו מרמזות על עליה ביחס גורמי המבנה מעבר ל-1. ברם, יש צורך בהשלמה של האנליזה על מנת להגיע למסקנות כלשהן מן הנתונים. המשך עבודת האנליזה בעיצומה, ותוצאות סופיות עבור האסימטריות ועבור יחס גורמי המבנה צפויות במהלך 2017.

בנוסף, אנו מציגים לראשונה תוצאות נסיוניות של אסימטריה לפיזורים אלסטיים וקוואזי-אלסטיים על חנקן 14. התוצאות שנמדדו מתאימות להערכה על בסיס מודל הקליפות, בתוך רמת הדיוק של הניסוי. בניסוי נצפה שינוי בכיוון האסימטריה בין פיזורים אלסטיים וקוואזי אלסטיים, תופעה הדורשת מחקר נוסף. תוצאות אלו ישמשו לצורך האנליזה של ניסויים אחרים המשתמשים במטרת אמוניה מוצקה מקוטבת.

## מכתב תרומה

הניסוי המתואר בתזה זו, ההכנות והאנליזה נעשו כחלק ממאמץ משותף של הקולבורציות E08-007 ו-E08-027. העבודה הזו מתמקדת בתרומה האישית שלי לחלקים הניסיוניים ולאנליזה של הניסוי. מטבע הדברים, התזה מתארת גם את עבודתם של אחרים שתרמו לניסוי. מכיוון שישנם אנשים רבים שתרמו לצדדים השונים של המחקר, לא נוכל למנות אותם בשמותם.

ההכנות לניסוי נעשו ברובן זמן רב לפני הצטרפותי לקבוצה. מרגע שהצטרפתי לקבוצה, נטלתי את האחריות על ניסוי E08-007. במהלך הניסוי עצמו הייתי אחראי על אנליזה ראשונית של הנתונים, ועל קבלת החלטות בהתאם להתפתחות הניסוי.

לאחר הניסוי ביצעתי את האנליזה של חלק הפיסיקה בניסוי E08-007. החלקים הקשורים באופטיקה נעשו על ידי אחרים, מלבד תיקון זווית הפיזור הנובע ממיקומו של הפיק האלסטי המתואר בפרק 3.2.4, אותו ביצעתי בעצמי. גם האנליזה של המטרה נעשתה בעיקר על ידי הקבוצה שעוסקת בכך.

הסימולציה הבסיסית המתוארת בעבודה, g2psim, נכתבה בשיתוף של כמה אנשים, ותרומתי התבטאה בכתיבת המודלים לחתכי הפעולה האלסטיים. אני פיתחתי ויישמתי את ההתאמה המתוארת בעבודה של הסימולציה הבסיסית לתוצאות הניסיוניות, את ההליך למציאת התרומות החלקיות, ואת חילוץ האסימטריות עבור הפורטון והחנקן 14. אני גם ביצעתי את האנליזה של אי הוודאויות הנלוות לשלבים אלו.